Chem Soc Rev

REVIEW ARTICLE

View Article Online
View Journal | View Issue

Cite this: *Chem. Soc. Rev.*, 2019, **48**, 205

From CO_2 methanation to ambitious long-chain hydrocarbons: alternative fuels paving the path to sustainability

Filipe Marques Mota and Dong Ha Kim *

The clean and sustainable CO_2 reutilization toward products of higher value is of great interest in a background of established environmental concerns and reducing the use of fossil fuels. As promising alternative fuels, hydrocarbons are more valuable than CO, alcohols or formate and can be directly used in existing infrastructures with high energy densities. The prominent development of catalysts capable of selectively converting CO_2 into hydrocarbons, from methane to short olefins and long carbon-chains, has been reflected in an expanding volume of exploratory works, which suitably demand interpretive and continuous revision. In the past decades, conventional studies on the thermochemical conversion of CO_2 have consistently unlocked meaningful pathways toward the synthesis of hydrocarbons covering a fairly wide range of molecular weights. Conversely, both electrochemically and photochemically driven reactions have only now started to unveil encouraging results, with an extensive number of critical citations outlining the continuous emergence of very recently published reports. In a field in need of urgent development, the authors provide, in a clear form, a detailed retrospective on benchmark catalysts, pioneering approaches and competitive developments in this subject, mechanistic difficulties, emerging stability issues, and reactor design, while highlighting the latest noteworthy reports. Most importantly, this review highlights the advances toward an increase in the hydrocarbon chain-length in the synthesis of highly competitive alternative fuels. Comparisons of valuable thermochemical, electrochemical and photochemically driven strategies in the conversion of CO_2 to hydrocarbons are expected to serve as guidelines to disclose promising pathways in a field where mechanistic uncertainties remain a bottleneck for determining the product selectivity. The authors summarize leading and inquisitive perspectives with a focus on the viability and practicability of each approach at a larger scale, while tentatively paving the way to stimulate progress in this field.

Received 26th June 2018

DOI: 10.1039/c8cs00527c

rsc.li/chem-soc-rev

Department of Chemistry and Nano Science, Ewha Womans University, 52 Ewhayeodae-gil, Seodaemun-gu, Seoul 03760, Korea. E-mail: dhkim@ewha.ac.kr

Filipe Marques Mota

Dr Filipe Marques Mota received his PhD degree in 2013 in Bioscience Engineering from K.U. Leuven (Belgium), in collaboration with IFP Energies Nouvelles (France) in the development of hydroconversion catalysts. He later worked as a research fellow at the Institute for Basic Science (Korea) in the synthesis and application of hierarchical nanostructured materials. He is currently a research professor in the Department of Chemistry and Nano Science at Ewha Womans University. His research interests focus on current challenges in the electrocatalytic and photocatalytic reutilization of CO_2, and in the development of energy storage devices.

Dong Ha Kim

Prof. Dong Ha Kim received his PhD degree from the Department of Fiber and Polymer Science at Seoul National University (2000). He worked as a postdoctoral researcher at the University of Massachusetts at Amherst and at the Max Planck Institute for Polymer Research. He assumed a faculty position in the Department of Chemistry and Nano Science at Ewha Womans University (2006). His research interests include the development of hybrid nanostructures for energy storage and conversion, environmental remediation, memory devices, display devices, and theragnosis. He has authored 160 SCI publications and holds 31 Korean and 2 US patents.

1. Introduction

In the past decades, environmental concerns and societal dependence on dwindling oil resources have provided the impetus for the development of viable alternatives to fossil fuels. With an ever-increasing global demand for energy that is predominantly produced worldwide from fossil fuels, new and effective technologies have been the focus of attention in the scientific community. The development and expansion of natural gas to liquid (GTL) and coal to liquid (CTL) technologies, and the significant progress being made in the production of biofuels from algae and woody biomass have been highlighted.[1–4]

CO_2 emissions that lead to increasing atmospheric concentrations are major bottlenecks in the cement, metal, bioethanol, oil refining and petrochemical industries, with fossil fuel combustion in power plants being the primary source of CO_2 (Fig. 1). Current total global anthropogenic emissions amount to *ca.* 35.5 Gt_{CO_2} per year, reflecting an increase in the CO_2 in the atmosphere from 278 ppm at the beginning of the industrial revolution to current values exceeding 400 ppm.[5,6] With CO_2 levels being widely accepted nowadays as one of the main reasons for global warming,[7,8] reducing carbon emissions on an adequate timescale to hinder further risks of climate change demands an urgent increase in the use of renewable energy.[9–11] Notwithstanding attempts to decarbonize the world economy, to date, the sum of constant non-carbon-emitting sources of energy remains scarce. Despite an increasing emphasis on renewable energy, the annual global investment in fossil energy has increased more than 2-fold over the period 2000–2013.[12] In this context, carbon capture followed by strategic sequestration (*e.g.* geological or deep-sea storage and mineralization) or fixation by reaction have emerged as research topics of heightened concern.[13–16] When put in perspective, under typical CO_2 injection and storage conditions (10 MPa and 40 °C), the storage of the currently produced CO_2 per day equals 1033 million barrels (MMbbl), which is 10-fold higher than the current daily global oil production rates (*ca.* 87–91 MMbbl).[17] At the current rates of growth, this value is predicted to attain a 20-fold increase in 2050.[18] These prospects underline the importance of discussing the premise of carbon reutilization. To date, the utilization of captured CO_2 is bottlenecked by the purity and partial pressure of the gas. While higher partial pressures facilitate the capture and separation of CO_2, power stations responsible for the highest CO_2 emissions exhibit significantly lower gas partial pressures when compared with those originating from petrochemical plants. Alternatively, CO_2 is much more abundantly present in ocean water than in air (up to 100 and 0.7 mg L^{-1}, respectively), with seawater revealing a net gain of dissolved CO_2 of 2 Gt per year.[19–21]

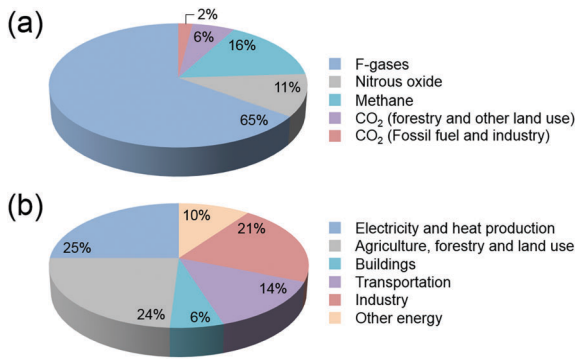

Fig. 1 (a) Global greenhouse gas production by human activities; (b) categorization based on the corresponding economic sectors. Source: IPCC (2014) based on emission values in 2010.[8]

The focus on the reutilization of carbon dioxide dates from the 1850s when the chemical transformation of CO_2 into chemicals, plastics, and fuels gained initial attention. Current examples of commercialized technologies include the synthesis of salicylic acid (1869),[22] sodium carbonate *via* the Solvay process (1882),[23] and urea production (1922).[24] The current annual global CO_2 utilization remains, however, on the order of 200 Mt, the equivalent of less than 0.6% of the total amount of anthropogenic emissions per year. In addition, with nearly 75% of the formed products, the incorporated CO_2 is released once the products are used, therefore hindering the long-term sequestration of the reutilized CO_2. CO_2 capture, distillation, and the overall availability of large-volume sources with high purity reflect severe limitations in the economic viability of promising technologies; the proposals for the large-scale implementation of innovative platforms require the careful analysis of associated opportunity costs.[17]

In any catalytic reaction, product selectivity along with the activity and stability of a selected material define the promising character of a catalyst. Once CO_2 is separated, the high stability of the molecule poses a challenge to its subsequent conversion. The chemically stable C═O bond possesses a dissociation energy of *ca.* 750 kJ mol^{-1}, requiring an equally high energy input and catalytically active materials for CO_2 reduction to occur. This high energetic demand emerges as a bottleneck in the large-scale implementation of the currently developed technologies for CO_2 hydrogenation; *e.g.* to methanol and methane. Concerning product selectivity, several routes have been developed for the selective reutilization of CO_2 toward a sustainable energy cycle for targeted fuels and chemicals, *e.g.* chemical reforming, photochemical, biological, mineralization and electrochemical methods. Recently, Li–CO_2 electrochemistry has been proposed for simultaneous CO_2 fixation and energy storage.[25–27] Conversely, using CO_2 as a building block to yield formic acid, carboxylic acids, urea, organic and cyclic carbamates, and organic, inorganic and cyclic carbonates has been widely reported, along with the synthesis of oxygenates, *e.g.*, methanol and dimethyl ether (DME), as promising and easily stored and transported fuels in internal combustion engines (Fig. 2).[28–36] Alternatively, the synthesis of CO_2 is often directed toward the formation of syngas (CO and H_2). The development of two-step cascade processes is a promising approach considering the viability of subsequent industrial platforms, *e.g.*, biotechnological syngas fermentation technologies, Fischer–Tropsch (FT) synthesis to produce fuels and chemicals, or the synthesis of alcohols (in particular, methanol) or methane.[37]

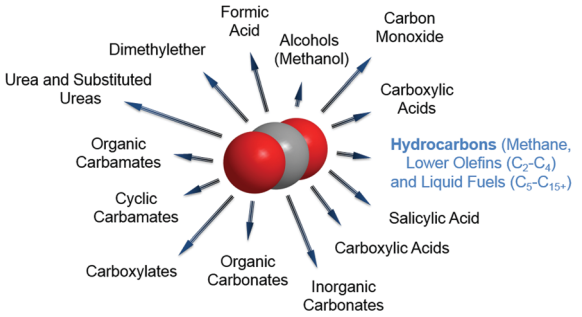

Fig. 2 Representative spectrum of possible products from the reutilization of CO_2.

1.1. Scope of the review

Within the plethora of emerging products assessed in the reutilization of CO_2, in this review, the authors provide a comprehensive dissection of reports of marked importance in the synthesis of hydrocarbons through thermochemical, electrochemical and photochemical approaches. The production of hydrocarbons reflects their role as the backbone of our energy infrastructure, with unparalleled energy density, and an emerging and valuable platform in ambitious space explorations. In addition to being a major component of natural and shale gas, relatively inexpensive and widely available, in the past decades, the production of methane (CH_4) has emerged as a pathway to a potential future energy-carrier and an alternative to an envisioned H_2 and methanol-driven sustainability. CH_4 production from CO_2 in the presence of H_2 serves as an alternative to the well-known bottlenecks in the storage and transportation of hydrogen related to its low volume density. This shift toward enhanced CH_4 production rates finds expected application within the current commercial infrastructure for electricity and heat generation as a substitute for gasoline, diesel or LPG in vehicles, and is appropriate in geographical regions where natural gas supplies are not abundant, and regulated CO_2 emissions may demand alternative energy storage routes.

Although synthesizing CH_4 is the less energetically demanding reaction pathway, extending the hydrocarbon chain to either paraffins or olefins is preferable from an economic point of view. These can either be stored as an energy carrier or directly used as a petrochemical feedstock (C_2–C_4) or as liquid fuels (C_5–C_{15+}). Lower olefins (C_2–C_4) for instance, are conventionally synthesized by the thermal or catalytic cracking of naphtha or vacuum gas oil, or by the dehydrogenation of alkanes of equal carbon number. With extensive application in the chemical industry as building blocks in the synthesis of polymers, solvents, drugs, cosmetics, and detergents and an overall two-fold boost in the global production capacity over the past 15 years,[38] the increasing demand for olefins from alternative feedstocks has been incited by both environmental and economic factors in recent years. The extensive market demand for olefins leading to the subsequent emission of *ca.* 1.2–1.8 tons of CO_2 per ton of olefin produced further underlines the importance of the selective reutilization of CO_2 to these products.

As the precursor to polyethylene, accounting for *ca.* 62% of the global ethylene consumption in 2016, C_2H_4 plays a major role in the plastic industry and benefits from an expanding global market and price point when compared to other C_2 value-added products. In 2021, ethylene global supply is projected to surpass the 170 million metric tons mark, with an increasing non-steam cracker percentage of *ca.* 6% predicted for the same year.[39] Taking into account the past market oscillations of the prices of conventional fossil fuels in recent years, the collected average prices still distinctly place ethylene (0.989 USD per kg) above the value-added products previously listed, *e.g.*, formic acid (0.4–0.6 USD per kg) or acetic acid (0.6 USD per kg).[40] Within the recently overviewed global market sizes, ethylene (155–248 billion USD) emerges two and three orders of magnitude above carbon monoxide (2.7–3.2 billion USD) and formic acid (0.62 billion USD), respectively.[41]

The synthesis of value-added transportation fuels accomplishing an idealized closed carbon cycle remains the most challenging to date. In the context of a depletion of fossil sources, the production of gasoline and diesel from CO_2, containing typically C_4–C_{12} and C_{12}–C_{20}, respectively, would represent a dramatic shift in sustainability. Despite the strong fluctuation in fuel prices in recent years, global consumptions continue to dramatically increase, reflecting the ever-increasing growth of global energy consumption. In particular, gasoline global market consumption has currently surpassed the annual 1000 million metric tons mark.[42] The noteworthy dependence of fossil fuels aggravated by drastic fluctuations in the oil market further underlines the need for the development of alternative fuels from conventional non-fossil sources.

The above-discussed economic interest in a direct CO_2RR to hydrocarbons demands the continuous updating of the current strategies for urgent development. Electrochemical and photochemical-based exploratory works, in particular, have reflected a dynamic development of promising approaches in recent years that deserve clear dissection in the delineation of impending strategic paths. Representative reviews available in the current literature tend, however, to cover the entire spectrum of formed products in the reutilization of CO_2, failing to provide the necessary level of detail presented here. The authors will further focus exclusively on heterogeneous catalytic systems. The facilitated separation of catalysts and formed products and reactants is of prime concern in the design of commercially practical processes and is notably advantageous in comparison with homogeneous systems. The following sections provide a detailed retrospective on the benchmark and innovative catalytic systems in terms of achieved activity, selectivity and stability levels. In addition, discussions on the proposed mechanistic pathways and the current associated difficulties, pioneering alternative approaches, and competitive developments are reviewed herein, while highlighting the latest noteworthy reports.

2. Thermochemical CO_2 reduction reaction (t-CO_2RR)

The extensive background in t-CO_2RR to hydrocarbons is a direct reflection of its ever-increasing attention in the community and of

an accelerated development in light of analogous CO-based technologies. In addition, the thermochemically-driven reaction has a greater potential to be applied on a large scale as compared to the energetically promising alternative electrochemical and photochemical strategies in the production of transportation fuels. For the reasons above, extensive progress has been made in the production of C_1 chemicals, *e.g.*, CO, formic acid, and methanol. The reduction of the fully oxidized carbon to hydrocarbons requires the promotion of the kinetics of a reaction highly limited by the transfer of at least eight electrons. Although great progress has been attained in the selective synthesis of CH_4, selectively producing long-chain hydrocarbons still faces a series of drawbacks and engineering bottlenecks. To date, the study of suitable catalysts essentially relies on single metal or alloy-based catalysts dispersed on metal oxides. Achieving progress in the development of CO_2RR platforms relies on an in-depth knowledge of its underlying chemical mechanism, with this drawback being inspected below.

2.1. Mechanistic difficulties

Assessing and eventually disentangling potential mechanistic pathways permits the optimization of the overall CO_2 conversion rates through the minimization of relevant thermodynamic or kinetic barriers of the intermediate reactions, and allows an enhancement of the overall product selectivity. When tentatively reducing CO_2 to the simplest hydrocarbon, CH_4, in the presence of H_2, the latter is easily dissociated over the ideally well-dispersed metallic phase. Subsequent spill-over of the resulting reactive atomic hydrogen species occurs on the support, where the hydrogenation of the involved carbon intermediates takes place. Mechanistically, the reduction of the CO_2 molecule has been recognized to significantly depend on the selected catalyst, the choice of the support (*cf.* Section 2.2.3), operating conditions, and CO_2 to H_2 reactant ratios.[43]

Chen and colleagues have recently summarized possible pathways for t-CO_2RR to CH_4 on metal/oxide catalysts; the adapted schematic diagram is depicted in Fig. 3.[44] A possible direct hydrogenation of CO_2 to synthetic natural gas claimed in earlier years is represented in Fig. 4.[45] As evidenced in Fig. 3, both proposed pathways – the RWGS + CO-Hydro and formate-based – reflect an emerging parallelism in the synthesis of alcohols during the production of hydrocarbons, a key point in the development of selective catalysts. Reaction pathways involving the initial conversion of CO_2 to CO, followed by the methanation of the adsorbed intermediates (CO*) have been widely argued. The formation of CO* is proposed to occur through the direct reverse water gas shift (RWGS) reaction pathway (Fig. 3), or following a direct C–O bond cleavage (Fig. 4). The formation of CO* is particularly emphasized over representative Ni/Al_2O_3 state-of-the-art catalysts in the selective CO_2RR to CH_4.[43,46,47]

The stability of the CO* intermediate determines whether the molecule will desorb or undergo further reduction. The reduction of CO* has been suggested to follow two distinct pathways: (1) the dissociation of CO* into carbon and oxygen species that are subsequently hydrogenated to CH_4 and water,

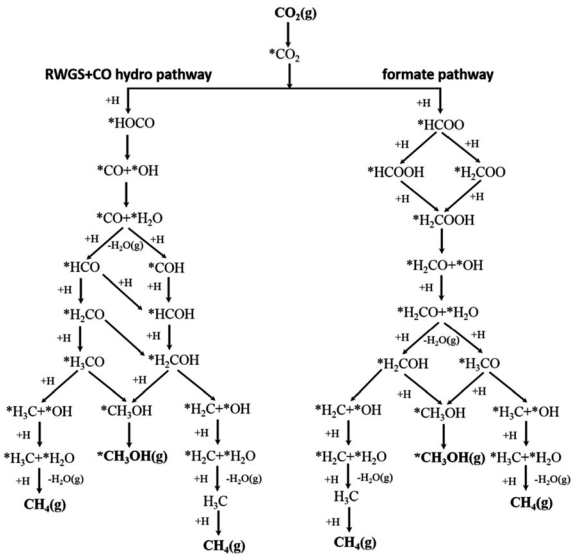

Fig. 3 Schematic representation of the proposed RWGS + CO-hydro and formate mechanistic pathways in the selective t-CO_2RR to methane. Adapted with permission from ref. 44. Copyright The Royal Society of Chemistry 2016.

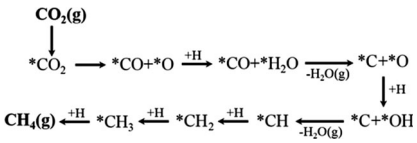

Fig. 4 Proposed direct C–O bond cleavage pathway in CO_2 methanation.

respectively; (2) the H_2-assisted transformation of CO* to HCO* or COH* species.[48] Despite the common formation of a CO* intermediate, higher CH_4 selectivity and lower activation energies have been reported when the atmosphere is switched from CO to CO_2, in accordance with the suggested CO* favored distribution during t-CO_2RR. Equally under debate is the formation and decomposition of observed surface formate species (Fig. 3). For instance, over Ni/Y_2O_3, formate species were proposed to be a reaction intermediate leading to enhanced catalytic activity but Behm claimed that the detected formate only played a minor role in the reaction, acting as a spectator species.[43,46]

When extending the carbon-chain from CH_4 to short olefins or products in the range of gasoline or even diesel, CO_2 has been proposed to be first converted into a more reactive CO* intermediate *via* RWGS, followed by the modified Fischer–Tropsch (FT) reaction, which conventionally utilizes syngas (CO and H_2) to generate long-chain hydrocarbons.[49–52] The proposed mechanism for a CO_2-based FT pathway is schematically simplified in Fig. 5. The conventional FT synthesis reaction utilizing syngas, first reported in the 20s by Hans Fischer and Franz Tropsch, applies iron and cobalt-based catalysts at high (HTFT) and low temperatures (LTFT), respectively. The properties of the resulting synthetic crudes (syncrudes) are significantly different depending on the type of temperature-based process,

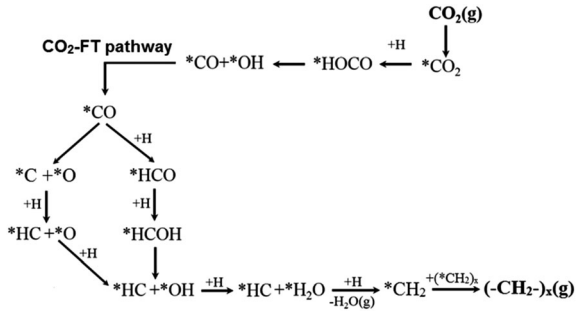

Fig. 5 Schematic representation of the proposed CO_2-based Fischer–Tropsch mechanistic pathway. Adapted with permission from ref. 44. Copyright The Royal Society of Chemistry 2016.

with three aspects being of importance to highlight (1) the probability of chain growth, (2) the degree of hydrogenation, and (3) secondary product formation.[53] The probability of chain growth over the selected catalyst determines the carbon number distribution, often expressed by using the Anderson–Schultz–Flory (ASF) equation. HTFT syncrude is characterized by a light carbon number distribution, rich in olefins and oxygenates, with aliphatic hydrocarbons being predominantly linear. To a minor extent, naphthenes, mostly in the naphtha fraction, and aromatics, with increasing content as carbon number increases, are present. In contrast, *ca.* 50% of the hydrocarbon mass of LTFT syncrude is in the C_{22+} fraction, and becomes more paraffinic with increasing carbon number.[54] Wax production is followed by selective hydrocracking to give the desired transportation fuels either in the naphtha or diesel ranges.

In agreement with the proposed mechanism in Fig. 5, a stronger CO* binding energy is expected to favor the synthesis of hydrocarbons, while a weakly adsorbed CO* favors the RWGS reaction with CO evolution.[55] The presumed parallelism between the CO_2RR and the conventional CO-based FT synthesis, with the emergence of CO as an intermediate in the former process and presumably similar chain-growth pathways, have served as valuable guidance in continuous exploratory works. For these reasons, several comparative studies have assessed the applicability of state-of-the-art FT catalytic systems using CO_2 as a feedstock. Leading groups have developed structure–function studies to enhance the selectivity of CO_2RR using conventional FT catalysts to attain C_{5+} hydrocarbon yields comparable to those produced with CO as the feedstock.[56] When switching the atmosphere from syngas to mixtures of CO_2 and H_2, state-of-the-art Fe-based CO_2RR catalysts ideally hinder the formation of CH_4 and favor the high olefinic nature of the yielded products (*cf.* Section 2.2.2).[57–60] Directing the CO_2-based Fischer–Tropsch mechanistic pathway toward the selective production of light olefins generally produced from fossil fuels including naphtha, gas oil, and light alkanes *via* catalytic cracking processes remains an alternative of interest as indicated in the introduction of this Review. Promoting the oligomerization of formed olefins to longer carbons is an alternative of equal importance, with the effect of residence time and co-feed being crucial to directing the readsorption of these products in the initiation of surface chains.[61]

An overall drawback in the direct application of conventional FT catalysts during t-CO_2RR is, however, the need for an additional component able to direct the RWGS for initial CO production. Notwithstanding the thermodynamical viability of the combination of the two reactions, reaction conditions for CO_2RR have been found to significantly differ from those of CO-based FT. Mechanistic difficulties have been highlighted in the past years, reflecting the prominent CO_2 inertness during adsorption and reaction steps, and subsequent C–C coupling barriers. The above issues are further dissected in Section 2.2.2 in the application of suitable catalysts under CO_2 and H_2 mixtures.

2.2. Overview of catalysts

To date, extensive research has drawn critical conclusions regarding the activity and the selectivity of unsupported metal catalysts and their supported counterparts while scrutinizing the effects of incorporated promoters, preparation methods, and synthesis conditions on the resulting performance. In conventional t-CO_2RR pathways, CO_2 is firstly converted to CO *via* the RWGS reaction, with the latter being subsequently transformed into hydrocarbons. The study of suitable catalysts has essentially relied on single metal or alloy-based catalysts dispersed on metal oxides. Notwithstanding the role of the support in the activation of CO_2 and the suggested support-dependent mechanistic pathways (*cf.* Section 2.2.3),[62] limited catalytic activity has been found over individually evaluated metal oxide systems, *e.g.*, ZnO, MnO_x, Al_2O_3, and CeO_2.[63] Notably decisive in all cases is the lack of H_2 dissociation sites, with CO formation through the RWGS reaction prevailing over the evaluated materials. In contrast, product selectivity is strikingly determined by the incorporated metal, with the reaction being preferentially directed to CH_4 or long-chain hydrocarbons in accordance with the emerging catalytic fingerprints of the selected metal element. Over the past decades, Ru, Rh, Pt, Pd, Ni, and Co-based catalysts have been shown to selectively promote the synthesis of CH_4 under the selected operating conditions. An extensive line of work has simultaneously focused on optimized CH_4 selectivity, enhanced activity, and the stability of these systems. The singularity of iron oxides, on the other hand, has been directed toward the synthesis of long-chain hydrocarbons in a clear parallelism with conventional CO-based FT platforms. Benchmark catalysts, the corresponding catalytic formulations, and the impact of the support and promoters in each case are detailed in the following sections.

2.2.1. Catalysts favoring t-CO_2RR to methane. For the production of the simplest hydrocarbon, methane, while the reaction can be driven under atmospheric or simply moderate pressures, most studies investigating the direct t-CO_2RR to CH_4 in the presence of H_2 (Fig. 3 and 4) have been performed at relatively high temperatures (>300 °C), which represents a major drawback toward relevant rates.[64,65] CO_2 methanation, being highly exothermic, demands the development of catalysts active at low-temperature ranges in which the undesired endothermic RWGS reaction is additionally suppressed. The investigated metal-based catalysts are discussed below. Table 1

Table 1 Performance of metal-based catalysts in t-CO_2RR to CH_4, tentatively compared on the basis of the temperature necessary to achieve *ca.* 60% CO_2 conversion, unless otherwise stated. Indicated methane selectivity (%) is obtained at corresponding conditions. Metal content (%), liquid hour space velocities (LHSV) and pressure (*P*) values are further indicated. As extensively discussed, to date, the most common catalyst for CO_2RR selectively to CH_4 still relies on Ni/Al_2O_3 formulations. State-of-the-art catalytic performances representing superior catalytic properties have however been italicized here

Catalyst	Metal (%)	H_2/CO_2	LHSV (L g^{-1} h^{-1})	*P* (MPa)	*T* (°C)	Selectivity (%)	Ref.
$Ce_{0.96}Ru_{0.04}O_2$	Ru	4	≈10 000 h^{-1}	0.1	450 (55%)	99	70
Highly dispersed Ru NP/TiO_2	*Ru (0.80)*	*4*	*4.18*	*0.1*	*140*	*100*	*73*
Ru NP/TiO_2 (“wet” impregnation)	Ru (0.75)	4	4.18	0.1	200	100	73
Ru/TiO_2 (rutile) reduced at 400 °C	Ru (5)	4	75	0.1	295	100	74
Ru/TiO_2 (anatase) reduced at 400	Ru (5)	4	75	0.1	335	100	74
Single-atom Ru/CeO_2	Ru (0.89)	4	120	0.1	295	100	77
Ru nanoclusters/CeO_2	Ru (2.56)	4	120	0.1	270	100	77
Pd/SiO_2	Pd (6.2)	4	≈3300 h^{-1}	0.1	450 (40.8%)	10.4	87
Pd–Mg/SiO_2	Pd (6.2)	4	≈3300 h^{-1}	0.1	450	95	87
Pd–Ni/SiO_2	Pd (6.2)	4	≈3300 h^{-1}	0.1	450 (50.5%)	89	87
Size-tunable Ni NP supported on surface-modified cage-type mesoporous SiO_2	Ni (21.7)	1	1.2	0.1	475 (11%)	65	96
Ni-MCM-41	Ni (1)	4	19.7	0.1	500 (50%)	83	94
Ni/RHA-Al_2O_3	Ni (15)	4	30	0.1	500	90	90
Ni/TiO_2	Ni (10)	4	10 000 h^{-1}	0.1	400	95	100
Ni/Al_2O_3	Ni (10)	4	10 000 h^{-1}	0.1	350	98	100
Ordered mesoporous nickel alumina	Ni (15)	5	91	0.1	350	94	92
Ni/CaO–Al_2O_3	Ni (23)	4	15 000 h^{-1}	0.1	335	100	106
Co-Impregnated Ni – 1 wt% MgO/SiO_2	Ni (10)	4	15	0.1	325	98	105
Ni/ZrO_2–Al_2O_3	Ni (12)	3.5	8.1	0.1	325	100	98
Ni/Al_2O_3	Ni (10)	4	20	0.1	300	100	43
Ni@MOF-5	Ni (10)	4	2000 h^{-1}	0.1	300	100	97
Ni/CeO_2	Ni (10)	4.6	22	0.1	300 (73%)	100	99
NiO–MgO–Al_2O_3	Ni (10)	4	15	0.1	290	96	107
Ni/CeO_2 (hard template synthesis method)	Ni (10)	4	45	0.1	285	100	102
Ni/mesoporous nanocrystalline γ-Al_2O_3	*Ni (20)*	*3.5*	*9*	*0.1*	*275*	*100*	*91*
Ni/CeO_2	*Ni (10)*	*4*	*10 000 h^{-1}*	*0.1*	*270*	*100*	*100*
Ni/CeO_2	*Ni (10)*	*4*	*20*	*0.1*	*270*	*100*	*43*
Ni/ZrO_2	Ni (10)	4	20	0.1	260	100	43
Ni/Sm_2O_3	Ni (10)	4	20	0.1	260	100	43
Ni/Y_2O_3	*Ni (10)*	*4*	*20*	*0.1*	*240*	*100*	*43*
Co/SiO_2	Co (3)	4	1640 h^{-1}	0.1	277 (13.7%)	42	60
Cobalt foil	Co	3	—	0.1	302 (1.55 CH_4 molecules/Co site s)	98	119
Co/ZrO_2	Co (10)	4	3.6	3	400 (92.5)	99.9	123
Co/SiO_2	Co (10)	4	3.6	3	400 (80.1)	97.8	123
Co/Al_2O_2	Co (10)	4	3.6	3	400 (77.8)	96.5	123
Co/SiC	Co (10)	4	3.6	3	400 (77.5)	96.4	123
Co/Al_2O_3	Co (20)	4	5000 h^{-1}	1.5	300	—	125
Co_4N/Al_2O_3	Co_4N (20)	4	5000 h^{-1}	1.5	*ca.* 230	98	125

summarizes the representative performances for a convenient comparison of the reported performances of the listed materials. Catalytic systems representing state-of-the-art performances have been highlighted.

Ruthenium and rhodium-based catalysts. When making comparisons between benchmark materials experimentally and theoretically investigated in the past decades, Ru and Rh-based catalysts unveiled remarkable CH_4 selectivity, and catalytic activities, even near room temperature.[47,66,67] The mode in which transient carbonyl species are bonded with ruthenium is claimed to play a key role in their reactivity, and is believed to depend on the Ru oxidation state at the time of interaction, the particle size and under-coordinated sites, the catalytic temperature, and the composition of the reacting stream.[67,68] Although works developed over other supports deserve equal attention,[69,70] fast-forward three decades from the seminal contribution of Grätzel, Ru/TiO_2 remains widely recognized as one of the most attractive catalytic formulations in CO_2RR attaining complete CH_4 selectivity under atmospheric pressure and temperatures under 200 °C.[64] The increase in activity with increasing metal–support reflects earlier reports in CO methanation over these catalysts. At 473 and 523 K, Ru/TiO_2 achieved superior activities as compared with MgO, Al_2O_3, SiO_2, and ZrO_2-supported counterparts.[71]

In the past thirty years, significant work on TiO_2-supported materials has shed much light on the performance of Ru. Mechanistically, FTIR experiments provide evidence for the formation of adsorbed CO species (Ru_x–CO, $Ru^{n+}(CO)_x$, (TiO_2)Ru–CO), and CO species linearly bonded to the reduced Ru crystallites (Ru_x–CO) were suggested to be reactive surface intermediates.[72] The size and morphology of Ru species has

been proved to depend on the crystal structure of TiO_2. At 180 °C, the size of Ru nanoparticles (NPs) on anatase-type TiO_2 determined the hydrogenation activity, with a maximal value with the smallest particles evaluated in this study (2.5 nm diameter).[73] Reflected in the formation of a Ru–O–Ti bond assessed by X-ray absorption measurements and H_2-TPR experiments, a rutile TiO_2-based interaction not only promotes the highly efficient dispersion of Ru NPs to a great extent, but also hinders their subsequent aggregation.[74] Sassoye found that Ru-based P25 commercial TiO_2, composed of 20% rutile and 80% anatase phases, exhibited superior performance as compared to pure anatase or the rutile-counterparts.[75] The authors later assessed the impact of mixing anatase and rutile TiO_2 in different ratios and at different stages of the catalyst preparation, *i.e.*, before or after RuO_2 deposition, or after annealing.[76] Following thermal reduction under H_2, the interaction between RuO_2 NPs and TiO_2 phases during the annealing step was shown to dictate the resulting catalytic performance. Characterization suggested the migration and subsequent epitaxial stabilization of RuO_2 NP over the rutile TiO_2 phase. The NPs could then be reduced with high dispersion and specific activity. Incorporated anatase was claimed to be beneficial to impede the negative effect of support sintering and the subsequent loss of accessible Ru active sites.

In light of a number of exploratory works on the effect of the support (*cf.* Section 2.2.3), assessing the strong metal–support interactions (SMSI) that arise has also been of key interest. Following the works of Abe, Zhang and colleagues recently investigated the effect of the size of Ru domains in Ru/CeO_2 nanowires from atomically-dispersed Ru centers, to Ru nanoclusters (*ca.* 1.2 nm), and Ru NPs (*ca.* 4.0 nm), utilizing *ex situ* and *in situ* spectroscopic techniques and density functional theory calculations (Fig. 6).[77] Interestingly, the nanoclusters showed superior CO_2RR activity, with 98–100% CH_4 selectivity, and a turnover frequency (TOF) of 7.41×10^{-3} s^{-1} at 190 °C. Ce^{3+}–OH sites and Ru sites near the metal–support interfaces were demonstrated to be responsible for CO_2 dissociation and for carbonyl hydrogenation, respectively. The strongest SMSI and H-spillover effects with the corresponding suppression of the activation of metal carbonyls and the dehydration of the support surfaces were found in single Ru atoms and the Ru NPs, respectively. Conversely, competitive SMSI and H-spillover reached a balance in CeO_2-supported Ru nanoclusters, with the resulting superior CO_2RR activity for selective CH_4 formation (Fig. 6e).

High CH_4 selectivity and superior activity have been emphasized in an extensive line of works using Rh/TiO_2.[78–81] Over Ru/γ-Al_2O_3 with metal NPs within a wide range of 3.6 to 15.4 nm, larger NPs unveiled a 4-fold superior activity at low temperatures (135–150 °C) whereas, at 200 °C, the turnover frequencies were found to be similar for all samples.[82] The same authors later reported that over TiO_2, the rate normalized by surface Rh atoms could be increased with an increase in the NP size up to *ca.* 7 nm, with a continuous size increase being shown to not play a significant role in the catalytic performance.[83] Kinetic parameters such as the apparent activation energy and reaction orders with respect to H_2 and CO_2 were also demonstrated to depend strongly on the Rh cluster size. These variations may arise from the disparity of the selected operating conditions and characterization of the selected supports, but they further pinpoint the NP size effect as one of the most debated issues in the development of supported catalysts in t-CO_2RR.

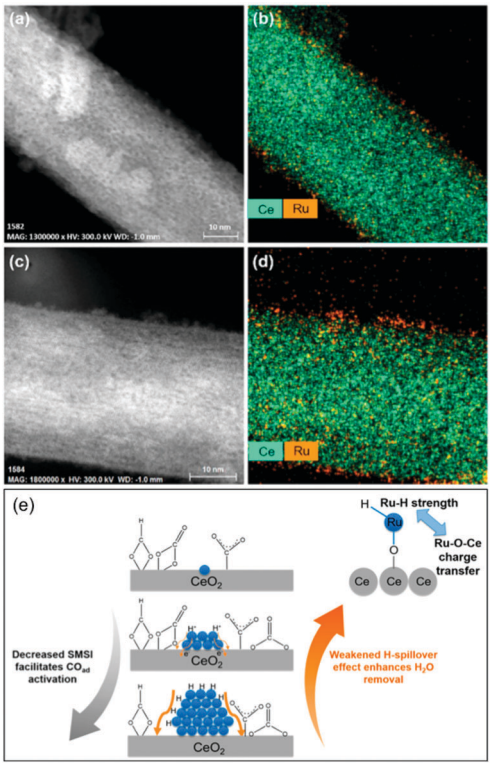

Fig. 6 Cs-Corrected (a and c) HAADF-STEM images and (b and d) the corresponding Ce and Ru element maps of (a and b) nanoclusters and (c and d) single-atom Ru on CeO_2 nanowires. (e) Proposed competitive strong metal–support interactions and H-spillover effects leading to the competing CO activation and surface dehydration over the Ru single-atoms, nanoclusters, and nanoparticles. Readapted with permission from ref. 77. Copyright 2018 American Chemical Society.

Palladium and platinum-based catalysts. Pd and Pt have emerged as promising candidates for t-CO_2RR, with Pt-based catalysts unveiling the most promising conversion levels at analogous operating conditions at the expense of a lower cost-effectiveness.[84] Comparatively, Pd shows negligible conversion below 300 °C and a preferential formation of CO over CH_4 in the said temperature ranges.[84] Favoring the RWGS or CH_4 production was, however, early confirmed to be alternately achieved over large or finely dispersed Pd NPs, respectively.[85] Shape-controlled Pd-nanocubes and nanopolyhedra particles revealed an activity and selectivity dependence on the exposed Pd facets (100) and (111), which were presumed to control the adsorption strength of intermediate CO*.[86] DFT studies on Pd on MgO/SiO_2 suggested the activation of CO_2 over MgO through the formation of magnesium carbonate species, whereas a supply of atomic hydrogen was essential for further hydrogenation of magnesium carbonate to CH_4.[87,88]

Nickel-based catalysts. Notwithstanding their excellent hydrogenation performance, the large-scale industrial application of noble metals is limited by their high cost. Fast forwarding nearly 30 years since Falconer assessed the premise of Ni under a CO_2 atmosphere,[52] Ni-based systems are today the most widely studied catalysts for CO_2RR due to their attractive cost-effectiveness. The slow adsorption of CO_2, believed to result in a higher H_2:CO surface ratio, has been ascertained to favor selective CH_4 production over long-chain hydrocarbons. Ni-Based catalysts, however, exhibit lower activity when compared with the representative Ru and Pd-based counterparts (Table 1), and a rather rapid deactivation due to carbon deposition, poisoning, and Ni sintering under high temperatures (*cf.* Section 2.4). For these reasons, the design of novel Ni-based catalysts, screening a wide spectrum of supports of choice with high surface area, *e.g.*, Al_2O_3, SiO_2, TiO_2, and CeO_2, attempts not only to favor enhanced metal–support interactions but also to hinder the deactivation of the Ni active centers.

Following a series of works on Ni-based amorphous SiO_2 catalysts,[89] Chang demonstrated that Al incorporation, with an enhancement of the acidity of the support, could crucially increase the overall hydrogenation activity.[90] At 500 °C, an optimized yield (*ca.* 58%) and desired methane selectivity (*ca.* 90%) were obtained. Over Ni supported on mesoporous γ-Al_2O_3, experimental results have shown that both t-CO_2RR activity and CH_4 selectivity could be continuously increased within a 10 to 20 wt% Ni loading range, whereas a 25 wt% Ni content led to larger crystallite size and inferior catalytic activities.[91] The evaluated loading range is additionally representative of most literature reports to date in the study of Ni-based catalysts (Table 1). As extensively discussed in Section 2.2.3, incorporating metal NPs into mesoporous and mesostructured materials is considered highly advantageous.[92] Ni embedded within a three-dimensional mesoporous SBA-15 unveiled higher activity, lower coke formation, and higher thermal stability in the 600–800 °C range as compared with conventional SiO_2 and γ-Al_2O_3 supports.[93] Highly dispersed and thermally stable metallic Ni over siliceous MCM-41 has shown enhanced CH_4 selectivity (up to 96%) in a low conversion range at 300 °C, superior to that of Ni/SiO_2 and even to a Ru/SiO_2 reference.[94] Over mesostructured silica nanoparticles (MSN), with extended intra- and inter-particle mesoporosity and a BET area of 1051 m^2 g^{-1}, dispersed Ni active centers showed higher activity compared to a conventional tubular-shaped MCM-41 architecture or a microporous 3D HY-zeolite-supported counterpart.[95] Taking advantage of the dimensionality, pore-size, and geometrical features of structured architectures is a well-established approach in catalytic platforms. Recently, ultra-small Ni NPs in a 2.7 to 4.7 nm-range, depending on the Ni content, were supported in the cage-type mesopores of –COOH-functionalized-silica SBA-16 *via* wet impregnation followed by thermal reduction.[96] At pH = 9, deprotonation of the carboxylic acid groups on the cage-type mesopore surfaces induced the effective incorporation of Ni^{2+} precursors *via* favorable electrostatic interactions, toward high dispersion of the resulting particles.

The manipulation of the interactions between the metal and the support while taking advantage of the micro and mesoporosity, remains a leading strategy for enhancing metallic dispersion.[97] Ni-Supported ZrO_2–Al_2O_3 showed higher catalytic activity and better stability than its γ-Al_2O_3 counterpart, reflecting the acidic/basic properties and enhanced CO_2 adsorption of zirconia.[98] The highly dispersed ZrO_2 was claimed to inhibit the formation of nickel aluminate-like phases, enhancing the dispersion of Ni species, and facilitating the reduction of NiO. In comparison, Ni incorporation in ceria has showcased unprecedented activities and CH_4 selectivity close to 100% at 340 °C and atmospheric pressure.[99,100] The superior performance can be quickly gauged in Fig. 7 when CeO_2-supported Ni catalysts are compared with other state-of-the-art materials (*cf.* Table 1 for detailed information on the results in Fig. 7). The activity boost over CeO_2-supported Ni has been ascribed to its reducibility, the presence of oxygen vacancies and oxygen storage capacity, and the emerging interactions with Ni determine the morphology, size, dispersion, and electronic properties of the incorporated NPs. DFT calculations have suggested the superior activity of CeO_2(110) as compared to both (100) and (111) phases since oxygen vacancy formation is more likely over the former.[101] The presence of Ce^{3+}/Ce^{4+} ion pairs and oxygen vacancies effectively promotes CO_2 activation;[102] these assumptions were corroborated by *in situ* FT-IR and *in situ* XPS results evidencing the promoted generation of active CO intermediate species.[99] The preparation of NiO-included mixtures of metal oxides, *e.g.*, mesostructured NiO–CeO_2 synthesized using a surfactant template method, using SBA-15 as a hard template, or directly mixing NiO with hard template-individually prepared CeO_2, has served as an approach in the synthesis of Ni-based metal oxides.[99,103,104] The hindered sintering of the resulting narrow metal Ni, formed from the reduction of NiO, was ascribed to their strong interactions with the ceria support.

The above findings conspicuously highlight the mechanistic implications of the interactions between the metal and the selected support. While recently assessing the suitability of less

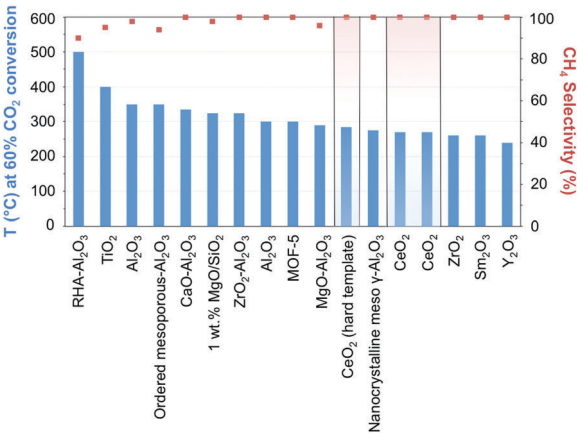

Fig. 7 Performance of Ni-based catalysts in t-CO_2RR to CH_4, tentatively compared on the basis of the temperature necessary to achieve *ca.* 60% CO_2 conversion. The highlighted results indicate the overall superior performance of Ni/CeO_2 catalysts in the literature. Further details and respective references have been conveniently summarized in Table 1.

explored oxides, Muroyama reported CH_4 yields at 250 °C following the order Ni/Y_2O_3 > Ni/Sm_2O_3 > Ni/ZrO_2 > Ni/CeO_2 > Ni/Al_2O_3 > Ni/La_2O_3.[43] The notability of these catalytic systems, in particular, Ni/Y_2O_3, is underscored by their activity, which is superior to even Ni/CeO_2. The nature of the formed intermediates examined by *in situ* infrared spectroscopy was claimed to depend on the selected support. In detail, CO species could be detected over Ni/Al_2O_3, whereas only carbonates were found over Ni/La_2O_3. Over Ni/Y_2O_3, considering the higher catalytic activity for CO_2 methanation and the rapid decomposition of formate species, the latter were proposed to serve as intermediates in the reaction (Fig. 3).

Basic and redox active promoters have been shown to improve CO_2 adsorption in Ni-based catalysts to prevent sintering of the active material and to increase its reducibility.[105,106] The incorporation of alkaline Mg species into an ordered mesoporous Al_2O_3-based framework (Mg/Al molar ratios in a wide 0–10% range) *via* one-pot evaporation-induced self-assembly (EISA) unveiled increased surface basicity, which could intensify the chemisorption and activation of CO_2 and enhance low-temperature catalytic activity.[107] Despite finding suitable application toward the production of long-chain hydrocarbons (Section 2.2.2), Fe has been proposed as a second metal to improve the performance of Ni in CO methanation, according to both experimental and density functional theory calculations.[108–110] In line with the above, Al_2O_3-supported Ni, Cu, Fe and corresponding Ni-based alloys prepared with the same total metal loading and varying Ni : Cu and Ni : Fe ratios were recently investigated for CO_2 methanation.[111] The resulting alloys exhibited lower particle diameter and sharper particle size distribution. At Ni : Cu and Ni : Fe ratios of 3 : 1, these catalysts showed opposite activity trends when compared with a Ni/Al_2O_3 reference, with Ni:Fe-based Al_2O_3 showing a 3-fold enhancement of the reaction rate.

Cobalt-based catalysts. As representative materials in the conventional LTFT using syngas, Co-based catalysts were considered candidates in CO_2RR toward long carbon-chains. When switching the reaction feed to a mixture of CO_2 and H_2, traditional Co-based FT catalysts were, however, shown to not lead to the anticipated ASF product distribution obtained under syngas atmosphere. Instead, products with low C/H ratio, and a favored CH_4 formation with a decline in chain growth, have been reported due to the slow adsorption rates of the thermodynamically and chemically stable CO_2 on the surface of the catalyst.[112] With a relatively low RWGS activity for CO generation,[113,114] the equilibrium constraints for the reverse CO shift reaction require severe operating conditions and relatively high temperatures.[115] Observed CO vibrations in FT-IR studies were postulated to solely reflect transition states during the conversion of CO_2 to $-(CH_2)_n-$ rather than formed CO species.[116] The high temperatures applied in the first step of the reaction (RWGS) lead, however, to the primary formation of CH_4 over Co-based catalysts. Conversely, the possibility of working at lower temperatures to favor the extension of the carbon-chain results in lower overall reaction rates, requiring larger reactor volumes and extended gas recycling rates. Literature findings have thus underlined not only the importance of the incorporated components to direct the RWGS for CO production but also the required optimization of the operating conditions for each reaction step in the overall mechanism, when the atmosphere is skewed toward CO_2. The latter is particularly difficult with different feed gas ratios of H_2 and CO_2 (3 : 1, 2 : 1, and 1 : 1) and operating pressures (ranging from 450 to 150 psig) showing only minor effects in directing the desired product distribution.[112] Despite the suitability of the Fe-based catalysts introduced in Section 2.2.2 toward long-chain hydrocarbons, mixtures of Fe and Co and Fe–Co alloys have shown limited enhancement compared to the individual metals.[117,118]

Following early reports on Co/SiO_2 prepared by incipient wetness impregnation[60] and studies on high-purity Co foil,[119,120] the application of Co-catalysts has since emerged as a valuable and cost-effective route to producing CH_4 with high activity and selectivity. In line with the advantageous acid/basic properties of ZrO_2 outlined above,[98] Song has recently claimed the emergence of a new Co–Zr phase with a thickness of *ca.* 1–2 nm at the Co–ZrO_2 interface.[121] These claims were corroborated by representative TEM photographs unveiling lattice fringes with no correlation with ZrO_2, Co^0, or Co_xO_y, and XPS results suggesting the presence of oxygen vacancies in ZrO_2-supported materials but not in the Al_2O_3 counterparts (Fig. 8). The bonding between Co species and surface Zr atoms was claimed to become stronger, and therefore more stable upon reduction, which, in return, led to a re-dispersion of Co^0 on ZrO_2. The resulting high activity at 400 °C (92.5%) superior to SiO_2 (80.1%), Al_2O_3 (77.8%), and SiC-supported counterparts (77.5%), a CH_4 selectivity of 99.9% and high stability up to 300 h were reported. Other remarkable results were recently reported, with Co-based porous carbon catalysts fabricated using a ZIF-67 zeolitic imidazolate framework as a template, with controlled morphology from cubic to rhombic dodecahedron, and particle size in the 150 nm to 1 μm range.[122]

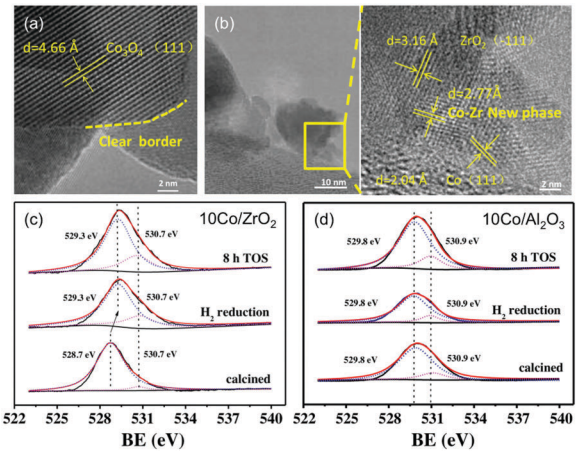

Fig. 8 (a) TEM images of calcined catalyst precursors Co_3O_4/ZrO_2 and (b) the corresponding reduced catalyst Co/ZrO_2. (c) and (d) are the O 1s XPS spectra for the Co/ZrO_2 and Al/Al_2O_3 catalysts calcined, following H_2 reduction, and after 8 h on stream. Readapted with permission from ref. 121. Copyright 2018 Elsevier B.V.

The hierarchical structure suppressed the sintering of the 7–20 nm-sized Co NPs, with high CO_2 conversion (52.5%) and CH_4 selectivity (99.2%) at 72 000 mL g^{-1} h^{-1} and 270 °C.

Exploiting synchrotron-based *in situ* characterization techniques such as XANES and XPS, Somorjai demonstrated that product distribution could be tuned depending on the support and oxidation state of cobalt.[123] The authors observed that 10 nm Co NPs on TiO_2 or SiO_2 could not be reduced at 250 °C, with complete reduction only being achieved at 450 °C. Interestingly, CoO on TiO_2 unveiled 10-fold superior CO_2RR rates compared to fully reduced cobalt. Inversely, the activity of cobalt supported on SiO_2 showed a higher turnover frequency than Co^0. In previous works, the authors had reported model Co-based catalysts with particle size in the 3–10 nm range prepared using colloidal chemistry in the absence of trioctylphosphine oxide, a capping ligand claimed to result in phosphorus poisoning of the metal surface.[124] Nitride Co_4N/γ-Al_2O_3 samples prepared by NH_3-temperature programmed reaction revealed superior activity for CO_2 (and CO) conversion compared with Co^0-based counterparts.[125] The formation of a Co_4N phase led to a strong metal–support interaction modulating the metal particle size and dispersion, and enhanced the adsorption capacity of the catalyst, as confirmed by H_2, CO, and CO_2-TPD.

Establishing synergies in metal-based hybrid catalysts. Structural and chemical effects on the intimacy of Co and other metal NPs as FT catalysts have long been investigated.[126,127] An intimate contact between two metals modifying the local band structure, ensemble-type geometric effects, prevention of deactivation by carbonaceous deposits, and improvement in the reducibility of Co have been suggested. A similar strategy has been applied in t-CO_2RR using either Pd or Pt co-catalysts. Using *in situ* NEXAFS spectroscopy, Somorjai suggested that H atoms dissociated on well-defined monometallic Pt NPs deposited near Co centers could be transferred to the latter *via* long-distance H-spillover and surface diffusion across silica, facilitating Co reduction (Fig. 9).[128,129] The close intimacy found between individual Pt and Co NPs could enhance CO_2RR rates up to a factor of 6 per Co surface atom. The authors further synthesized CoPt bimetallic NPs with controlled size and composition supported on MCF-17, evidencing Pt segregation under a reducing hydrogen atmosphere for the advantageous application in CO_2RR to CH_4.[130] Recently, a perovskite-structured $BaZrO_3$-supported catalyst corroborated the cooperative H-spillover between the Pt and Co centers, with CO_2 preferentially dissociating on Co and H_2 dissociating occurring on Pt.[131] The interaction could be further enhanced through the atomic decoration of Pt on the surface of Co. Additionally, taking the strong interaction between Co and the $BaZrO_3$ support into account, a 6-fold increase in CH_4 formation rate was found in comparison to previously studied γ-Al_2O_3 supports at 325 °C. At the same temperature, the methane selectivity reached 80%, in comparison to only 43% over γ-Al_2O_3.

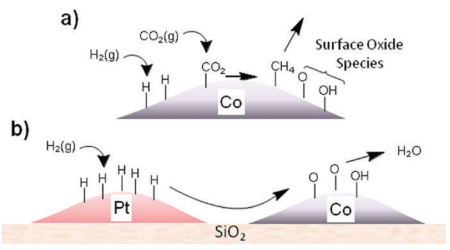

Fig. 9 (a) Schematic representation of the production of surface oxide species during CO_2 methanation and (b) transfer of adsorbed hydrogen from Pt to Co *via* a spillover mechanism to re-reduce the cobalt oxide surface, releasing water. Reprinted with permission from ref. 128. Copyright 2014 American Chemical Society.

Notwithstanding the enhanced reducibility of the resulting catalysts with a superior number of metallic sites, the high cost of incorporated noble metals still demands the development of novel synthetic strategies hindering the corresponding metal loadings. The recently reported Pt-promoted Co–Al_2O_3 (0.03–0.43 wt% Pt) synthesized by double flame spray pyrolysis showed significant improvement in the reducibility of Co_3O_4 and high t-CO_2RR activity as compared to a pristine Co–Al_2O_3.[132] Ruiz *et al.* demonstrated that a synergistic effect could be found with physical mixtures of Pd (5 wt%) and Rh (2 wt%)-based γ-Al_2O_3 catalysts at temperatures between 150 and 200 °C.[133] Similarly, H_2 was activated over Rh/γ-Al_2O_3, but the activation of CO_2, its dissociation to adsorbed CO*, and subsequent hydrogenation to CH_4 were believed to take place on both phases. Activated H species on Rh/γ-Al_2O_3 were claimed to migrate and react with the adsorbed CO* on Pd/γ-Al_2O_3, leading to selective CH_4 formation. A similar strategy was considered by mechanically mixing Rh/γ-Al_2O_3 and Ni/activated carbon.[134] The production of methane was significantly higher than the theoretically predicted values, considering the individual performances, and attributed to an *in situ* supply of hydrogen by the Ni-based catalyst. The suggested hydrogen spill-over further maintained Rh particles in a metallic state necessary for the reaction.

2.2.2. Catalysts favoring t-CO_2RR to longer carbon-chains. The favored synthesis of longer carbon-chains has been predominantly achieved in t-CO_2RR platforms following the parallelism of CO-based FT technologies. This has led to the limitation of emerging results of interest since the t-CO_2RR is plagued with additional challenges when the atmosphere is switched to CO_2: (1) CO_2 is a poison for CO hydrogenation catalysts; (2) the poisonous effect of water as a by-product during the reaction. Most importantly, however, is the need to guarantee the presence of suitable active centers capable of performing the RWGS to generate *in situ* CO* intermediates that are subsequently converted into hydrocarbons. The difficulty in optimizing the operating conditions for these consecutive steps reflects the unsuitability of Co-based catalysts for producing long-chain hydrocarbons, in accordance with an intrinsic poor activity for the RWGS. An interesting alternative could, therefore, be the design of catalysts with multiple optimized functionalities provided by active centers placed adjacently.

In this context, Somorjai and Yang have recently highlighted the importance of nanostructured catalysts using well-defined and characterized interfaces. Considering the incompatibility

of synthetic conditions of the materials of choice, the integration of all the desired components into one single NP is challenging and requires an elegant synthetic design. The authors, therefore, developed a well-defined CeO_2–Pt@mSiO_2–Co nanostructured catalyst for converting CO_2 into C_2–C_4 with high selectivity (60%), with no activity decay up to 40 h.[135] As suggested above, the Pt/CeO_2 interface plays the role of converting CO_2 and H_2 into CO, which could subsequently be reacted on conventional Co/mSiO_2 centers to yield hydrocarbons through an analogous FT process. The successful production of C_2–C_4 *via* a tandem process on a structurally well-defined catalyst additionally demonstrates the power of sophisticated structure control in multiple-step chemical conversions (Fig. 10). To date, the promising incorporation of optimized functionalities widely extending the library of catalysts in analogous CO_2-based FT processes has remained scarce, with the application of Fe-based catalysts being the main focus of the literature, as cautiously reviewed below.

Iron-based catalysts. The application of Fe-based catalysts, possessing the most favorable characteristics for a selective synthesis of long-chain hydrocarbons to date, follows a parallelism with conventional FT platforms under CO_2 atmosphere. In the conversion of syngas, Fe-based catalysts are conventionally applied in high-temperature FT synthesis, leading to an olefinic product distribution notably skewed to low carbon number. According to representative syncrude compositions on a mass basis listed by de Klerk, *ca.* 35% and 33% of the resulting crude corresponds to the C_2–C_4 fraction (olefins and paraffins) and to the C_5–C_{10} naphthas range.[54]

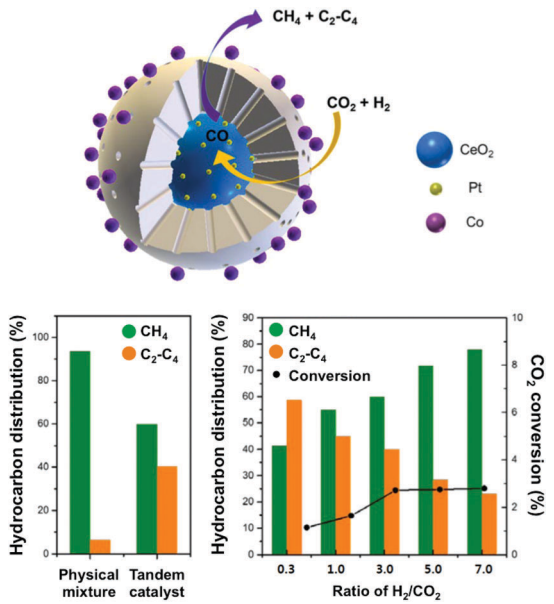

Fig. 10 (top) Schematic representation of a well-defined nanostructured catalyst, CeO_2–Pt@mSiO_2–Co, for t-CO_2RR to C_2–C_4 hydrocarbons using two metal–oxide interfaces. The catalytic performance of the prepared tandem catalyst is compared with a physical mixture of the evaluated components (left). The impact of the H_2/CO_2 ratio on the hydrocarbon distribution and CO_2 conversion (right). Adapted with permission from ref. 135. Copyright 2017 American Chemical Society.

The development of these catalysts for CO_2RR has followed the guidelines drawn *a priori* for CO-based platforms. Despite the inherent difficulty in understanding the mechanism and involved species behind CO_2RR, the phase reconstruction of Fe catalysts has been well documented to direct the presence of active sites needed to perform the two catalytic reactions in this process, *i.e.*, CO_2 and H_2 produce CO by the RWGS reaction, which further reacts with H_2 by FT synthesis to form hydrocarbons. The phase reconstruction of Fe catalysts, which is the subject of an intense debate, is dependent on the initial Fe_2O_3 particle size[136] and is induced in a series of designated episodes of self-organization, altering the composition and structure of the catalyst and prompting the continuous evolution of the resulting activity and product selectivity (Fig. 11).[137] The active centers, a complex mixture of iron phases, are generated when Fe oxide is exposed to the reactants, with the freshly reduced catalyst not being active in FT synthesis. Surface reconstruction unlocks a difficulty in classifying the active centers during the reaction, and most importantly, in quantifying said sites to calculate turnover numbers as a measure of the catalytic activity. Initial iron species, mainly α-Fe and Fe_3O_4, are believed to undergo phase transformation into an amorphous, and probably oxide, iron phase, active for the RWGS reaction, which strongly interacts with the support. Iron carbides, *e.g.*, Fe_5C_2, have been suggested as active centers in the hydrogenation of CO *via* the FT process.[138,139] The possibility of Fe_5C_2 species acting as the active phase in the conventional FT process has been long discussed.[140,141] In line with the above findings, attempts have been made to tentatively optimize the ratio between Fe_3O_4 and Fe_5C_2 species to adjust the product selectivity.[142]

The catalytic properties of Fe-based catalysts markedly depend on structural effects and on the strategic incorporation of promoters (*e.g.* K, Mn, Cu, and Ce) and the selection of supports, toward enhanced activity, product selectivity and stability. The particle size of Fe_2O_3 NPs was assessed using the confinement effect of an Al_2O_3 support with varying pore size.[143] The catalysts with fixed Fe and K-dopant contents (15 and 10 wt%, respectively) prepared by incipient wetness

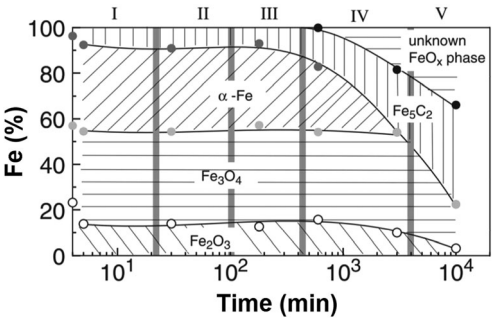

Fig. 11 Iron-phase composition as a function of time during the Fischer–Tropsch synthesis under CO_2 atmosphere, determined by Mössbauer spectroscopy. Data collected with a Cu–K-doped Fe–Al catalyst at 250 °C, 1 MPa, and H_2/CO_2 = 3. Reproduced with permission from ref. 138. Copyright 2003 Springer Nature.

impregnation exhibited Fe_2O_3 NP size and distribution determined by the corresponding Al_2O_3 pore size. Alumina with a pore system in the 7–10 nm-range and corresponding Fe_2O_3 particle sizes of 5–8 nm were the most active for CO_2RR to hydrocarbons. Narrower particle diameters were found to be unsuitable on account of the weak reducibility of smaller iron particles. Recently, bare Fe_2O_3 prepared *via* a template-assisted method and precipitation method and with easier reducibility, led to a greater ability for the formation of catalytically active iron carbides.[144] Other works of significance have been recently reported using a high surface area iron-based catalyst prepared by the thermal decomposition of ammonium glycolate complexes.[142]

Despite inducing enhanced light olefin selectivity as compared with SiO_2 and Al_2O_3-supported catalysts, MgO leads to poor dispersion of the incorporated Fe active species. These findings inspired later works on SiO_2–MgO and Al_2O_3–MgO.[145,146] Upon the incorporation of MgO up to a 20 wt% loading in Fe–K/Al_2O_3–MgO catalysts, CO_2 conversion, total hydrocarbon selectivity, and the selectivity of C_2–C_4 olefins and C_{5+} species displayed a remarkable increase with a continuous increase in the MgO content.[146] MgO was confirmed to play a key role in the nature of the Fe species present, determining the resulting product yield. In Fe-based catalysts, the presence of ceria has been conspicuously assessed either as a support or as a promoter. The morphology of supported Fe/CeO_2 catalysts markedly determined the CO_2 conversion, the methane to hydrocarbon selectivity, and the olefin-to-paraffin ratio,[147] with a selective exposure of different crystal planes directing the metal–support interaction and the reactivity of emerging Fe-species. Ceria nanorods exhibited the highest hydrocarbon selectively, whereas higher olefin-to-paraffin ratios were achieved on ceria cubes.

Carbon nanotubes (CNT) have been extensively applied as supports in the conventional CO-based FT synthesis reaction, with a higher selectivity to olefins, improved activity owing to an enhanced catalyst dispersion, and low deactivation rates.[148,149] In the conventional FT synthesis, pioneering results were reported over Fe-supported carbon nanofibers with remarkable C_2–C_4 olefin selectivity.[150] Under CO_2 conditions, Fe@CNT have also received attention.[151] To overcome a number of disadvantages for the industrial applications of CNT in powder form, including a high-pressure drop for gas phase processes and agglomeration, Fe NP–carbon nanotube arrays grown on monoliths were evaluated for CO_2RR.[152] Detailed studies of the catalyst *via* HR-TEM, EDX and XRD uncovered the detailed evolution of the Fe NP throughout the process, with the formation of iron carbides, suggesting the presence of magnetite species and the surprising absence of iron oxides.

To increase the yield of hydrocarbons and overcome important drawbacks in the applicability of these materials, a number of dopants (*e.g.* K, Mn, Cu, and Ce) are often incorporated in the rational design of Fe-based catalytic systems. The extensive research carried out along these lines has additionally benefited from studies carried out under H_2 and CO atmosphere in conventional FT synthesis. Therefore, tailored and optimized product distribution and an enhanced RWGS activity – limited *a priori* when compared with Co-based systems – have been reported. These results have permitted similar performances in the synthesis of hydrocarbons using either CO_2 or CO as a feed.[115] Potassium has been shown to simultaneously increase the chemisorption of CO_2, decrease the adsorption of H_2, and enhance the activity for CO formation,[153] thus hampering CH_4 formation and favoring chain growth.[21,114] In addition, K-moieties have been proposed to accelerate the generation and assure the stabilization of the Fe_5C_2 phase, favoring the modified FT reaction. By simultaneously facilitating the RWGS reaction and carbon-chain propagation, high selectivity (*ca.* 60%) toward long-chain hydrocarbons has been achieved along with a significant shift in olefin production in the C_2–C_{5+} range up to *ca.* 80%.[58,154–156] Recently, Herskowitz shed additional light on the effect of potassium (2 wt%) on both Fe–Al–O oxide and Fe_5C_2 carbide materials, formed during CO_2 hydrogenation.[157] The incorporated potassium enhanced the RWGS rate of reaction on the oxide phase 10-fold as compared to the unpromoted oxide. The results were correlated with an increase in the Fe^{2+}/Fe^{3+} ratio determined by XPS, hinting at the role of oxygen vacancies as active sites for the first reaction step of t-CO_2RR. Conversely, potassium suppressed the methanation rate on the carbide catalyst by 5-fold, while increasing the formation of C_{2+} hydrocarbons by 1.4-fold. The synergism that emerged in the presence of potassium has been ascribed to the presence of potassium alanate ($KAlH_4$).[155] Prior to the reaction, the complete decomposition of KNO_3 to other phases *e.g.*, K_2O and potassium aluminate ($KAlO_2$) were observed during heat treatments above 500 °C.[158] The latter appears to bind hydrogen in its structure to form $KAlH_4$, leading to a lower surface coverage of adsorbed H species suppressing the hydrogenation of olefins to paraffins.

The incorporation of Mn and Cu-dopants improves the reducibility of FeO_x species, the distribution of iron species, and the surface basicity.[57,159] Mn favors the reduction of iron oxides and the carburization and dispersion of Fe_2O_3,[160] while suppressing CH_4 and favoring an increase in the formation of unsaturated high-chain hydrocarbons, with a higher olefin/paraffin ratio.[155] However, Mn-loading has been shown to remain effective over a limited concentration range, with a continuous content increase leading to an eventual blockage of iron active centers. Mesoporous Mn–Fe oxide (0.05MnFe) catalysts exhibiting moderately high BET area, showed enhanced performance under fixed conditions (20 bar, 340 °C, $CO_2 : H_2 : N_2 = 23 : 69 : 8$ (molar)) with reduced CO and CH_4 formation and improved selectivity to C_2–C_5 and C_{6+} hydrocarbons, accompanied by oxygenates formation.[161] Enhanced performance, in terms of hydrocarbon production with copper-promoted samples, has been claimed to be the result of a greater number of carbide species present when the evaluated iron catalysts reach a steady state during operation.[162] During the hydrogenation of CO, the incorporation of copper was claimed to provide active sites for hydrogen activation and dissociation, dramatically accelerating the reduction of hematite to magnetite, with a larger number of magnetite nuclei being formed in this case.[163] Under CO_2 conditions, the presence of a copper surface enriched with

hydrogen was however demonstrated to favor CH_4 formation, which could be subsequently inhibited with the incorporation of potassium.

In the design of catalytic systems for t-CO_2RR, other co-catalysts and dopants have been investigated. In accordance with the high activity of ceria-supported catalysts for CO_2 methanation, ceria-promoted Fe-based catalysts have demonstrated enhanced activity and selectivity to C_2–C_5 olefins.[164] As mentioned above, the synergetic effect is solely achieved if the incorporation of ceria, herein reflected in its corresponding particle size, is optimized to minimize the blockage of active Fe sites. Given the mechanistic similarities established between both catalytic processes, catalysts used in CO-based FT (*e.g.*, Ru) have often been considered to be relevant, in an attempt to direct product selectivity to longer chains. Choung claimed that Ru incorporation could increase the probability of α-olefin readsorption in a Fe–K/γ-Al_2O_3 catalytic system, enhancing the overall activity and skewing product selectivity to higher C_{5+} hydrocarbons.[165]

2.2.3. Effect of the support: concluding remarks. In this review, the abovementioned exploratory works have repeatedly highlighted the key role of the nature of the support in the activity, selectivity, and stability of the resulting catalyst. Seminal studies on supported metal NPs demonstrated that the specific activity of Pd/Al_2O_3 could be enhanced up to 70-fold and 35-fold as compared with large unsupported Pd crystallites and Pd/SiO_2 catalysts, respectively.[85] These observations, underlining the significance of the incorporation and choice of a support, further agreed with later evaluated Pd-based and Rh-based systems with activities following the trend TiO_2 > Al_2O_3 > SiO_2[166,167] and the studies of Worley.[168] Since then, the selection of the support, *e.g.*, Al_2O_3,[85] SiO_2,[52] zeolites,[169] ZrO_2,[170] TiO_2,[64] CeO_2,[100,171] La_2O_3,[172] MgO,[173] Nb_2O_5,[80] perovskites,[131] and carbon materials, as well as corresponding crystal structures[75,76] and surface areas,[174] have been shown to determine the morphology and dispersion of the incorporated active phase and play a key role in the resulting catalytic performances. Solvents used for impregnation, metal loading, and calcination temperatures have additionally been demonstrated to influence the nature of the precursor species formed on the selected supports.[173] The impact on the stability of the resulting hybrid materials is addressed in Section 2.4.

Metal–support interfaces have been established in this review to play a central role in governing both the electronic and chemical properties of the resulting catalytic systems, governing the surface chemistry in t-CO_2RR platforms, and directly impacting the charge transfer and mass transport in the activation of reactant molecules.[77] Unveiling the nature and effects of these interactions on active site-dependent reaction mechanistic pathways and product selectivity has been covered widely in the literature.[175,176] *In situ* studies on Ru-loaded anatase and rutile TiO_2 have indicated that the former acts as a better catalyst for CO supply, while rutile TiO_2 is more effective in the hydrogenation of adsorbed CO intermediates.[47] Zhang recently suggested that adsorbed CO_2 could react with the hydroxyl groups of rutile TiO_2 to produce CO *via* the formation of formate species, whereas the dissociation of adsorbed CO could then proceed as assisted by the presence of adsorbed H provided by the incorporated metal NPs.[177] In the same year, Wang used *operando* XANES, IR, and Raman to disclose the generation process and evolution during the reaction of Ce^{3+}, surface hydroxyls, and oxygen vacancies in a Ru/CeO_2 catalyst.[178] Steady-state isotope transient kinetic analysis-type *in situ* DRIFT infrared spectroscopy offered proof of CO_2 methanation following the formate route (Fig. 3), with the rate-determining step being the dissociation of the latter, catalyzed by oxygen vacancies. However, over an α-Al_2O_3 supported counterpart and in the absence of oxygen vacancies, CO_2 methanation was claimed to undergo the RWGS + CO-hydrogenation pathway (Fig. 3). The reducibility of the metal oxide was thus expected to play a key role in the rate-limiting cleavage of the second C–O bond, known to be dependent on the ratio of co-adsorbed CO* and H*.[63] The combined results of H_2 temperature-programmed reduction, quantitative H_2 and CO chemisorption, *in situ* DRIFTS, and CO_2 methanation kinetics revealed that CO-coverage on a Ru-based catalyst decreased with the support reducibility. For the irreducible Al_2O_3 support, the Ru particles were quasi-saturated with CO at low temperatures and the reaction was limited by the competitive Langmuir-type co-adsorption of H_2. The ZnO support led to the lowest Ru–CO coverage associated with a weak CO adsorption and the reaction was dominated by the reverse water-gas shift reaction. CeO_2 showed Ru–CO coverage between Al_2O_3 and ZnO, ensuring H_2 dissociation and sufficiently high Ru–CO adsorption strength. The increasing interest in ceria as an excellent CO_2 methanation catalyst has prompted additional studies on other reducible metal–oxides, *e.g.* In_2O_3 and Ga_2O_3.[80,171,179,180]

Whereas limited catalytic activity was found over individual metal oxide systems as sole t-CO_2RR catalysts, a continuous focus on the properties of the support has shed some light on works assessing the properties of new materials as unconventional t-CO_2RR catalysts. Transition metal carbides, with desirable behavior for reactions involving CO_2 and analogous properties to those of hydrogenating precious metals, are interesting examples. Molybdenum carbide is cost-effective, exhibits the required dual functionality and is expected to behave similarly to reducible oxides.[181] Alternatively, Ajayan and collaborators recently reported the use of N-doped graphene quantum dots as metal-free catalysts in the selective synthesis of CH_4 above 380 °C.[182] The located N-dopants at the edge-sites were claimed to markedly induce the thermocatalytic activity of these carbon-nanostructures, with increasing N-content, leading to lower onset reaction temperatures, higher CO_2 conversion, and improved CH_4 selectivity. Most importantly, the catalyst performance was crucially dependent on the observed doped N-configurations and corresponding defect density.

2.3. Methanol-mediated routes toward long-chain hydrocarbons

Serving as an alternative to modified Fe-based CO_2RR catalysts through an analogous FT process, CO_2 has been converted into linear hydrocarbons through intermediate steps involving the synthesis of methanol by methanol-mediated approaches.[183,184]

In the proposed platforms aligning two individual and well-established reactions, CO_2 is first converted to methanol, followed by the conversion of the latter to hydrocarbons.[185] Complex catalytic formulations involving Cu-based and/or other metal-based and metal oxide-based components have shown promising performance in methanol synthesis from CO_2.[186–189] Clear inspiration has been garnered from the typical Cu–ZnO–Al_2O_3 industrial catalysts for the synthesis of CH_3OH from syngas,[190] with a highly efficient Cu–ZnO–Al_2O_3–ZrO_2 arising as a promising catalyst.[191]

The conversion of methanol to hydrocarbons has been thoroughly investigated in the literature, with the C–C bond formation being demonstrated over zeolite or zeotype catalysts. The methanol-to-hydrocarbons (MTH) process can be additionally turned into the production of gasoline-rich (methanol-to-gasoline, MTG) or olefin-rich (methanol-to-olefins, MTO) product mixtures by the proper choice of catalyst and reaction conditions. Product selectivity is directly derived from the imposed shape-selectivity created inside the micropores of the selected crystalline structures. How the dimensionality and pore size of selected catalysts controls the product selectivity is a topic of heightened interest that is summarized elsewhere.[192] In general, zeolite H-ZSM-5 (MFI topology) with a tri-dimensional interconnected channel system defined by 10-membered ring pore apertures has been utilized in the synthesis of hydrocarbons.[193] When the MTO pathway is preferred, the silicoaluminophosphate SAPO-34 with narrow channels (8-membered ring) and wide cages is preferably employed.[194]

The expectedly effective catalytic conversion of CO_2 into gasoline may be attained through a one-pass operation using a serially connected flow-type reactor.[183] Such results suggest the promising potential for industrial application but inconveniently rely on consecutive process steps. Coupling both catalytic functionalities in a one-step process has emerged as an alternative that has been receiving increasing attention. In spite of the considerable efforts made in the development of composite catalysts, the results to date have been based on the somewhat disadvantageous design of complicated catalytic systems and remain rather unpromising. Compared with analogous technologies using syngas, the current state-of-the-art methanol-mediated t-CO_2RR emphasizes the limiting occurrence of the RWGS reaction leading to undesirably high CO yields (up to 80%) with the prepared bifunctional catalysts. Major drawbacks in both MTG and MTO technologies such as high cost and fast catalyst deactivation are expected during a methanol-mediated t-CO_2RR to hydrocarbons. In addition, the formed H_2O molecules dramatically affect the stability and activity of the incorporated zeolites during the second step of the consecutive processes. Upcoming research works clearly demand strategies that involve more than the simple incorporation of optimized components for both desired reactions. The desired product selectivity is additionally expected to be considered in the rational design of these hybrid catalytic systems. The effect of the zeolite structure for HY (a tridimensional large pore zeolite with a 12-membered ring pore aperture) and H-ZSM-5 was assessed in Fe–Zn–M-based catalysts toward the maximization of the yield for isoalkane formation.[195] The Fe–Zn–Zr/HY catalyst was confirmed to be efficient for the highly selective production of isobutane, whereas its H-ZMS-5 counterpart yielded enhanced C_{5+} hydrocarbon formation. The latter further unveiled a ratio of branched hydrocarbons over 90%, which is highly suitable for high-octane gasoline.

The production of olefins, which has achieved notable success in analogous technologies using syngas,[150,196,197] has unlocked low yields at low overall CO_2 conversion levels to date, while alkane formation following alkene hydrogenation has also been reported. Recently, the thermodynamic and kinetic coupling between the components of a ZnZrO/SAPO-34 tandem catalyst, fabricated with a ZnO–ZrO_2 solid solution and a Zn-modified SAPO-34 zeolite, achieved a selectivity for lower olefins as high as 80–90% among hydrocarbons at 12.6% CO_2 conversion, with only 3% CH_4 being formed (Fig. 12).[198] Methanol conversion on SAPO-34 or ZnZrO/SAPO-34 produced lower olefins with high selectivity (over 90%), corroborating the assumption that the zeotype phase was the catalyst for MTO conversion. The CO_2RR technologies for producing short-chain olefins *via* methanol-mediated routes remain promising as compared with modified Fe-based FT platforms, being at least partly commercially established (MTO) and directing a more tuned and narrow distribution of the emerging short-chain olefins. In addition, the development of multifunctional catalysts incorporating adjacent active sites combining the fingerprints required over the involving catalytic steps is expected to significantly enhance the potential of these systems in the future.

In particular, a bifunctional catalytic system incorporating the partially reduced In_2O_3 and H-ZSM-5 zeolite has recently unveiled pioneering performances in the direct and highly selective production of fuels in a gasoline-relevant range, minimizing the formation of CO and undesirable side-products (Fig. 13).[199] C_{5+} selectivity reached 78.6%, with only 1% for CH_4 selectivity at a CO_2 conversion of 13.1% under stable conditions over 150 hours. As discussed above, the generated shape selectivity within the pore architecture of the ZSM-5 catalyst facilitated the attained product selectivity. The CO_2RR could be manipulated

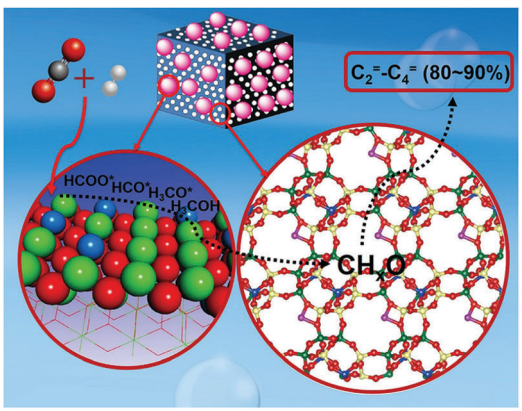

Fig. 12 Proposed mechanism for the formation of olefins with high selectivity over a ZnZrO/SAPO-34 catalyst. Adapted with permission from ref. 198. Copyright 2017 American Chemical Society.

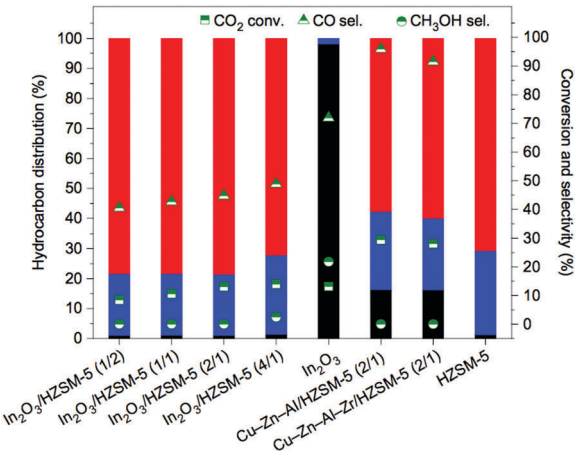

Fig. 13 t-CO_2RR performance over various bifunctional catalysts containing Cu-based components or In_2O_3 and HZSM-5 with different mass ratios, as shown in the parentheses, and the stand-alone In_2O_3 catalyst (reaction conditions, 340 °C, 3.0 MPa, 9000 mL h^{-1} g^{-1}, $H_2/CO_2/N_2$ = 73/24/3). Results over HZSM-5 obtained for the direct conversion of methanol (liquid CH_3OH 0.855 mL h^{-1} g^{-1}). Maximum hydrocarbon selectivity to C_{5+} (red), C_2–C_4 (blue), and CH_4 (black) is maximized over In_2O_3/HZSM-5. Cu–Zn–Al-based and Cu–Zn–Al–Zr-based catalysts represent materials of choice in the industrial methanol synthesis from syngas and in CO_2 hydrogenation, respectively. Reproduced with permission from ref. 199. Copyright 2017 Springer Nature.

by controlling the surface structure of the In_2O_3 and the mass ratio between both catalytic phases. The proximity of the two components was additionally shown to play a crucial role in suppressing the undesired RWGS reaction and obtaining a high C_{5+} selectivity.

2.4. Stability issues

Along with the costs of implementation and production, the lifetime of a catalyst is vital in determining the technological practicality of the thresholds. In the t-CO_2RR, metal stability against poisoning, sintering, and coke deposition are the main issues investigated when evaluating the catalytic decay of these platforms. Nonetheless, the stability of these systems further depends on the overall catalyst design (*e.g.*, selected support, choice of the incorporated metal, and eventually added promoters), utilized feedstock (*e.g.*, CO_2 purity and partial pressure of the gas) and operating conditions applied during catalytic assessment (*e.g.*, temperature, pressure, and gas hourly space velocity). The poisoning of metal-loaded catalysts derived from the presence of sulfur compounds in industrial feedstocks has prompted decades of research in the use of adsorbents for effective sulfur removal.[200,201]

Large surface areas and the rational design of hierarchical supports have been pinpointed in most attempts to hamper the catalytic decay related to metal sintering and coke deposition. The morphology of the support has been additionally detailed to impact the morphology of the incorporated metal NPs,[96] promote NP dispersion, determine the adsorption properties of the resulting catalyst, and to induce product selectivity.[174] In methanol-mediated routes for long-chain hydrocarbon synthesis, zeolites and zeotypes with narrow pore size and constraint effects that induce shape-selective properties additionally serve as a bridge in the selective synthesis of the desired products.[193] However, the induced confinement of these crystalline microporous aluminosilicates simultaneously prompts severe molecular diffusion limitations, leading to rapid deactivation and compromising the industrial practicality of the zeolite.[194] In addition to the dramatic decrease of the full application of the zeolite, pore blockage undesirably affects the selectivity of the catalyst as the reaction is skewed to the surface of the material where shape-selectivity is absent. Reducing the zeolite crystal thickness has been, in this context, reported to be advantageous in reducing diffusion path lengths and remarkably hindering catalytic decay. Inter- or intra-crystalline mesopores have been generated in zeolites by the use of a hard template or a soft template, self-assembly of nanoslabs, packing of nanocrystalline zeolites, or post-synthetic demetallation treatments used to render internal active sites more accessible.[202] Along the same line of thought, twenty years of active research on ordered mesoporous materials have found suitable applications in CO_2RR toward the facile dispersion of metal NPs with hindered tendency toward deactivation. Larger surface areas and pore volumes, uniform pore distribution and enhanced pore interconnectivity of the resulting architectures have long been highlighted in a wide range of applications toward a better interaction between the metal–oxide and the support, resulting in high metal dispersion. Improved molecular diffusion, suppression of sintering and agglomeration of metal atoms, and hindered coking during the reaction even at high temperatures are to be expected.

Finally, the encapsulation of metallic NPs is an efficient strategy for hindering deactivation due to both metallic particle sintering and coke formation.[203–205] Shape-controlled Pd NPs embedded in mesoporous silica shells showed no increase in particle size during the catalytic assessment and had greater stability toward sintering as compared with a Pd/SiO_2 counterpart prepared by wetness impregnation.[86] The above reports additionally highlight the advantage of encapsulating metal NPs as a valuable pathway to preserving superior catalytic performance. For instance, the activity of CO_2 methanation could be significantly enhanced by encapsulating small-sized (111) faceted Ni particles in metal–organic frameworks at 300 °C with high thermal stability demonstrated up to 200 h.[206] DFT calculations confirmed that the preserved plane had a lower potential energy barrier (10.0 kcal mol^{-1}) for CO_2 dissociation into adsorbed CO* and O* intermediate species when compared with the (200) facet (20.3 kcal mol^{-1}).

The loss of metallic surface has been thoroughly assessed under CO_2RR conditions, as it represents a crucial bottleneck in the application of promising catalytic systems. With stability being dependent on the choice of the incorporated metal NPs, Ru-based catalysts emerged as the most resistant to catalytic decay after being assessed over a wide temperature range. Ru NPs on TiO_2 prepared by a polygonal barrel-sputtering method were stable at 80 and 140 °C for 24 h, and up to one week at 180 °C.[73] TEM imaging revealed no change in the size

or size distribution of these incorporated NPs as compared with the as-prepared counterparts. Over a γ-Al_2O_3 support, Farrauto demonstrated cyclability runs introducing pre-treatment steps under H_2 prior to each CO_2RR cycle, which could serve as a valuable industrial strategy toward the extended stability of the evaluated catalysts.[207]

Regarding the significantly less stable Ni-based systems, Mirodatos showed that sintering on a SiO_2-supported catalyst can be ascribed to the formation and migration of highly mobile Ni subcarbonyl adspecies due to the interaction of Ni NPs with adsorbed CO*, prompting fast catalytic decay.[208] The catalyst, initially presenting a monomodal Ni particle size distribution, evolved toward a bimodal system consisting of small spherical and large faceted crystals, with the selective development of (111) planes under reaction conditions. In contrast, the formation of nickel carbide was suggested to decrease the concentration of the mobile subcarbonyl adspecies. Manipulating the inherent interactions between the (111) faceted incorporated metal NPs and supports serves as a valuable strategy for enhancing the metallic dispersion and hindering catalytic decay due to particle sintering and coke formation. $Ce_{0.72}Zr_{0.28}O_2$ mixed-oxide catalysts with high oxygen storage capacity, for instance, were able to notably enhance Ni dispersion (10 wt%) and further restrain the sintering of the metal, resulting in high stability on stream toward deactivation up to 150 h at 350 °C.[209] Similarly, 5 wt% Ni/2 wt% ceria/Al_2O_3 was reportedly stable after 120 h at 300 °C. A remarkable stability with only a 7% decay after 252 h at 300 °C was reported with a supported Ni nanocatalyst fabricated by the *in situ* reduction of the NiAl-LDH precursor.[210] The superior degree of Ni^{2+} dispersion in the LDH precursor could induce highly dispersed Ni NPs that are resistant to sintering, with the intrinsic topotactic phase transformation from the LDH matrix to the supported Ni NPs being proposed to ensure a strong anchoring effect.

In the desirable shift to long-chain hydrocarbons, although significant deactivation of Fe-based catalysts is mostly ascribed to the above-discussed issues related to poisoning from gradual coke deposition and obstruction of the active sites, the inherently formed water vapor has been shown to act as a poison in the t-CO_2RR, re-oxidizing the catalyst surface and altering the resulting product selectivity.[118,211] By removing or reducing these effects, the equilibrium at the Fe-based catalyst surface should favorably skew the production of CO or CH_4 to desired intermediates such as olefins.[212] An alternative approach is the utilization of *in situ* permselective silica membranes, as introduced in Section 2.5.[213] Fe-Based catalysts undergo inherent deactivation due to the undesirable phase transformation into the stable but non-active carbide (Fe_3C) formed by Fe_5C_2 carburization.[214] The optimization of the design of the Fe catalyst and a better understanding of the observed phase transformation is once again highlighted (Fig. 11). It is important to highlight that the stability of the applied catalysts significantly depends on the operating conditions and the reactor design, as discussed in the following section.

2.5. Reactors and process considerations

The t-CO_2RR technologies for either selective CH_4 production or long-chain hydrocarbons have been designed for the conversion of synthesis gas, according to the obvious parallelism in the proposed reactors when the atmosphere is switched to CO_2 as a feedstock. With the acquired knowledge on the catalytic chemistry of the above-discussed possible reaction pathways to convert CO_2 and these relatively well-established conventional technologies as a guideline, reprocessing development faces only minor technological barriers requiring engineering solutions for reactor design, implementation, and operation. Playing a role as important as the rational synthesis of optimized catalytic architectures, the control of operating conditions and key parameters in the design of t-CO_2RR reactors, *i.e.*, temperature, pressure, and space velocity, have been additionally demonstrated to substantially impact the resulting activity, product selectivity, and stability.[142,158] As expected, high reaction pressures, low-temperature operation favoring energy consumption, and high space velocities maximizing the reactor throughput are desired. The thorough energetic integration analysis is also of primary importance in the industrial prospect of thermochemically-driven catalytic platforms.

With t-CO_2RR being strongly exothermic, efficient heat management and heat removal are crucial requirements for facilitating stable hydrocarbon production to prevent the propensity of the reactor to overheat and lead to rapid catalyst deactivation by sintering and coking (mostly associated to CH_4 cracking), and to permit and effective utilization of the released heat.[207] Using a transient mathematical model, Simakov mapped a dynamic two-dimensional domain of the two crucial operating parameters, *i.e.* space velocity and cooling rate, to assess the effect of the selected operating conditions during CO_2 methanation in a heat-exchanger type reactor.[215] Scanning the reactor performance over extended ranges of space velocities and heat removal rates showed a non-trivial dynamically evolving map; however, the model suggested an enhancement of CH_4 yield with controlled thermal management. Interestingly, the high pressures that are favorable for CH_4 production and beneficial for practical applications were suggested to lead to a faster catalyst deactivation due to the higher partial pressure of CH_4 causing susceptibility to cracking and leading to coke formation.

The emerging carbon deposition has been well documented to deactivate the catalyst by fouling the catalyst surface, blocking catalyst pores, and disintegrating the catalyst support. Heat-exchanger-type reactors are thus of crucial importance, not only toward desirable heat management but also for the energetic reutilization of the generated heat during the reaction. CO_2 methanation is preferentially assessed in fixed-bed reactors and reports on microchannel and monolith reactors as design solutions have been valuable. However, directing the reutilization of CO_2 to long-chain hydrocarbons has been thoroughly explored in either conventional fixed-bed, fluidized bed, or three-phase slurry configurations (Fig. 14).[217] The parallelism found with the conventional FT fluidized bed or three-phase slurry reactors, extensively investigated in the past

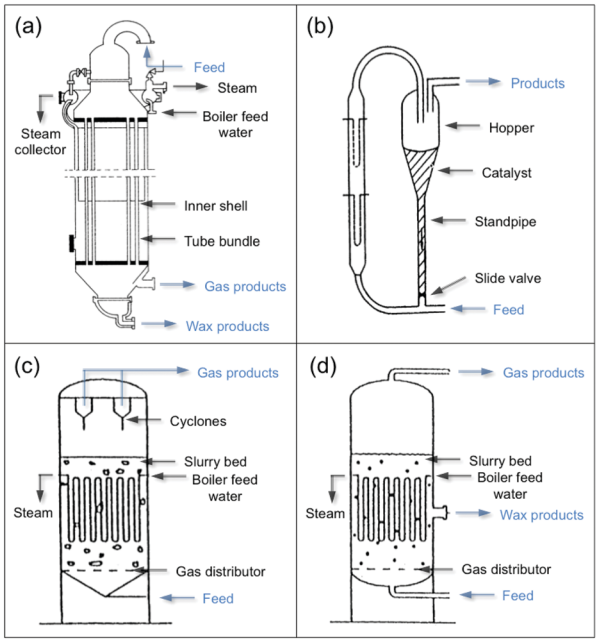

Fig. 14 Schematic representations of (a) a multi-tubular fixed bed reactor and (b–d) three types of fluidized bed reactors: (b) circulating fluidized bed, (c) ebullated or fixed fluidized bed, and (d) slurry phase bubbling bed. Types (b) and (c) are two-phase systems. In type (d), CO_2 and H_2 pass through a liquid in which the solid catalyst particles are suspended. Adapted with permission from ref. 216. Copyright 2002 Elsevier B.V.

decades, underlines their numerous advantages (1) toward the effective removal of the generated heat, (2) as a bridge to higher hydrocarbon productivity due to the effective contact between the reacting phases with higher heat and mass transfer rate, and (3) with a facile continuous operation mode compared to the other reactor types.[218,219] Over the years, fixed fluidized bed (FFB) reactors have also been preferable as compared to circulating fluidized bed (CFB) reactors. The former require notably smaller dimensions and subsequent lower construction costs up to 40%, offer a wider cooling section allowing the installation of more cooling coils, demand lower rates of removal and replacement with fresh catalyst, and require less maintenance as compared to CFB reactors, which require significant maintenance, particularly in the narrower sections where the very abrasive iron carbide is continuously circulated.[216]

In the design of t-CO_2RR reactors and selected process configuration, the authors highlighted additional points of key relevance: (1) it is crucial to remove water during the catalytic evaluation of iron-based catalysts in modified FT systems, for which membrane reactors, allowing continuous water removal during the reaction, have been proposed to dramatically hinder the observed catalytic decay and improve the performance of the overall process. (2) Emerging process configurations may find higher suitability in the direct RWGS and modified FT synthesis in consecutive reactor volumes under optimized conditions for each reaction. (3) CH_4, short-chain alkanes or alkenes, and longer-chain (C_{5+}) hydrocarbons are preferentially recycled in the process in accordance with the desired product selectivity, whereas CO and CO_2 are recycled to the RWGS unit (in the case of sequential process configuration).

2.6. Concluding remarks and analytical prospects

The chemical conversion of CO_2 into value-added fuels with the assistance of H_2 and utilizing inexpensive and stable catalysts is a promising response to the pernicious effects of CO_2 accumulation in the atmosphere and to the foreseen shortage of fossil fuels on a global scale. The catalytic t-CO_2RR has been known for several decades to directly produce hydrocarbons above methane in high conversion yields. While the production of long-chain hydrocarbons is economically preferable, to date, selectively reducing CO_2 to synthetic natural gas has shown superior promise, notwithstanding the lower value of CH_4, wider H_2 consumption, lower energy per unit volume, and eventual storage difficulties.

Ni and Co-based systems, and Fe-based catalytic systems have gained increasing attention due to their promising features regarding the CO_2RR to produce CH_4 and longer carbon-chains, respectively. The increasingly convergent application of Fe-based CO_2RR catalysts in parallel with the conventional high-temperature Fischer–Tropsch platforms utilizing syngas has further highlighted the urgent need for the assessment of novel materials. In addition, the induced reconstruction of Fe-species, which is largely affected by the choice of the selected operating conditions, support and structural promoters, has reflected the lack of well-defined catalysts in which the spatial arrangement of interfaces has been determined; the difficulty in the manipulation of the desired mechanistic pathways is well-known. The broad distribution of the products in the modified FT synthesis directly implies their costly separation and the need for large capacity plants. For these reasons, t-CO_2RR through the above-mentioned pathway may require further optimization in the rational design of these catalysts toward enhanced product selectivity.

Showcasing the extensive line of work regarding the t-CO_2RR in the past decades, most of the catalysts reviewed herein have exposed the increasingly complex synthesis, with metal catalysts being incorporated on optimized supports and their often further decoration with multiple structural promoters. Most of these catalysts that are synthesized by co-precipitation, impregnation, or physical mixing exhibit large morphological variations in the spatial arrangements of the active sites and subsequent characterization uncertainties. On the one hand, the range of reported preparation methodologies increase the number of catalytic descriptors such as the surface area, particle size, and metal dispersion, leading to clear disparities in the attained catalytic performances. On the other hand, the lack of well-defined catalysts in which the formed interfaces are precisely controlled hinders the development of more efficient catalysts. The in-depth understanding of the reaction mechanism and identification of intermediates further represent a severe limitation in the development of highly efficient catalysts toward the control of the selectivity of each pathway. Notwithstanding the consensus for the presence of CO* as a reaction intermediate,

the identification of other descriptors, *e.g.* oxygen adsorption energy, adsorption configurations of CO_2 and key intermediates and activation barriers for key reaction steps, deserves greater focus in the future. It should be additionally noted that CO_2 hydrogenation *via* a modified FT synthesis has been largely demonstrated to give rise to liquid fuels and short-chain olefins, depending on the catalyst and applied promoters, and selected operative conditions.

Along with the above listed practical drawbacks, one of the most defining industrial bottlenecks for the reutilization of CO_2 is the need to obtain both CO_2 and H_2 in an economically favorable manner. In particular, renewable and relatively inexpensive CO_2-free H_2 production is a requirement for sustainability, and it remains a limitation for the large-scale practical implementation of the t-CO_2RR. Although H_2 may be obtained from renewable CO_2-neutral energy sources (*e.g.* electrolysis, biomass, WGS, through the use of bacteria, or wind power), to date, 95% of the produced H_2 is derived from hydrocarbon-based feedstocks, *e.g.* steam reforming of CH_4, coal gasification and partial oxidation of light oil residues, leading to additional CO_2 production.[220–222] CO_2-free H_2 production on a large scale with significantly reduced associated costs plays a key role in the cost-competitive production of gasoline and light olefins. H_2 synthesis by alternative (photo)-electrocatalytic water splitting is highly regarded in this sense. Similarly, the above listed strategies for a CO_2-free H_2 production are predicted to follow new developments.

To offset the energetic demand of the reaction, proper energy integration is also required toward the commercialization of the progress outlined herein. Alternative strategies may additionally induce a decrease in the required thermoneutral voltage in the t-CO_2RR. Recently, well-dispersed Ru-NPs on exfoliated LDHs have been proposed as highly active heterogeneous catalysts for CO_2 methanation under light irradiation in a flow-type photoreactor.[223] This is an example of new design ideas for catalysts functionalized by targeting activation to reactants, opening a door to potential industrial solar-to-chemical energy conversion.[224]

3. Electrochemical CO_2 reduction reaction (e-CO_2RR)

Over the past decade, a marked decline in renewable electricity prices induced by the steep development of novel energy platforms has extended the possibilities for decreasing the dependence on fossil fuels globally. Herein, we highlight the photovoltaic industry on the basis of the consistent improvement of solar cell efficiencies and the reduction of manufacturing costs.[225] Compared with traditional chemical processes driven by fossil energy, electrochemical technologies are environmentally friendly, operate under relatively mild conditions, and can be coupled with renewable electricity sources at remote locations. Transforming CO_2 into hydrocarbons is a valuable alternative for leveling the output from these intermittent renewable sources (*e.g.*, wind and solar energy) that are strongly dependent on season and daylight, to serve previously established infrastructures on a global scale.[226]

In principle, CO_2 can be electrochemically reduced to give a wide range of products at the surface of solid electrodes. In a typical CO_2RR cell, water acts as the source of protons and CO_2 is reduced to the target products, *e.g.*, CO, formate, methanol, and methane at the cathode, while oxygen is evolved at the anode. A cost-effective e-CO_2RR requires electrocatalysts acting as working electrodes that can operate at low overpotentials and generate desirable products at high current densities over long periods of time (enhanced stability) without the formation of by-products (enhanced selectivity). In practical processes, however, the CO_2RR is undesirably skewed to more negative voltage ranges, with the emerging overpotentials being largely attributed to (1) high activation energies needed for the electron transfer during CO_2 activation on the surface of the catalyst, (2) ohmic losses related to the electrolyte and electrode conductivity, and (3) observed mass transport limitations. Similarly, high Faradaic efficiencies (FE), defined as the ratio of charges transferred to a certain product relative to the number of total charges passed through the circuit, are a key prerequisites in the synthesis of attractive electrocatalysts.

Electrocatalytically, methane was first reported with the co-formation of CO and CH_3OH at significantly low partial currents in the presence of Ru.[227] Only in 1985 did the pioneer works of Hori and Suzuki disclose the formation of CH_4 and C_2H_4 as the main products of e-CO_2RR on a Cu electrode.[228,229] Fast-forward to three decades from the seminal works of Hori, and Cu has remained the sole metal electrocatalyst capable of binding and converting the now well-established adsorbed CO (CO*) intermediate (*cf.* Section 3.1) to more reduced hydrocarbon products at fairly high efficiencies. To date, the synthesis of hydrocarbons requires the highest overpotentials and lowest FE (Fig. 15).[230] Hydrocarbon or alcohol formation should be thermodynamically more favorable than the production of CO, formic acid, formaldehyde or H_2.[231] Experimentally, slow kinetics are observed as multiple electron transfer (beyond $n = 2$) is required in both cases (*e.g.* for CH_4, $n = 8$).[232] In addition, with increasingly negative applied potentials the parasitic H_2 evolution reaction (HER) becomes more significant, by consuming protons and electrons required in the e-CO_2RR.

3.1. Mechanistic difficulties

The mechanism for the e-CO_2RR is an area of intense discord.[233] In the presence of heterogeneous electrocatalysts, the reaction takes place at the interface established with a usually CO_2-saturated aqueous electrolyte. The rate-limiting chemical adsorption of CO_2 is followed by electron transfer and/or proton migration to cleave C–O and form C–H bonds, configuration rearrangement of involved intermediates, and product desorption and diffusion into the electrolyte. In the multi-step e-CO_2RR to CH_4 involving an eight-electron transfer and seven reaction intermediates, in-depth mechanistic studies demand an understanding of the problem in a seven-dimensional space of adsorbate–surface interaction energies.[234] The seminal works from Hori first claimed the intermediate formation of

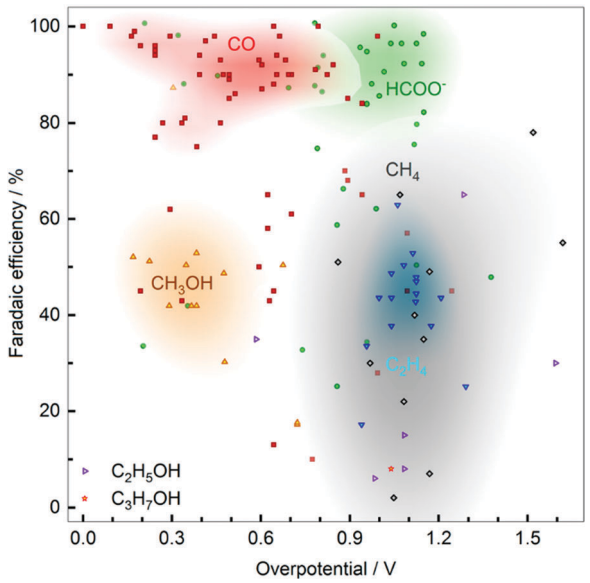

Fig. 15 Performance map for the e-CO_2RR toward commonly reported products in terms of the maximum attained FE and corresponding overpotential for each reported catalyst. A cluster analysis of the points (by kernel density estimation, KDE), demonstrated by the corresponding background color intensity, unequivocally revealed the performance regions associated with each product. Bibliographic references and relevant data for each report were provided by the authors. Adapted with permission from ref. 230. Copyright 2017 American Chemical Society.

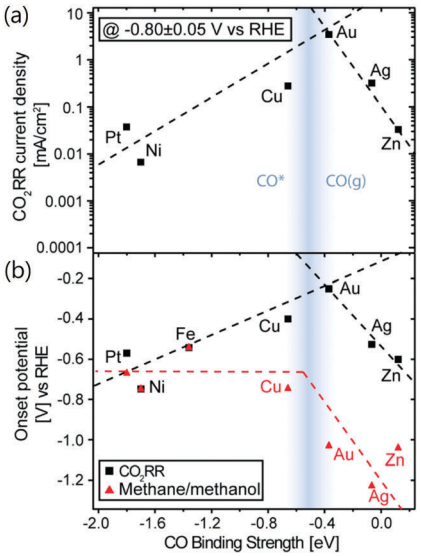

Fig. 16 (a) Volcano plot of partial current density for the e-CO_2RR assessed at −0.8 V *vs.* CO binding strength. (b) Distinct onset potentials plotted *vs.* CO binding energy for the overall e-CO_2RR, and for methane/methanol production. Dashed lines serve as a guide. Reprinted with permission from ref. 245. Copyright 2014 American Chemical Society.

CO,[235–237] with adsorbed CO (CO*) being later confirmed by chronopotentiometric evaluation.[238,239] To date, reducing CO and CO_2 has revealed similar product distribution and potential dependence, thereby reinforcing that the rate-determining step occurs after CO formation.[240,241] In light of the complexity of the proposed mechanisms, studies based on other identified representative intermediate species *e.g.*, HCOOH, HCHO, MeOH, and CH_3CHO, have become a noteworthy strategy.[242]

Throughout the years, comparative studies have ascribed the activity and selectivity of efficient CO_2RR electrocatalysts to the resulting binding energy of the involved intermediates with the selected catalyst.[234,243–245] Within the extensive line of examined materials, *e.g.* ionic liquids, proteins, organometallic complexes, metals, transition-metal oxides, transition metal chalcogenides, and carbon-based materials (N-doped nanostructures in the form of few-layered graphene, carbon nanotubes and carbon fibers), the large majority has been found to be capable of solely yielding CO (n = 2).[246–252] To date, the presence of metals is almost universally required for the e-CO_2RR to occur to a significant extent,[230] with, Al, Si, V, Cr, Mn, Co, Zr, Nb, Mo, Ru, Rh, Hf, Ta, W, Re, and Ir being mostly inactive at −2.2 V_{SCE} in 0.05 M $KHCO_3$.[253] Seminal works over metal electrodes (Hg, Au, Pb, Zn, Cd, Sn, and In) with no investigation of emerging gaseous products reported the nearly exclusive production of formate in solution.[254,255]

The singularity of Cu has been established to arise from an ideal binding energy to the formed intermediates allowing the subsequent reduction of CO_2 to CO and to further desired hydrocarbons (Fig. 16). With metals like Sn, Hg, Pb, In, Cd, and Tl, the formed $HCOO^-$, following the activation of CO_2 with the transfer of one electron and one proton, desorbs easily. With Au, Ag, and Zn, the presence of a strongly bound $HCOO^-$ permits the breaking of the C═O bond, but the resulting weakly adsorbed CO is promptly evolved as a reaction product.[244] In particular, Au features the highest current density and the lowest onset potential for e-CO_2RR. Metals of this group were shown to produce methanol (Au) or both methane and methanol (Ag and Zn) at more negative potentials,[245] which further pinpoints the importance of the oxophilicity of the surface in the selectivity between hydrocarbons and oxygenates, with Au being, in this case, the least oxophilic metal of the group. Metals that bind CO* strongly are poisoned by CO or other intermediates, with H_2 being evolved as the main product from the competing water reduction. With a high CO* coverage, the reduction of CO* is rate-determining and rather insensitive to the binding strength. For these reasons, metals such as Pt, Ti, Ni and Fe show similar onset potentials as compared to Cu for the limited CH_4 production.[245]

The complexity behind the proposed reaction mechanisms is largely ascribed to the dependence of the catalytic phase and operating conditions.[256] Mechanistic difficulties are further aggravated by oxygenate species sharing commonalities with the pathways toward hydrocarbon production, for which the oxophilicity of the surface plays a central role.[245] Over the Cu electrode, extending the chain-length could not be achieved merely based on the selected potential range (Fig. 17). The observed product distributions evidenced an increase in the FE to C_2H_4 and ethanol up to a certain potential range, with the latter seemingly decreasing at more negative potentials. Interestingly, methane and ethylene unveiled different onset

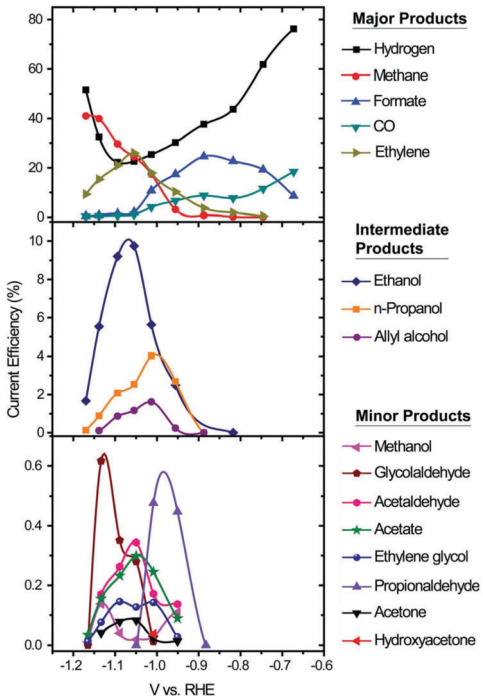

Fig. 17 Plots of the current efficiency of emerging e-CO_2RR products over the Cu electrode as a function of potential. Products were divided into three panels in which major, intermediate, and minor products have been grouped. The data reported by Jaramillo reflected previous reports on the Cu electrode being extended to a wider overpotential range and therefore shedding light on the current efficiency of several new products detected in this contribution for the first time. Reprinted with permission from ref. 232. Copyright The Royal Society of Chemistry 2012.

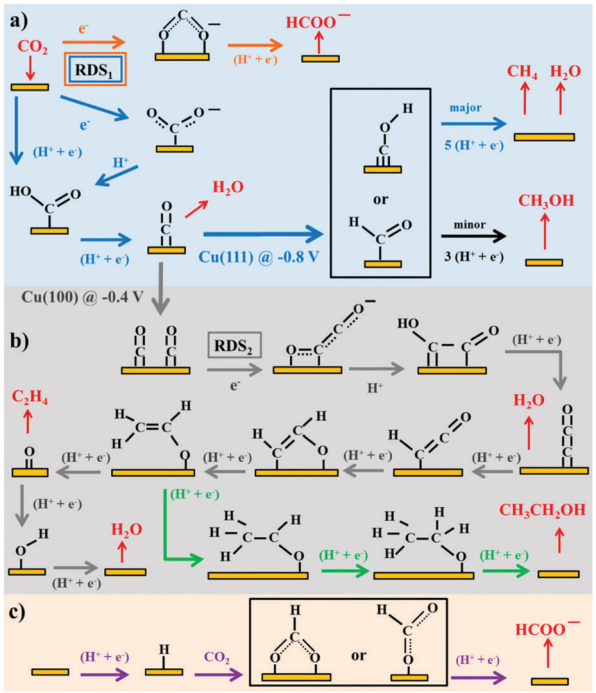

Fig. 18 Possible reaction pathways for the e-CO_2RR leading to the synthesis of hydrocarbons (CH_4 and C_2H_4) along with CO, formate (orange and purple arrows), and oxygenates (black and green arrows). (a) and (b) are mechanistic pathways toward C_1 and C_2 species, respectively, while (c) represents the pathway for CO_2 insertion into a metal–H bond yielding formate. Species in black are adsorbates and species in red are reactants or products in solution. RDS are rate-determining steps, accounting for the activation of CO_2 and the dimerization reaction between CO* adsorbed species. Potentials (V_{RHE}) for Cu(111) and Cu(100) are in accordance with experimental observations. Reprinted with permission from ref. 256. Copyright 2015 American Chemical Society.

potentials, largely suggesting that the formation of C_2H_4 could surprisingly be attained in less negative ranges as compared to CH_4. For CH_4 and C_2H_4, product selectivity has been ascribed to distinct rate determining steps and coverage effects.[232,241] In Fig. 18, the overall mechanistic complexity of these products is depicted as intentionally featuring proposed pathways in the synthesis of oxygenates, CO, and formate. Over the Cu cathode, following the rate-determining CO_2 activation step and the formation of the generally accepted CO* intermediate, distinct facet-dependent C_1 and C_2-based mechanisms have been reported (*cf.* Section 3.2.1);[257] on Cu(111) the reduction of CO* to CH_4 and C_2H_4 takes place simultaneously, whereas on Cu(100) a second pathway directs C_2H_4 at lower potentials without CH_4 generation.[258] These findings were corroborated by DFT calculations demonstrating that dimerization should have a lower activation barrier on Cu(100) than Cu(111), and that the divergent mechanistic pathways are in fact the reason for the distinct onset potentials found for CH_4 and C_2H_4 in Fig. 17.[259] On Cu(111), adsorbed CO species have been proposed to have subsequent proton-electron incorporation to give CHO*, H_2CO* and OCH_3*.[260] With each electrochemical step involving the transfer of a proton from the solution to a species adsorbed on the surface, the CH_4 partial current has been shown to be proportional to proton activity.[261] At very low and high pH, CH_4 formation is mirrored by the HER.[262] Herein, Fig. 18 additionally pinpoints the controversy found in the literature reflecting the proposed mechanistic pathways involving either the generation of CHO* or COH* species (Fig. 19).[263–265]

On Cu(100), the proposed mechanisms suggest OCCO* formation by CO* dimerization under relatively low overpotential, which represents a more favorable pathway compared to the rate-determining proton-transfer-dependent CO* hydrogenation. C_2H_4 is preferentially formed in basic electrolytes, while in acidic or neutral solutions CH_4 formation is preferred.[262] The rate of CO* dimerization toward the selective formation of C_2H_4 has been further suggested to benefit from high CO* surface coverage and tensile strain.[266,267] For the formation of C_2H_4 on Cu(100), the formed dimer can be consecutively hydrogenated to OCCHO*, OHCCHO*, and OH_2CCH_2OH*. The OH_2CCH_2OH* intermediate can form HOH_2CCH_2OH* by direct hydrogenation and H_2CCH_2OH* by breaking the C–O bond, which might be a parallel pathway in the reduction mechanism of the CO dimer on Cu(100). C_2H_4 is finally formed by dehydroxylation of the HOH_2CCH_2OH* and H_2CCH_2OH* intermediates.

3.2. The singularity of Cu: modification of metal electrodes

Since the initial claims by Hori, the extensive literature on the aqueous e-CO_2RR to hydrocarbons on Cu has conspicuously

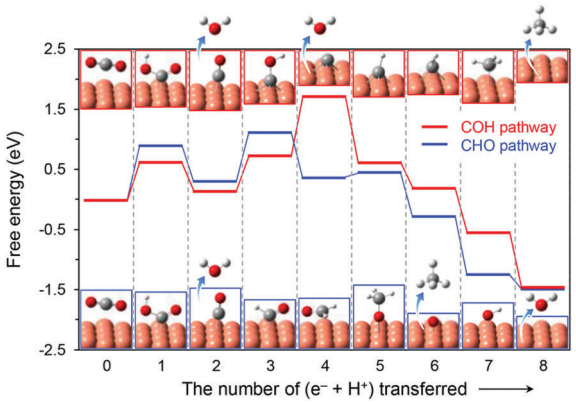

Fig. 19 Multi-step conversion of CO_2 to CH_4, indicating the calculated free energies (at zero external bias) for alternative pathways considering the formation of CHO* (blue) and COH* (red) intermediates.[264,265] Molecular species at each step are identified. Reprinted with permission from ref. 263. Copyright 2017 American Chemical Society.

unveiled Faradaic yields above 50% at reasonable current densities (*ca.* -5 mA cm^{-2}). These hydrocarbons are produced at prohibitively high overpotentials (nearly 1 V), reflecting high efficiency losses on the Cu electrode. Fast catalytic deactivation and low product selectivity accompanied by the formation of oxygenates have reflected additional bottlenecks for practical use. The extensive research to enhance the catalyst performance of Cu and its derivatives, *e.g.* studies on the morphology and surface oxidation state, is reviewed below and conveniently summarized in Table 2. Works on Cu overlayers over a substrate metal of choice are suggested for revision[268–270] and not detailed herein.

3.2.1. Morphology studies. As discussed above, Cu electrodes have been shown to exhibit facet-dependent selectivity for both CO and CO_2RR.[232,257,271–273] Cu(111) favors CH_4 and C_2H_4 at high overpotentials (<-0.8 V_{RHE}), whereas on Cu(100), C_2H_4 is formed through a C–C coupling pathway, followed by a series of reduction steps of the C_2 intermediates under a relatively lower overpotential range (-0.4 to -0.6 V_{RHE}).[257] Cu(100) additionally suppresses H_2, CO and formate at less negative potentials as compared with Cu(111), rendering higher hydrocarbon yields.[271] Similarly, stepped surfaces such as Cu(911) and Cu(711) showed remarkable selectivities to $\geq C_2$ species.[273] On polycrystalline Cu surfaces exhibiting a wide heterogeneity of catalytic sites, the FE for C_2H_4 and CH_4 is significantly lower (*ca.* 30 and 29% in 0.1 M $KHCO_3$, respectively).[238]

Finding a surface that favors C–C coupling pathways toward C_2H_4 formation not only underlines the economic interest of ethylene over methane, but it is also of importance to unlock the pathways to desired multicarbon products. Works focusing on the nano-structuralization of Cu have disclosed enhanced performance on single crystal Cu(100) surfaces and even more on cleaved Cu(100) substrates with high-indexed planes.[271] Cu nanocubes easily synthesized *in situ* and predominantly exposing (100) facets were claimed to be among the most selective for C_2H_4 over CH_4.[274] Onset potentials for C_2H_4 production in 0.1 M $KHCO_3$ over these Cu nanocubes, Cu(100), Cu(Poly), Cu(211) and Cu(111) decreased in the order $-0.60 > -0.73 > -0.74 > -0.79 > -0.96$ V_{RHE}, respectively. Analogous results suggested a key role played by the edge sites of these nanocubes.[275,276] When coupled with density functional theory (DFT) calculations, the approach has further shed light on the determination of the energetics of the initial C–C coupling steps on varying Cu facets.[277]

These findings have stimulated the rational design of creative Cu-based nanostructures as a strategic path to enhance the catalytic activity and attain desired product selectivity.[278] CO_2RR on Cu NPs was shown to depend on the particle size, the population of low-coordinated surface sites, and the chemisorption strength of intermediate and hydrocarbon species.[279,280] In agreement, several studies have been reported on the abundance of weakly coordinated surface sites on Cu, *e.g.* sputtering,[281] electropolishing,[281] electrodeposition,[282] and anodization.[282] Baturina claimed that over Cu NPs supported on carbon (carbon black, single-wall carbon nanotubes, and Ketjen Black) the ratio of C_2H_4 to CH_4 could be enhanced by decreasing particle sizes, which was also ascribed to an increase in the fraction of under-coordinated sites, *e.g.* corners, edges, and defects.[283] Monodisperse Cu NPs assembled on a pyridinic-N rich graphene (p-NG) support showed mass- and particle size-dependent catalysis for the selective e-CO_2RR to C_2H_4 through C–C coupling over CH_4, with corresponding FE of 19 and 0.9% at -0.9 V_{RHE}, respectively.[284] Despite a still important formate formation (FE of 3.6%), the localized electron pair of the pyridinic-N with stronger Lewis basicity was claimed to facilitate the rate-determining formation of the $CO_2^{\bullet-}$ anion radical, and its protonation to COOH*.

Corroborated by reaction-diffusion modeling, additional reports on Cu NPs revealed that mesoscale phenomena such as interparticle reactant diffusion and readsorption of intermediates could be expected to play a defining role in product selectivity.[285] Agglomerates of *ca.* 15 nm sized Cu nanocrystals showed the promising formation of propanol at current densities *ca.* 25-fold larger than those found on Cu^0 NPs at the same applied potential.[286] Alternatively, ensembles of densely packed Cu NPs were shown to undergo structural transformations during electrolysis into electrocatalytically active cube-like particles inter-mixed with smaller nanoparticles (Fig. 20).[287] Enhanced C_2H_4 formation along with ethanol and *n*-propanol was found at an onset potential at -0.53 V_{RHE}, with a FE to C_2–C_3 species of *ca.* 50% at -0.75 V_{RHE}. Although the observed *in situ* structural evolution of Cu-based electrocatalysts is thoroughly discussed in the following subsections, a greater understanding of how NPs and the atoms within evolve under electrically biased and chemically relevant conditions is necessary. Nonetheless, using NPs as precursors to an active architecture is presumed to serve as a valuable pathway to extend the catalyst library in future exploratory works.

Over Cu nanowire array electrodes, the hydrocarbon selectivity at a fixed potential could be tuned by systematically altering the Cu nanowire length and density.[288] Recently, 5-fold twinned $\sim$20 nm-thin Cu nanowires were found to exhibit high CH_4 selectivity over other carbon products, reaching 55%

Table 2 Faradaic efficiencies (%) of products obtained from the e-CO_2RR on representative copper-based catalysts reported in the literature. The selected potentials reflect the maximization of the corresponding C_2H_4 to CH_4 ratios. N.D. refers to (stated or presumed) non-detected species. Catalysts are organized in accordance with the underlying synthesis strategy in the corresponding papers for an effective comparison with reference Cu electrodes (a). (b) Single crystal electrodes, (c) nanostructures (NP and NW stand for nanoparticles, and nanowires respectively), (d) enhanced surface roughness, (e) Cu_2O or oxide-derived electrodes, (f) surface modification studies (*e.g.* chlorine-induced), and (g) Cu-based alloys. Catalysts reflecting the most promising results in the current state-of-the-art have been conveniently italicized

	Catalyst	Electrolyte	pH	Potential (V_{RHE})	Faradaic efficiency (%) C_2H_4	CH_4	Others	Ref.
a	Cu foil	0.1 M $KHCO_3$	6.8	−1.1	20	57	CO (5), H_2 (20)	279
	Polycrystalline Cu	0.1 M $KHCO_3$	6.8	−1.01	30.1	29.4	C_{2+} (3.0) CO (2)	238
	Cu foil	0.1 M KCl	5.9	−1.05	47.8	11.5	C_3H_7OH (3.6), C_2H_5OH (21.9) CO (2.5), H_2 (5.9)	237
b	Cu(111)	0.1 M $KHCO_3$	6.8	−1.15	8.3	46.3	C_2H_5OH (2.6) HCOOH (11.5), CO (6.4), H_2 (16.3)	271
	Cu(100)	0.1 M $KHCO_3$	6.8	−1.00	40.4	30.4	C_3H_7OH (1.5), C_2H_5OH (9.7) HCOOH (3.0), CO (0.9), H_2 (6.8)	271
c	5-fold twinned Cu NW	0.1 M $KHCO_3$	6.8	−1.25	2	55	C_2H_5OH (3) $HCOO^-$ (3), CO (1)	289
	Cu NP (2 to 15 nm)	0.1 M $KHCO_3$	6.8	−1.1	3	12	CO (22), H_2 (65)	279
	Cu nanoflower	0.1 M $KHCO_3$	6.8	−1.6	10	5	HCOOH (50)	278
	8.1 μm-length Cu NW arrays	0.1 M $KHCO_3$	6.8	−1.1	17.4	N.D.	C_3H_7OH (7.8) C_2H_5OH (3.8), C_2H_6 (2.4) HCOOH (17.5), CO (7.6), H_2 (44.2)	288
	Cu/p-NG	0.5 M $KHCO_3$	7.3	−0.9	19	0.9	C_2H_6 (0.6) $HCOO^-$ (3.8)	284
	Cu NP ensembles	0.1 M $KHCO_3$	6.8	−0.81	27	0.4	C_3H_7OH (5.9), C_2H_5OH (13.3), C_2H_6 (0.3) $HCOO^-$ (8.5), CO (6.6), H_2 (35.7)	287
	Prism-shaped Cu nanocatalyst	0.1 M $KHCO_3$	6.8	−1.1	27.8	14	C_3H_7OH (4), C_2H_5OH (3) HCOOH (14), CO (1), H_2 (33)	291
	Cu nanocubes (44 nm)	0.1 M $KHCO_3$	6.8	−1.1	41	20.2	C_2H_6 (0.3) $HCOO^-$ (4), H_2 (60)	275
	40 wt% Cu/VC	0.1 M $KHCO_3$	6.8	−1.39	42	17	H_2 (17)	283
d	Cu foam	0.5 M $NaHCO_3$	7.2	−0.7	14	N.D.	C_2H_6 (37) CO (23), H_2 (12)	292
	Cu mesocrystals	0.1 M $KHCO_3$	6.8	−0.99	27.2	1.47	C_2H_6 (0.3) $HCOO^-$ (4), H_2 (60)	276
	Cu NP-covered surface	0.1 M $KClO_4$	6 ± 0.5	−1.1	36	1	C_2H_6 (1) CO (34), H_2 (28)	281
e	$PdCl_2$/Cu_2O-derived Cu	0.1 M $KHCO_3$	6.8	−1.0	3.4	N.D.	C_3H_7OH (5), C_2H_5OH (11), C_2H_6 (30.1) H_2 (16)	342
	8.8 μm Cu_2O film	0.1 M $KHCO_3$	6.8	−0.99	21.6	0.2	C_2H_5OH (5.1), C_2H_6 (0.2) CO (0.5), H_2 (67.7)	308
	Cu_2O-Derived Cu	0.5 M $KHCO_3$	7.5	−1.25	22	2.5	CO (4)	307
	Cu_2O-Derived Cu	0.1 M $KHCO_3$	6.8	−0.98	32	N.D.	C_3H_7OH (5), C_2H_5OH (8) H_2 (34)	316
	Cu_2O-Derived Cu	0.1 M $KHCO_3$	6.8	−1.0	32.1	N.D.	C_3H_7OH (4), C_2H_5OH (16.4) H_2 (34)	342
	Cu_2O-Derived Cu	0.1 M $KHCO_3$	6.8	−0.98	32.4	<2	C_3H_7OH (5), C_2H_5OH (8) $HCOO^-$ (3), H_2 (35)	266
	Anodized Cu[a]	0.1 M $KHCO_3$	6.8	−1.08	38.1	1.3	H_2 (36.6)	343
	Electro-redeposited Cu	*0.1 M $KHCO_3$*	*6.8*	*−1.2*	*39.04*	*0.03*	*C_2H_5OH (7.8) $HCOO^-$ (16.30), CO (1.16), H_2 (31.56)*	*320*
	Plasma-activated Cu nanocube	0.1 M $KHCO_3$	6.8	−1.0	45	N.D.	C_3H_7OH (9), C_2H_5OH (22) CO (2)	323
	Boron-doped Cu[a]	*0.1 M $KHCO_3$*	*6.8*	*−1.1*	*52*	*0.08*	*C_2H_5OH (27), H_2 (20)*	*321*
	Nano dendritic Cu catalysts	*0.1 M KBr/Br_2*	*2.5*	*−1.30*	*57*	*9*	*CO (8), H_2 (9)*	*322*
	Plasma-activated Cu[b]	*0.1 M $KHCO_3$*	*6.8*	*−0.9*	*60*	*2*	*$HCOO^-$ (2), CO (2)*	*309*
f	Chloride-induced Cu_2O–Cu	0.1 M KCl	N.A.	−1.6	22	1.4	C_4H_{10} (0.9) C_3H_6 (0.9), C_3H_8 (1), C_3H_7OH (8.7) C_2H_5OH (24), C_2H_6 (1), CH_3OH (3) $HCOO^-$ (3)	325
	Cu foil	0.1 M $KHCO_3$ + 0.3 M KI	6.8	−1.0	58	22	$HCOO^-$ (6), CO (<1), H_2 (12)	326
g	Au_3Cu alloy nanocrystals	0.1 M KH_2PO_4/ K_2HPO_4	7.0	−0.98	7	36	$HCOO^-$ (9), CO (27), H_2 (21)	335

[a] Cu-Based electrodes exhibited remarkable stability levels up to 40 h. [b] For the plasma-activated Cu, values refer to collected Faradaic selectivities instead of Faradaic efficiencies.

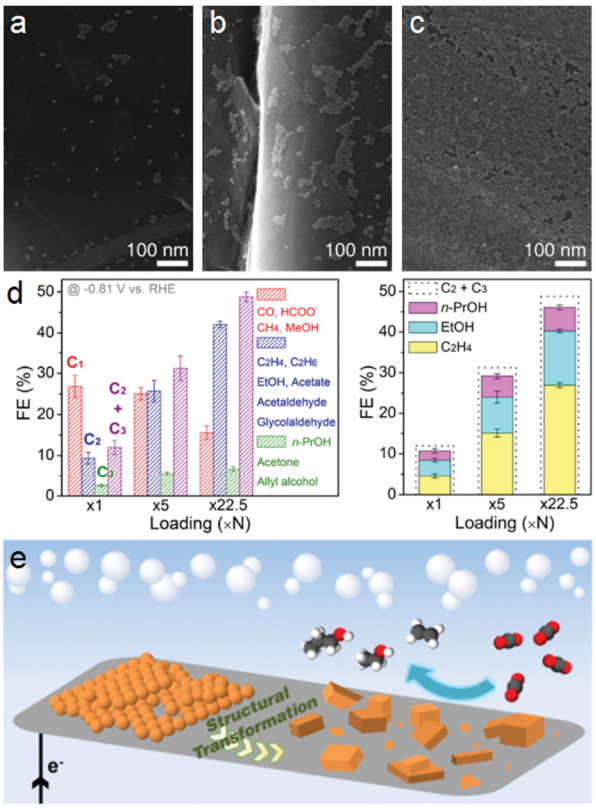

Fig. 20 Representative SEM images of Cu NPs loaded on carbon-paper support at corresponding (a) ×1 loading, (b) ×5 loading, and (c) ×22.5 loadings. (d) FE for C_1, C_2, and C_3 products, and detailed values for ethylene, ethanol, and *n*-propanol depending on the loading of Cu NPs in each sample. These measurements were carried out at −0.81 V_{RHE}, using CO_2-saturated 0.1 M $KHCO_3$. (e) Schematic representation of the proposed transformation process of Cu NP-ensembles into an active catalyst for C_2–C_3 formation.[287]

FE at −1.25 V_{RHE}.[289] Additional wrapping with graphene oxide (GO) preserved both the morphology and reaction selectivity of these nanostructures. These findings further agree with the enhanced stability and facile electron transfer reported elsewhere between rGO and Cu NPs, believed to increase localized electron concentrations.[290]

Recently, highly defective prism-shaped Cu catalysts prepared using a one-step electrodeposition method showed FE to C_2H_4 up to 27.8% for 12 h.[291] The improved activity for C_2H_4 production was reflected in a 4-fold higher partial current density (−11.8 mA cm^{-2}), as compared to that of the planar Cu sample (−2.8 mA cm^{-2}). The presence of a significant fraction of defect sites on the prism Cu surface plays a role in improving C_2H_4 production. The report is an example of assessing the impact of surface roughness as a strategic pathway to enhance the number of active sites reflected in recent years. For instance, Broekmann designed mesoporous Cu foams with FE to C_2 reaching 55%, by a template-assisted electrodeposition process occurring during selected HER-conditions.[292] Highest efficiencies were reached for C_2H_6 at −0.7 V_{RHE} (37%) and C_2H_4 at −0.8 V_{RHE} (20%). The synthesis of Cu foams emphasized the importance of high surface roughness, hierarchical porosity, and the confinement of reactive species toward an increase of the hydrocarbon chain length, but it remains a challenge to assess the exact role of morphology taking into account the high variability in size, tortuosity, and crystal structure of the nanofabricated electrodes explored to date.[292,293] In addition and as detailed in the following sections, the morphology can further affect both local pH and flow field, accelerating the C–C coupling reaction and prolonging retention times.[294]

It is of current general consensus that surface reconstruction during e-CO_2RR is a key factor in the activity and selectivity of Cu electrodes, despite attempts to optimize the rational design of these catalysts. With a weak cohesive energy, simple polycrystalline Cu held at a fixed negative potential (−0.9 V_{SHE}) in 0.1 M KOH can undergo stepwise surface reconstruction, first to Cu(111), and then to Cu(100), highlighting the dynamic nature of the electrocatalytic surfaces.[295] In addition to physical conditions including temperature, pressure, and electrical potential, reversible surface reconstruction induced by adsorbates and reactants have been proposed. Reflecting the difficulty in witnessing the said phenomenon by *ex situ* methods, Waegele has presented, for the first time, clear evidence of the reversible reconstruction of Cu surfaces induced by the CO* intermediate.[296] Using attenuated total internal reflection infrared and surface-enhanced Raman spectroscopies, the reversible formation of nanoscale metal clusters on the electrode was revealed by the appearance of a new C≡O absorption band characteristic of CO bound to undercoordinated copper atoms and by the strong enhancement of the surface-enhanced Raman effect.

3.2.2. Surface modification and importance of the oxidation state. The incorporation of reducible organic additives, *e.g.* ionic liquids and pyridines with the potential to precipitate and form a film of corresponding bimolecular reductive coupling products has been recently demonstrated in the optimization of the selectivity between hydrocarbons and H_2.[297] The approach reflects the advantage of directly employing less expensive polycrystalline Cu metal electrodes. In the works of Agapie, the introduction of *N*-substituted pyridinium species was able to reduce CO_2 to $\geq C_2$ species with FE up to 78% (C_2H_4 of *ca.* 40%) and to attain unprecedented C_2 to CH_4 ratios.

Excellent results have been reported in the application of metal oxides with tunable layer thickness in the CO_2RR.[298] Copper oxides, in particular, have been the object of numerous studies since the seminal work of Frese.[282,299,300] In principle, however, CH_4 is thermodynamically more favorable on a pure Cu surface, whereas CH_3OH is preferred on Cu_2O or partially oxidized Cu electrodes due to the reverse free-energy distribution.[299] In fact, by introducing a moderate amount of oxygen (either oxidized surface or hydroxyl species), the reduction product has been shown to switch from CH_4 to CH_3OH over Cu-based electrodes.[301] It was in this sense unexpected when in recent years highly nanostructured surface electrocatalysts derived from the reduction of copper oxides showed unprecedented energy efficiency toward $\geq C_2$ species. Whether the oxide layer plays a role in the mechanism behind the reactivity trends,

or whether it only acts as a promoter of the resulting metal-based architectures has remained under intense discussion.[302,303] Importantly, these findings are notably derived from the stability of the formed Cu oxide surfaces.[304] Kanan suggested that Cu_2O layers formed by annealing and subsequent reduction to Cu particles during e-CO_2RR were able to efficiently catalyze the CO_2 reduction process at comparatively lower overpotentials.[305] The team reported the notable suppression of CH_4 in favor of C_2H_4, largely corroborated by distinct reports on C_2H_4 to CH_4 ratios up to *ca.* 100 over electrodeposited Cu_2O.[306–308]

In line with the discussion in the previous section, the impact of the resulting density of steps and edges of these oxide-derived nanostructures is anticipated.[308] Highly roughened surfaces with low-coordinated sites have been proposed to bind oxygen more strongly, helping to stabilize oxides during the reaction, with the highly porous architecture serving as a favorable oxygen reservoir.[309] In addition, it is expected that during the catalytic reaction on these rough surfaces, there is a significant rise in the local pH, suppressing the pH-dependent CO* protonation that leads to methane formation. The pH-independent pathway *via* CO dimerization is, however, not affected, resulting in high ethylene selectivities (*cf.* Section 3.1).[309] Similarly, reported disparate proton coupling requirements for CO and H_2 production have established a mechanistic basis for the CO_2RR selectivity toward CO.[310] The effect of the electrolyte concentration and the importance of the local pH are, in fact, believed to be a strategy of interest in upcoming research works (*cf.* Section 3.5).[311]

With e-CO_2RR being sensitive to electrolyte polarization, which causes gradients in pH and the CO_2 concentration near the cathode surface and therefore impacts the intrinsic kinetics of the reduction reaction, it is therefore desirable to measure the concentration of reaction-relevant species in the immediate vicinity of the cathode. Whereas conventional analytical methods only sample products from the bulk electrolyte, Bell and colleagues proposed the use of differential electrochemical mass spectrometry (DEMS) to measure the composition, *i.e.* CO_2 and reaction products of the local reaction environment.[312] This capability could be achieved by strategically coating the electrocatalyst directly onto the pervaporation membrane used to transfer volatile species into the mass spectrometer, enabling in this sense species to be directly sampled from the electrode–electrolyte interface during both e-CO_2RR assessments over Ag and Cu.

However, as pointed out by Cuenya and colleagues, observed lower onset potentials for C_2H_4 production could not be solely attributed to a local pH effect.[309] Grain boundaries in oxide-derived Cu have been suggested to support unique surface sites, which could show enhanced activity for e-CO_2RR. In line with their results in the electroreduction of CO, Kanan believed that engineering the grain boundaries by altering the oxide reduction method or by using an alternative preparation of nanocrystalline materials could yield catalysts with higher activity and selectivity for long-chain products.[313,314] Aggregates of smaller particles were believed to give rise to a higher surface population of catalytically active sites situated on grain boundaries, defects and particle–particle junctions. These findings agreed with the presence of strongly chemisorbed CO* on sites supported by grain boundaries, uncovered by Verdaguer-Cassadevall.[314] Linear correlations found between the surface area-normalized activity for CO_2RR to CO and the grain boundaries density on Au electrodes significantly add to the hypothesis.[315] With analogous concluding remarks, Yeo claimed that with oxide-derived Cu NPs, the crystallite size decreased from 41 to 18 nm, and the FE of C_2H_4 formation could be enhanced from 10 to 43%.[316]

The nature of the remaining $Cu^{\delta+}$ active catalytic sites has been thought to play a key role in the resulting catalytic performance, as recently demonstrated over oxidized Cu electrocatalysts prepared through facile and tunable plasma treatments.[309] The presence of these $Cu^{\delta+}$ species, rather stable under reaction conditions, was demonstrated through *operando* X-ray absorption spectroscopy and cross-sectional scanning transmission electron microscopy. The exemplary claims by Cuenya and colleagues, not only emphasized the importance of characterization to unlock unanswered mechanistic details but also attained an outstanding Faradaic selectivity (defined as the ratio between the target product amount and the total detected products amount) to C_2H_4, up to 60%. The result linked in analogous reports to the presence of subsurface oxygen species has received increasing attention in recent literature.[317,318] With the help of DFT calculations, Pettersson demonstrated that the presence of subsurface oxygen species could enhance the adsorption energy of CO on Cu(100), with effects extending to at least the third layer.[319] With an improved coverage of adsorbed CO on the Cu catalyst, the greater probability of CO dimerization, which is a rate-determining step toward the production of ethylene, is to be expected.

Notwithstanding the clear difficulty in disentangling the contributions of specific crystallographic facets, surface roughness, nano-structuralization, local pH, and the presence of $Cu^{\delta+}$ and subsurface oxygen species, efforts have permitted the establishment of important guidelines in upcoming research works. *In situ* time-resolved tracking of the Cu oxidation state under e-CO_2RR conditions through soft X-ray absorption (sXAS) spectroscopy analysis shared by Sargent's team earlier this year showed the presence of remaining $Cu^{\delta+}$ species even at highly negative potentials below -1.0 V_{RHE} (Fig. 21a).[320] These findings were ascribed to the fact that the selected sol–gel copper oxychloride ($Cu_2(OH)_3Cl$) precursor was able to slow the electrochemical reduction of the resulting electro-redeposited Cu-based catalyst, further enabling control over its nanoscale morphology. The authors reported a rapid transition from Cu^{2+} to Cu^+ (within 5 min), with the transition from Cu^+ to Cu^0 being much slower. Surprisingly, for over an hour under e-CO_2RR conditions, 23% of the catalyst was shown to exist as Cu^+ under an applied bias as low as -1.2 V_{RHE}. Under these conditions, a FE of 54% for C_{2+} products (ethylene, acetate, ethanol) was attained. The work shed light on the morphology evolution of these catalysts, suggesting a simultaneous dissolution and redeposition of copper ions from the sol–gel copper oxychloride precursor, and enabling a wide spectrum of emerging architectures of varying sharpness to be grown from within the pristine bulk material (Fig. 21b).

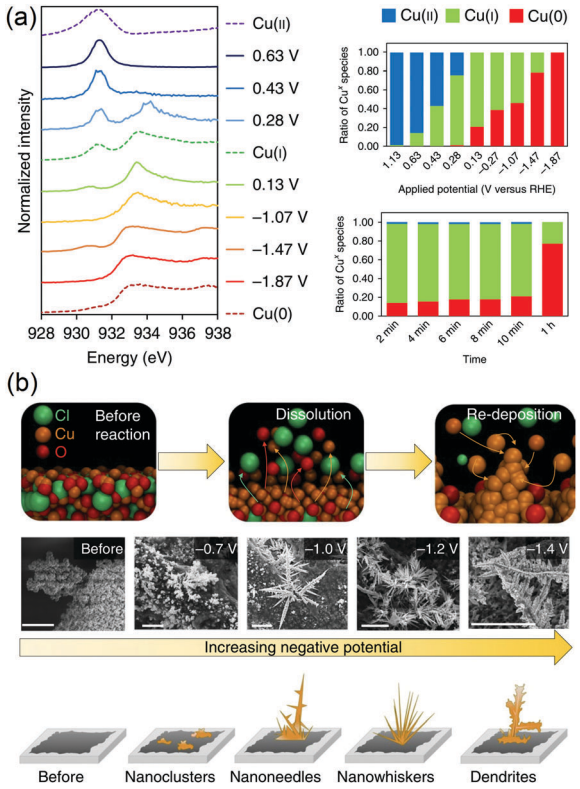

Fig. 21 (a) *In situ* Cu L_3-edge X-ray spectra of electro-redeposited Cu at different applied potentials and references for Cu metal, Cu_2O, and CuO. On the right side, calculated ratios of Cu oxidation states from linear combination fitting as a function of the applied potential or time. (b) Schematic representation of the growth of these nanostructures following simultaneous dissolution and redeposition of Cu. Representative SEM images (scale bars = 5 μm) collected at specific applied potentials after at least one hour of reaction. At −1.0 V_{RHE}, sharp needles of 5 to 10 μm in length could be witnessed, whereas at −1.2 V_{RHE}, sharp nanowhiskers of 5 to 10 μm with high length-to-diameter ratios predominated. At the most negative applied potential (−1.4 V_{RHE}), dendrites with rounded tips were reported. Adapted with permission from ref. 320. Copyright 2018 Springer Nature.

In light of the above findings, highly selective C_2 products from e-CO_2RR could be obtained on B-doped Cu with stable electron localization.[321] The attained selectivity of e-CO_2RR to C_2 hydrocarbons could be similarly ascribed, theoretically and experimentally, to the oxidation state of copper. In detail, at an average copper valence state of +0.35, the FE for C_2 hydrocarbons and C_2H_4 attained *ca.* 80% and 52%, respectively. Under these conditions, C_1 products (CH_4, CO, and HCOOH) could be additionally completely suppressed in both gas and liquid products.

Induced surface modification: additional studies. In a rather similar fashion to the works of Broekmann, Cu nanodendrites, obtained during the *in situ* electrodeposition in acidic medium (pH = 2.5) under high overpotential (<-2 $V_{Ag/AgCl}$) following local sintering and oxidation processes, showed an impressive FE to C_2H_4 of 57% at a current density of 170 mA cm^{-2}.[322] Contrary to the above-cited works, here the corrosive conditions under which catalysis was performed (using KBr, or mixtures of KBr and Br_2) were found to be responsible for the emergence of CuBr and Cu_2O-based needle-like dendrites. Of equal significance is the synthesis of highly active and selective Cu nanocubes with tunable Cu(100) facets as discussed above, but incorporating oxygen/chlorine ion content by low-pressure plasma pretreatments.[323] In this case, these electrodes displayed lower overpotentials and higher ethylene, ethanol, and *n*-propanol selectivity, resulting in a maximum FE of *ca.* 73% for C_2 and C_3 products.

Initial works by Hori evidencing changes in the product selectivity by changing the cationic species (Li^+, Na^+, K^+, and Cs^+) in bicarbonate solutions have recently inspired further works toward the surface modification of Cu-electrodes.[324] It was argued that the larger cations (*e.g.* Cs^+) had a greater specific adsorption, which caused a higher local pH, inhibiting CH_4 formation. Recently C_2 and $\geq C_3$ species were promoted over *in situ* generated Cl-induced bi-phasic Cu_2O–Cu using potassium chloride (KCl) electrolyte.[325] FE of $\geq C_3$ species attained values up to 11.5% at −1.6 V_{RHE}. Because of the chemoaffinity between chloride (Cl^-) and Cu, a uniquely shaped phase was observed during the application of a cathodic potential. An abundance of Cu^+ that could strongly bind and preserve the reaction intermediates for a longer time on the surface was demonstrated to be a key factor for the efficient synthesis of longer carbon chains. Similarly, Strasser showed that aside from an induced morphological evolution, the interaction of Cl^-, Br^- and, in particular, I^- with the Cu surface could lead to surface changes on the Cu interface as supported by DFT studies.[326]

3.2.3. Concluding remarks. In an attempt to establish a comparison of the important results achieved with Cu-based electrodes, Fig. 22 effectively summarizes the leading approaches discussed herein toward the enhanced synthesis of C_2H_4 as a representative target for longer-chain hydrocarbons. In a field still defined by a lack of standard metrics, the ratio of C_2H_4 to CH_4 is currently a figure of merit for rapidly evaluating the efficiency of novel catalysts in current research goals. A proper quantification is, however, particularly susceptible to the inaccuracy of measurements in the determination of decreasing contents of CH_4, therefore being prone to misleading conclusions. Fig. 22 underlines the successfulness of conveniently highlighted oxide-derived electrodes in suppressing CH_4 formation, and therefore, the promising character of this approach.

3.3. Alternatives to Cu electrocatalysts

3.3.1. Alloying. To date, the number of reports highlighting alternatives to Cu-electrodes for hydrocarbon production remains scarce. Effective electrocatalysts with tuned composition and chemical state are expected to mitigate the proton-catalyst interaction to suppress the competitive HER, while simultaneously optimizing the binding energy of intermediates, toward an enhanced energy efficiency, product selectivity, and improved reaction rates.[234,327] Studies on alloys and intermetallics with precise control of active sites have asserted the key role of composition and the need for new synthesis techniques.[327–329]

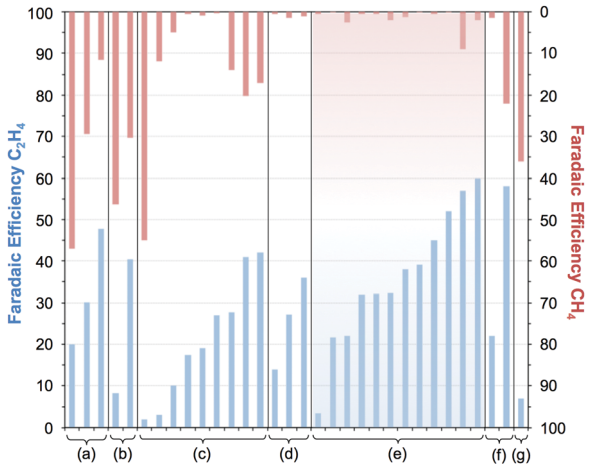

Fig. 22 Reported Faradaic efficiencies for CH_4 and C_2H_4 over Cu-based electrocatalysts. Representative reports were organized by the underlying strategy in the synthesis of the evaluated materials, and compared with (a) commonly reported Cu foil/polycrystalline Cu references. (b) Single crystal electrodes, (c) nanostructures, (d) enhanced surface roughness, (e) Cu_2O-derived electrodes, (f) surface modification studies (*e.g.* chlorine-induced), and (g) Cu-based alloys. Data are compared on the basis of a maximization of the C_2H_4 to CH_4 ratios in each study. Further details and respective references have been conveniently summarized in Table 2.

Said reports have shed light on the e-CO_2RR to methanol on Au–W and Au–Cd alloys,[231,330] whereas Cu-incorporated alloys have been developed as an alternative to cost-ineffective Au and Ag in the highly selective CO production.[331]

In the design of an efficiency-enhanced electrocatalytic system, Peterson suggested that Cu-alloying is preferential with metals with higher oxygen affinity, allowing CHO* to bind to the surface through both the carbon and oxygen atoms, thus increasing its stability without affecting the stability of CO.[234] A comprehensive investigation of Cu-alloy electrodes was carried out considering Ni, Pb, Sn, Zn, Cd, and Ag.[332] Limtrakul assessed the formation of CH_4 on Cu-based alloy (Cu_3X) stepped surfaces, with X = Ag, Au, Co, Ni, Pd, Pt, Rh, and Ir, using density functional theory calculations.[333] With the exception of Cu_3Pd and Cu_3Pt, the alloys were shown to be more energetically favorable toward CH_4 as compared to methanol. Alloying Cu with high OH affinity metals (*i.e.* Co, Ni, Ir, and Rh) showed an increasing OH* surface poisoning as compared to the pure Cu surface, while possibly suppressing HER. Conversely, alloys with Au, Ag, Pd, and Pt, improved the OH* removal step while promoting the HER.[333] Peterson rationalized a high selectivity toward CH_4 on Cu–Pt alloys based on the presence of Pt centers, which was believed to facilitate the protonation of CO* adsorbed on adjacent Cu active sites.[334]

Research focused on Au–Cu alloys showed enhanced formate, methane and ethylene formation over Au_3Cu nanocrystals as compared with monometallic Au counterparts,[335] the results being in line with an enhanced selectivity toward methanol and ethanol, claimed elsewhere.[336] Comparatively, Cu seems to have a more suitable binding strength for both of the adsorbed intermediates to facilitate the conversion toward hydrocarbons with superior FE.[327] Cu–Ag alloys showed high selectivity for the formation of C_2 compounds, but maximum FE to CH_3CHO (24%), C_2H_5OH (17%), and C_2H_4 (13%) recorded with a Cu/Ag ratio of 28/72 in CO_2-saturated 0.1 $KHCO_3$ reflected a relatively poor product selectivity.[337] Similarly, the analysis of Cu–Co thin films covering the complete compositional range revealed a shift in selectivity toward C_2 products (ethylene and ethanol).[338] Between 5 and 15 at% Co, the change in adsorption energies induced a change from CHO* to COH* intermediates, or to a favored CO–CO dimerization, both believed to be advantageous toward C_2. The above-listed results reflect the limitations in improving Cu-based catalysts through alloying strategies.

More interesting results were recently obtained with non-Cu containing alloy-based studies on nickel–gallium films (NiGa, Ni_3Ga, and Ni_5Ga_3) in e-CO_2RR to C_2H_4 and C_2H_6.[339] The onset potential at low current densities was >250 mV more positive than that of polycrystalline copper, and approximately equal to that of single crystals of copper. Similar results were obtained upon CO-based RR. Alternatively, Kortlever focused on a rationally designed bimetallic catalyst combining a metal that binds CO* strongly, Pd, with a metal that binds CO weakly, Au, in an attempt to tune the binding energy of CO.[340] The non-Cu containing catalyst was claimed to produce a mixture of C_1–C_5 hydrocarbons and soluble products at an onset potential of -0.8 V_{RHE}, tentatively formed through the polymerization of $-CH_2$ groups adsorbed on the catalyst surface.

3.3.2. The premise of single-atom catalysis. In the development of promising renewable energy conversion platforms, atomically dispersed electrocatalysts mimicking the advantages of homogeneous and biological systems, possess significant promise toward the maximization of the catalytic efficiency at a zero dimension.[341] However, along with synthesis difficulties reflecting the high surface energy of single atoms, selected supports must ensure the stability of the atomically-dispersed metal centers. In this sense, the exploitation of carbon-based materials and the introduction of other moieties, *e.g.*, S, P, and B, is believed to pave the way to enhanced activity levels. Through a convenient switching of ligands and selected metals, the different coordination and induced chemistry of these easily tunable orbital structures offers wide versatility in the resulting architectures. Relevant applications in the development of catalysts for the oxygen evolution reaction, nitrogen reduction reaction, and for the e-CO_2RR to carbon monoxide have been reported.[344–348]

It is, however, important to note that in single-atom systems there is a lack of adjacent active centers to stabilize intermediate species in C–C coupling reaction pathways believed essential in the synthesis of C_2 and C_3 hydrocarbons. In this sense, and contrary to homogeneous element dimers, trimers, or clusters, isolated active centers may be expected to inhibit CO–CO dimerization mechanisms and selectively produce C_1 species. For instance, 4% Cu–CeO_2 nanorods recently exhibited a FE of *ca.* 58% for CH_4 at -1.8 V_{RHE}, claimed to be the highest reported efficiency of CH_4 production in e-CO_2RR using H-type cells.[349] Fitted EXAFS results of these cathodes yielded an unconventionally low coordination number of Cu as 4.8 ± 0.5. The high electrocatalytic activity and selectivity were attributed to the

synergetic effect of the resulting multiple ($\approx$3) oxygen vacancy-bound single-atomic Cu active centers, where a single CO_2 molecule is strongly adsorbed, activated, and gradually reduced, as further corroborated by DFT calculations.

Conversely, while directing the synthesis of C_2H_4 may be of imposed difficulty, these authors believe focusing on this domain may further unveil analogous strategic paths of heightened importance. For instance, assessing the premise of structurally well-defined heterogeneous Cu–X–Cu bridged architectures (X being a guest atom), or alternatively, heterogeneous dual-atom catalysts incorporating adjacently placed single-atoms are suggested herein. In the latter case, the resulting selectivity is presumed to reflect the difference in the bonding strength of intermediates, according to the selected elements incorporated in the hybrid structure. Rigorous characterization and spectroscopic measurements (XANES & EXAFS) would be decisive in fully elucidating the undisclosed chemistry of the designed systems while shedding light on the corresponding mechanistic pathways.

3.3.3. Other strategies. Instead of tuning the binding energy of the reaction intermediates, one possible approach to direct product selectivity toward C–C dimerization pathways is to strategically adjust the CO* coverage. This has been recently outlined by Strasser in light of the impact of the areal density of CuO_x NP ensembles, showing that the multi-carbon product selectivity could be effectively tuned through an optimized re-adsorption of CO intermediates.[350] Seemingly independent of the applied potential and pH, the shift toward higher $\geq C_2$ selectivity was attributed to a dynamically favored diffusional interparticle coupling, which could control *CO desorption and re-absorption and the effective coverage of adsorbed intermediates. Alternatively, binary mixtures may also engender synergetic effects based on the properties of the neighboring incorporated materials, and incite a localized enhancement of CO pressure.[267] Incorporating Cu near neighboring CO-selective active centers (*e.g.* Au, Ag and Zn) emerges as a strategy to locally enhance the presence of CO species. On the basis of increased CO* coverage over Cu active centers and by utilizing the diffusional transport of CO, the resulting sequential catalysis pathway has been recently demonstrated to permit the control of oxygenate selectivity in aqueous CO_2RR.[351] The subsequent need to disentangle the intrinsic properties of incorporated multiple active centers is, however, often laborious. Established interactions between the components of hybrid architectures have been shown to arbitrate the stabilization of reaction intermediates, product selectivity, and the overall catalytic activity and process efficiency.[352,353]

A recently assessed strategy focuses on the homogeneous molecular structures and the practical handling of heterogeneous catalysts to tackle innovative possibilities for e-CO_2RR. Works of significance in homogeneous catalysis (summarized elsewhere and recommended for revision) may provide valuable inspiration for the rational design of heterogeneous catalysts.[354] A molecular copper–porphyrin complex deposited on a carbon electrode unlocked high activity, with a partial current density of 21 mA cm^{-2} for hydrocarbon production at -0.976 V_{RHE}, corresponding to turnover frequencies of 4.3 CH_4 and 1.8 C_2H_4 molecules $site^{-1}$ s^{-1}.[355] This result represents the highest catalytic activity for hydrocarbon production over a molecular e-CO_2RR, which will foment additional interest in immobilized molecule catalysts in the future. In line with the above discussion focusing on the restructuration of electrodes as a crucial platform to assess structure–reactivity correlations, Wang and co-workers have recently assessed the restructuration of Cu complexes in CO_2 methanation through *in situ* and *operando* X-ray absorption spectroscopy (XAS) characterization of representative Cu complex structures under electrochemical reaction conditions.[356]

The singularity of Cu and copper oxide-derived catalysts has only very recently faced examples of metal-free catalysts prone to catalyze e-CO_2RR through reaction pathways involving more than two electrons. The said results have reflected analogous approaches toward enhanced CO formation in carbon nanotubes and graphene oxide, in which the acidic CO_2 molecule was confirmed to find preferential adsorption onto incorporated Lewis basic pyridinic N groups.[251,252] By combining a high inherent defect density, achieved by tuning the dimensions and morphology of carbon nanostructure into nm-scale, with foreign N-doping, Wu *et al.* achieved multi-carbon hydrocarbons and oxygenates formation at high FE, high current densities and low overpotentials (Fig. 23).[357] The synthesized N-doped graphene quantum dots (NGQDs) showed high FE to CO_2RR up to 90%, with a C_2H_4 and ethanol selectivity reaching 45%, and a C_2 and C_3 product distribution and production rate comparable to those over copper (Fig. 23). With lower formation energy toward N-doping at the edge sites compared to basal planes, and a roughly estimated 44% of exposed edge sites on these quantum dots, catalytic site proximity was herein claimed to favor C–C coupling pathways toward C_2 product formation. Additional theoretical insights into the reduction pathways of CO_2 on these NGQDs were later published.[358] Studies focusing on microporous carbons of high nitrogen-content and incorporating chemically heterogeneous nitrogen species of varying reactivity are therefore expected to emerge in the future.[359]

3.4. Stability issues

In the development of CO_2RR electrocatalysts, the stability of the reported systems remains a significantly underdeveloped research area, even when extended to CO_2RR value-added products, *e.g.* formic acid attaining FE above 90% and current densities of 200 mA cm^{-2}, currently the closest to a potential commercialization break. While long-term tests are yet to be performed, assessing the stability of the reported electrocatalysts and mapping emerging drawbacks in function of the selected operating conditions are scarcely practiced.

Contextually, the durability of electrosynthesis reactors is usually measured in years, with stationary fuel cells having proven lifetimes as high as 40 000 h.[360] Following the parallelism with H_2 technologies, current values below 100 h are insufficient and require a dramatic enhancement for practical application in the future. In particular, over the Cu electrode, a notable

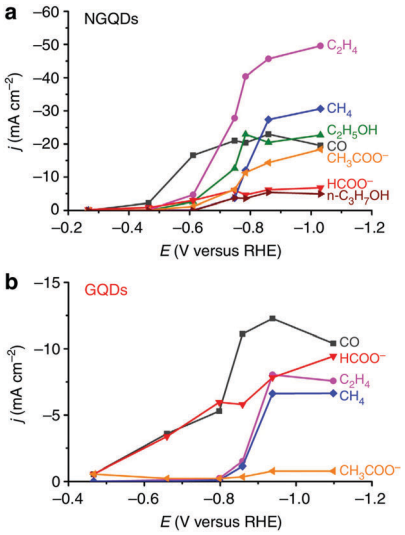

Fig. 23 Partial current densities of emerging CO_2RR products as a function of the applied potential over (a) N-doped graphene quantum dots (NGQDs) and (b) GQDs cathodes. Adapted with permission from ref. 357. Copyright 2016 Springer Nature.

deactivation of e-CO_2RR to hydrocarbons and subsequent HER dominance within a two-hour range was earlier evidenced in representative reports.[240,361,362] The nature of the species responsible for blocking and poisoning the catalytic active surface, leading to rapid activity degradation, has remained debatable in the literature. In 2005, Hori proposed that the activity decay could be derived from heavy metal impurities in the electrolyte being cathodically reduced and deposited at the electrode, as metal electrodes other than Cu are inactive toward hydrocarbon production.[363] On the basis of the observed potential of the anodic peaks, identified Fe^{2+} and Zn^{2+} in chemical reagents of the best quality were proposed as the cause of the observed catalytic decay. Suppression of the effects of metal deposition could be attained through prior purification of the electrolyte solution *via* pre-electrolysis or ion-complexation of trace metal impurities using ethylenediaminetetraacetic acid or solid-supported iminodiacetate resins over Au, Ag, and Cu electrodes.[364]

Several research groups proposed the deactivation of the Cu cathode by graphitic carbon species formed *via* the decomposition of reaction intermediates.[240,278] The accumulation of carbonaceous species on the catalytic surface has parallelism with metals that strongly bind CO*, *e.g.* Pt, Ti, Ni and Fe, evolving only H_2 from the competing water reduction. Over the Cu surface, Mul claimed that emerging COH* species in CH_4-directed pathways prompted a rapid deterioration of the hydrocarbon production rates, whereas favoring ethylene production through CO–CO dimerization could substantially hinder the activity decay up to several hours.[365] The results are of particular interest as they extend the previously discussed effects of the selected operating conditions, oxidation states, catalyst morphology, and local pH to the stability of the working electrode.[311]

As outlined in previous sections, an increasing number of reports over Cu–O combinatorial catalytic systems have demonstrated an enhancement of the FE of C_2H_4 on account of the presence of mixed Cu oxidation states and possibly subsurface oxygen. The performances of catalysts previously referenced in this review remain limited when probed from a stability point of view, *e.g.* Cu_2O film (1 h), plasma-activated Cu (5 h), and electro-redeposited Cu (1 h).[308,309,320] Alternatively, while assessing the effect of the selected pretreating reduction operating conditions, Hwang reported FE for C_2H_4 of *ca.* 40% and a remarkably superior stability up to 40 h over anodized copper $Cu(OH)_2$ catalysts prepared by a simple electrochemical synthesis method.[343] Equally surpassing stability levels reported to date, the boron-doped copper electrode developed by Sargent's team unveiled superior stability up to 40 h under continuous operation at -1.1 V_{RHE}, confirming that the $Cu^{\delta+}$ sites induced by boron doping were highly stable at the high applied potential during the CO_2RR process.[321] Comparatively, on morphology-based investigations, the ensembles of Cu NPs reported by Yang were stable for 10 h.[287]

Mechanistic uncertainties and correspondingly unaccounted poisonous carbonaceous species reflect additional drawbacks to this problem. Augustynski proposed an activation treatment, repeated every 5 min during the course of the electrolysis, involving the periodic anodic stripping of poisoning species from the active surface of the electrode.[366] Despite intervention and potentially mandatory modification on the reactor level, these results showed a facile method to extend the activity to 48 h with no activity decay being virtually witnessed. Alternatively, Wang developed surface-restructuring-based Cu electrodes with remarkable stability in the e-CO_2RR, even in electrolytes without pre-purification.[367] Pre-deposited Pd atoms on the Cu working electrode were shown to induce continuous morphological and compositional restructuration of the Cu metallic surface, inducing a stable catalytic activity up to 16 h. The strategy is expected to be extended to other foreign atoms, as demonstrated in this work upon the replacement of Pd with Rh.

3.5. Reaction cells and electrolyte-related effects

Increasing reports have focused on the implications of process variables and operating conditions, *e.g.* the effect of temperature, pressure, and CO_2 solubility on the rates of e-CO_2RR and product distribution.[243,368] Exploratory works have revealed the effect of the adsorption of anions and cations on the electrode surface, the presence of impurities, changes in the surface wettability and pH, or the impact of ion-pairing interactions with reactants and products.[365,369,370] The preferential CO_2 solubility in organic aprotic solvents has further sparked a number of increasing research works using various metallic electrodes.[371]

During their initial works, Hori alluded to the impact of the nature and composition of the electrolyte on the e-CO_2RR activity and product selectivity,[237,238] with the stabilization of the CO_2 radical being known to be impacted by the choice of the electrolyte.[372] For instance, in Hori's seminal works, the HER could be favored at FE above 70% in KH_2PO_4/K_2HPO_4, or hindered below 10% in $KClO_4$ utilizing the same catalyst.

Formation of C_2H_4 and alcohols was favored in KCl, K_2SO_4, $KClO_4$ and diluted HCO_3^- solutions, while CH_4 was preferentially produced in relatively concentrated HCO_3^- and phosphate solutions. Since CO_2 forms bicarbonate and carbonate species in alkaline solutions, selected electrolytes have also been preferentially limited to neutral and acidic pH ranges. However, with increasing the local pH following increasing proton consumption at the cathode surface, an emerging reactivity between CO_2 and evolving OH^- species is presumed in the proximity of the cathode. According to the findings of Gupta, the local pH can be up to 6 units higher, depending on the electrolyte buffer capacity, the thickness of the diffusion layer, and operating current density.[373] As the product selectivity toward CH_4 and C_2H_4 is pH-dependent, *i.e.*, it depends on the availability of hydrogen or protons on the electrode interface,[238] in electrolytes such as $KClO_4$ with low buffer capacities, high local pH is expected, enhancing the C_2 selectivity. Conversely, in buffered electrolytes like phosphate, CH_4 is favored over C_2H_4 due to a local pH close to neutral.[311] This understanding encourages the rational manipulation of the CO_2 concentration near the CO_2 reduction sites to give interesting results.[374]

H_2 production from water splitting and e-CO_2RR share several conceptual and technological features, both being cathodic in nature and the latter being ideally complemented by the oxygen evolution reaction (OER) on the anode. This has led to comparable designs for CO_2RR and water electrolysers, as reflected in the use of similar membranes, electrode types, and bipolar plates.[360] While CO_2 electrolysis in traditional electrochemical H-cells is widely appropriate for the fundamental research and screening of novel electrocatalysts, practical applications require the superior complexity of the working systems. Continuous exploratory works on the design of reaction cells have outlined the importance of separating the anodic and cathodic half-cells, *e.g.* using a cation exchange membrane (Nafion 117) to further prevent the reoxidation of CO_2 reduction products in the reaction cell. A schematic representation is given in Fig. 35 for photoelectrochemical systems. In general, experiments carried out in H-type cells do not effectively report how CO_2 electrocatalysts behave in flow reactors that are more pertinent to scalable CO_2 electrolyzer systems.

Alternatively, flow reactors have been shown to provide enhanced control over reagent delivery, enabling the use of a gaseous CO_2 feed to the cathode of the cell, and generating much higher current densities by hindering mass transport issues inherent in H-type cells (Fig. 24). In representative configurations, stainless steel plates serve as current collectors and provide electrical contact between the GDE and an external potentiostat.[375] In addition, a skewed focus from H-type to flow cells is predicted to better account for the dynamic nature of flow parameters, ion and electron transfer/transport, and the resulting electrocatalytic performance.[41] The resulting boost in the performance of e-CO_2RR platforms has been recently reflected in works on Cu dendrites, Cu nanoparticles, and electro-redeposited Cu, attaining absolute partial C_2H_4 current densities of 96.9, 150, and 161 mA cm^{-2}, respectively.[320,322,375] By the end of 2017, the collected number of papers published since 2007 on metal-based e-CO_2RR systems in continuous flow reactors remained negligible when compared with reports on research carried out in H-cells (Fig. 24a).[41]

Reported flow reactors in the e-CO_2RR are classified into two primary systems, *i.e.*, membrane-based flow cells and microfluidic reactors, with both architectures permitting an adaptive design to enhance current densities through the delivery of CO_2 to the cathode in the gas phase rather than dissolved in a liquid electrolyte. Fig. 24b and c provide schematic representations of these configurations with detailed information. Over membrane-based reactors, the choice of cation-exchange, anion-exchange, or bipolar membranes plays a key role in the kinetics of ion transport pathways between the anode and the cathode sides and the range of applicable electrolyte conditions (Fig. 24d).[376] In microfluidic cells, extensive studies have been performed concerning the properties of porous carbon gas diffusion layers, materials that are relevant to membrane reactors.[375,377] The recent contribution of Berlinguette shed light on the influence of noncatalytic components and feedstock characteristics

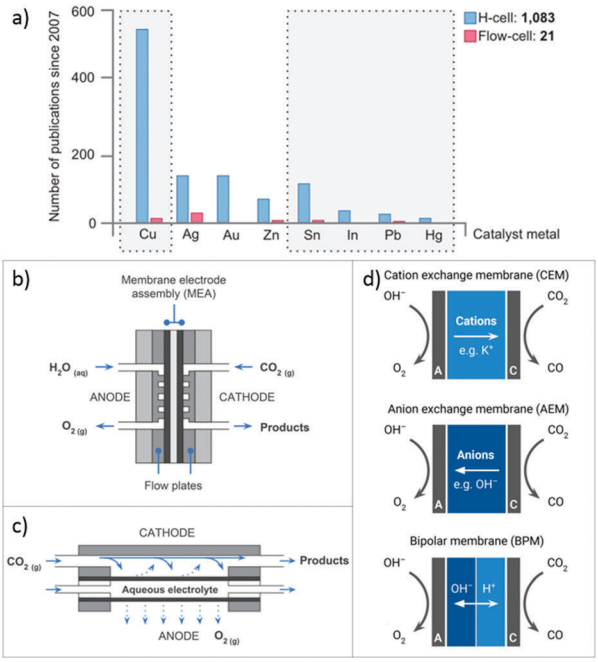

Fig. 24 (a) The number of papers published since 2007 on selected metal-based electrocatalysts for the CO_2RR in H-cells and in continuous flow reactors (data collected 29/12/2017). Cross-sectional diagrams of (b) a membrane-based reactor and (c) a microfluidic reactor. The former contains a membrane electrode assembly (MEA) consisting of the anode and cathode gas diffusion electrodes (GDEs) on either side of a polymer electrolyte membrane (PEM). In the schematized microfluidic reactor, the liquid electrolyte flows in the channel between the anode and cathode GDE materials, with CO_2 being supplied on the cathode side of the cell where it diffuses to the electrocatalyst supported on the cathode GDL. (d) Overview of different ion transport pathways between the anode and the cathode labeled "A" and "B", respectively, depending on the type of selected polymer electrolyte membrane. Readapted with permission from ref. 41. Copyright 2018 American Chemical Society.

(*e.g.*, gas *vs.* liquid, flow rate, electrolyte supply) on the overall CO_2RR performance in flow cells (*e.g.*, current density, prolonged stability, operating voltage, and selectivity).[41]

3.6. Concluding remarks and analytical prospects

We have shed light on the development of electrocatalysts toward the enhancement of the carbon chain, and the impact of factors such as the working potential, the nature of the electrolyte, and selected operating conditions (*e.g.* temperature, pressure, and resulting CO_2 solubility) on the resulting product selectivity. The underlying attention to ethylene provides insight into the C–C coupling reaction step required for the formation of multicarbon products, and the rational design of said catalysts. Being the most studied materials in the synthesis of hydrocarbons, the ability of Cu and derivatives to produce highly reduced products is a consequence of the balance of CO binding energy and further protonation of said adsorbed species as compared to other transition metals. Notwithstanding this unique capability and cost-effectiveness, prohibitively high (nearly 1 V) overpotentials, low product selectivity competing with the hydrogen evolution side reaction, and fast catalytic deactivation remain barriers to application. In addition to the limited selectivity toward long-chains, discerning the pathways that lead to the formation of alcohols, *e.g.* methanol, ethanol, or propanol, over Cu-based catalysts has remained ambiguous.

The FE toward CH_4 and C_2H_4 are particularly low as compared with CO and formate, both of which are above 90%, with the latter attaining high current densities of 200 mA cm^{-2}, highlighting the closest e-CO_2RR could lead to a potential breaking of the commercialization barrier (Fig. 15).[374,378–382] The production of ethylene and ethane show similar degrees of development, which is a step ahead of that of CH_3OH or C_2H_5OH.[360] For C_2H_4 production, multiple reports have claimed FEs greater than 40%, with nanostructuralization approaches reaching 41%, and a remarkable Faradaic selectivity of 60% belonging to a plasma-activated Cu oxide-derived surface configuration. However, on the basis of the currently observed accelerated growth toward target levels (95% FE for CO_2RR with 90% C_2 selectivity, according to technical and economic models), it is expected that these records will be broken in the future.

Specific crystallographic facets, surface roughness, the effects of nano-structuralization, induced local pH, and the presence of Cu^+ species and/or subsurface oxygen have been shown to play key roles in lowering the overpotential and enhancing the formation of C_2H_4 through dimerization reactions. Disentangling the contributions and determining the relative importance of each of them has remained an area of intense discord, with the dynamic character of Cu-based electrocatalysts prone to surface reconstruction significantly adding to the complexity of the systems discussed herein.[323] Evidence of simultaneous morphology and oxidation state evolution during reaction further underline the prominence of available *in situ* techniques expected to continue to lead the way to results of striking importance in this field, *e.g. in situ* synchrotron-based XRD and X-ray absorption techniques and eventually environmental TEM studies. The effect of the selected initial reduction conditions on the structure and chemical states of these Cu-based electrodes has been highlighted in recent reports. Using anodized copper $Cu(OH)_2$ catalysts, Hwang and colleagues proposed that harsh pretreatment reduction conditions at very negative potentials (-4.0 $V_{Ag/AgCl}$) could significantly enhance the selectivity and stability of C_2H_4 over the resulting O–Cu combination catalysts.[343] The results were attributed to the presence of mixed valences, with the harsh treatment being proposed to tune the surface properties of the oxygen-containing copper surface.

Highly efficient, robust and relatively cheap catalysts would be an effective way to push forward the e-CO_2RR on its way to industrial application. Exemplary research outcomes in the works of Cuenya and Sargent additionally highlight the remarkable progress in moving toward higher C_2H_4 to CH_4 ratios, which represent a desirable extension of the hydrocarbon chains of anticipated renewable alternative fuels.[309,320] Results are given in Table 2, emphasizing the number of recent studies close to and eventually surpassing C_2H_4 to CH_4 ratios of 100. Cu_2O-Derived electrocatalysts have proven to be able to enhance the selectivity to C_2H_4 and also dramatically reduce CH_4 yields (highlighted surface in Fig. 22). Works that may further foment the selectivity within the $\geq C_2$ range are of additional interest in the future. High paraffin selectivity has been attained upon the incorporation of a hydrogenating co-catalyst phase (*e.g.* $PdCl_x$), but works focusing on this angle have remained limited to date.[342] Nonetheless, the uniqueness of previously reported catalysts indicate the difficulty in establishing valuable guidelines in the design of analogous systems. Most importantly, the singularity of Cu and copper oxide-derived catalysts has only very recently faced heightened interest, indicating the need for new strategies. In-depth studies using microbial electrolysis cells (MEC) with electricity as an energy source and microorganisms as the catalyst are needed.[383–385] An additional alternative based on the well-established assumption of CO as a reaction intermediate could be to focus on two-step cascade processes, in which CO_2 is initially reduced to CO, with the latter being sequentially reduced toward long-chain hydrocarbons under optimized near-surface CO concentration (and consequently *CO surface coverage) conditions.

Fast forwarding three decades from the seminal works of Hori, reported studies on the e-CO_2RR still largely rely on time-consuming GC, HPLC and NMR analytical approaches that require the separate analysis of the formed products. Emerging real-time detection techniques are expected to accelerate the chances of discovery of noteworthy findings and bring the e-CO_2RR a step forward on the path toward feasibility.[312,386,387] In the design of new catalytic systems, the above-cited works often reflect nanostructure-engineering approaches leading to the formation of novel active sites capable of manipulating the reaction mechanistic paths to significantly improve the catalytic performance with high FE and low overpotentials. Alternatively, the use of redox mediators that can transfer both protons and electrons is appealing, given the multi-proton multi-electron nature of the e-CO_2RR. Striking technological advances are

expected for the process to achieve economic viability. Attained current densities determine the size of the reactor and the corresponding capital cost of the process. Mass and charge transport properties remain a prerequisite in the design of the reaction cells to accompany the optimization of the active sites developed in the catalyst toward high performance.

4. Photochemical CO_2 reduction reaction (p-CO_2RR)

The emergence of solar radiation as a clean and sustainable energy source has unlocked promising pathways to address the problems of global warming and replace traditional fossil energy in a number of chemical processes including water splitting, production of fuels, and environmental remediation.[388–390] Solar-to-fuel synthesis through the reaction of CO_2 and H_2O is considered a promising technology for the storage of solar energy in the form of chemical bonds. The light-induced CO_2RR to formic acid, formaldehyde, methanol, and methane was first demonstrated by Honda in 1979 over a library of semiconductors, *e.g.*, TiO_2, ZnO, CdS, GaP, SiC, and WO_3, in the presence of water.[391] In 1987, Grätzel demonstrated that the reaction rate for CO_2RR to CH_4 at room temperature and atmospheric pressure using highly dispersed Ru/RuO_x on TiO_2 could be sharply enhanced through photo-excitation of the support material.[64]

Fast-forwarding nearly four decades since the works of Honda, an extensive line of works has ascertained the promising character of light-responsive catalysts by the direct use of solar energy. However, the p-CO_2RR is a complex multi-step process in which light harvesting and charge separation and transfer (*i.e.*, electron and hole transport to surface reaction sites) play, in addition to surface reactions, a crucial role in the overall process efficiency. In addition to limited light harvesting and charge separation hindering improved process efficiencies, most solar-active catalysts have been shown to suffer from inefficient CO_2RR selectivity, the inability to hinder the competing HER, and catalytic instability. In-depth studies on the p-CO_2RR are still scarce, with emerging strategies to enhance CO_2 activation and the subsequent reduction lacking clarity and effectiveness. The design of highly efficient photocatalytic systems with meaningful selectivity toward C_2H_4 or longer carbon-chains remains a particular challenge. Below, we discuss the recent progress and opportunities in the development of relevant heterogeneous electrocatalysts reflecting the energetic efficiency and attained product selectivity.

4.1. Mechanistic difficulties

The CO_2RR has parallelism to water splitting technologies, which have largely accelerated the search for suitable alternatives to the common drawbacks of these solar-driven systems. Enhanced efficiency in p-CO_2RR, semiconductors with a wide optical absorption region and appropriate band edges are desirable.[392] Since the seminal works of Grätzel, an extensive semiconductor-library has been assessed in recent years to overcome the limitations of light harvesting and electron–hole recombination. Strategies to extend the light absorption under visible and near-infrared (NIR) illumination are of importance. Additionally, electron–hole recombination significantly limits the number of charge carriers available for surface reactions. Over the benchmark TiO_2, the rate of recombination of photogenerated charge-carrier pairs has been reported to reach 90% within 10 ns after their generation.[393]

While most reported CO_2RR mechanistic studies have been conducted on TiO_2, drawn conclusions are often extended to other materials. Nonetheless, the limited number of in-depth exploratory works on the photocatalytic mechanism, potential pathways, and CO_2 activation underscore the need for greater focus on these research fields.[394] Valuable strategies for enhancing the adsorption and activation of CO_2 and the factors determining the reaction pathways and selectivity for reduction products have been recently reviewed by Gong and colleagues.[395] An open discussion on e-CO_2RR, the activation of CO_2, is the subject of discord in light of the number of intermediate species in solution; *e.g.*, hydrated CO_2 molecules, carbonic acid (H_2CO_3), bicarbonate (HCO_3^-) and carbonate (CO_3^{2-}) ions. As recently assessed through isotopic experiments using $^{13}CO_2$ and *in situ* infrared spectroscopy studies in a $NaHCO_3$ aqueous solution (0.10 M), dissolved CO_2 was confirmed to be the intermediate species over a $ZnGa_2O_4/Ga_2O_3$ catalyst, whereas at corresponding pH values, H_2CO_3 and CO_3^{2-} were present only at very low concentrations.[396] HCO_3^- derived from $NaHCO_3$ was shown to not contribute to the reduction of CO_2 but to function as a buffer to enhance CO_2 dissolution. Most importantly, the single-electron reduction potential of CO_2 to the highly unstable radical anion $CO_2^{\bullet-}$ at -1.9 V_{NHE} is much more negative than the conduction band (CB) of candidate semiconductors, as shown in Fig. 25. Virtually no semiconductor provides sufficient potential to directly transfer a single photogenerated electron to a free CO_2 molecule, thus making this step highly improbable.[392] Instead, proton reduction at 0.0 V_{NHE} is more favorable, competing with CO_2 for electrons. This problem additionally aligns with (1) a preferential H_2O adsorption onto the catalyst surface as compared to CO_2, and (2) a facile transfer of only two electrons for the HER, while from a kinetics point of view, the production of the simplest hydrocarbon demands the transfer of eight electrons. These issues, therefore, highlight one of the major concerns in the p-CO_2RR, with the strongly competing HER leading to a low efficiency and selectivity.

Proposed pathways. The single addition of one electron to a free CO_2 molecule is highly unfavorable, with the emerging repulsion between the transferred electron on the electrophilic carbon atom and the free electron pairs on adjacent oxygen atoms inducing a bending of the molecular structure. Works assessing the structure and energetics of CO_2 adsorbed onto stoichiometric and oxygen vacancy-incorporated semiconductors at different facets using experimental and density functional theory slab calculations are of importance (Fig. 26).[403] For instance, the interaction of CO_2 has been claimed to be much stronger at oxygen vacancy sites of TiO_2, where a foreign oxygen atom can fill the vacancy, leading to CO_2 dissociation following electron transfer and subsequent CO evolution. The resulting

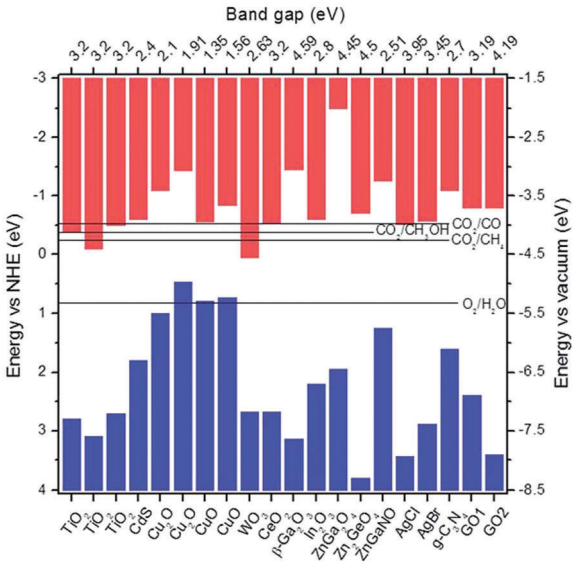

Fig. 25 Band edge positions for selected photocatalysts in the p-CO_2RR. Results summarized by Jaroniec and colleagues were based on references listed in the review. Particularly, for the listed TiO_2, Cu_2O, CuO, and GO, the reader is referred to the published works.[397–402] Reproduced with permission from ref. 392. Copyright The Royal Society of Chemistry 2015.

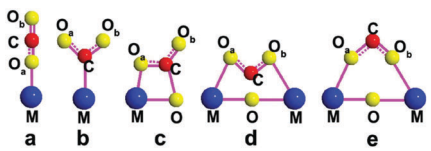

Fig. 26 Possible binding modes of CO_2 on the surface of Zn_2GeO_4. Reprinted with permission from ref. 403. Copyright 2012 American Chemical Society.

C–O cleavage provides one oxygen atom, left on the surface of TiO_2, to fill the vacancy. Alternatively, the CO_2^- radical has been proposed to bridge two Ti surface atoms forming a bidentate configuration with its oxygen atoms, a plausible intermediate step in the reduction process. With product distribution toward hydrocarbon formation being dependent on the preferred $CO_2^{\bullet -}$ binding mode, the additional surface modification of the used semiconductors is a strategy of interest.

Following CO_2 activation, the subsequent electron transfer initiates a series of chemical reactions, determining product distribution and the overall efficiency of the process. Different proposed pathways for this multistep reduction process involving a minimum of eight electrons and protons, with cleavage of C–O and formation of C–H bonds, have been recently summarized by Stolarczyk and colleagues (Fig. 27).[404] If bidentate binding occurs through both oxygen atoms to two Ti atoms, preferential attachment of a hydrogen atom to the carbon atom occurs with consecutive formate anion and formic acid formation in the absence of C–O bond cleavage. Conversely, monodentate binding through one of the oxygen atoms to a titanium atom or binding through the carbon atom to a surface-bridging O atom generally favors the formation of an adsorbed carboxyl radical, COOH. The designated formaldehyde-pathway proposes the recombination

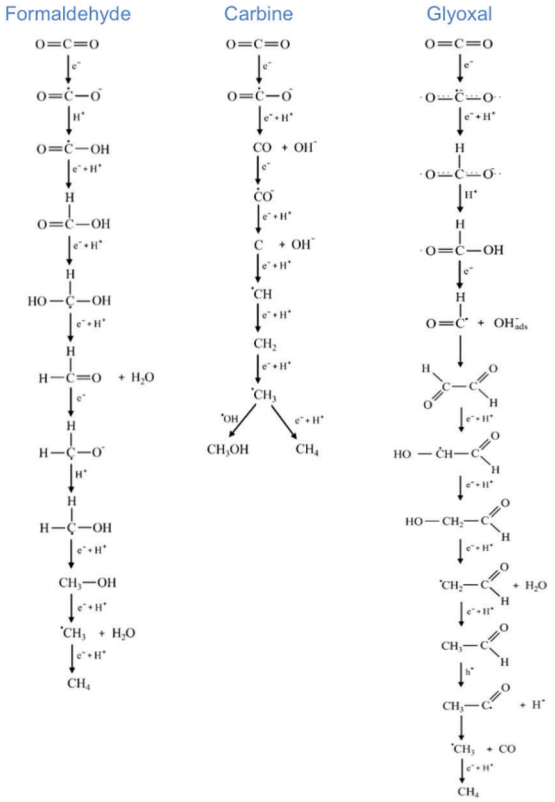

Fig. 27 Proposed formaldehyde, carbine, and glyoxal pathways for the CO_2RR to produce CH_4. Readapted with permission from ref. 404. Copyright 2013 John Wiley and Sons.

of a hydrogen radical with a carboxyl radical to form formic acid, which subsequently undergoes repeated reduction steps toward the synthesis of methane.[405] Methanol emerges here as an intermediate instead of a side product, in clear disagreement with the parallel formation of methanol and methane reported by Kočí.[406] In an alternative carbine pathway, the attachment of the hydrogen radical to the oxygen atom of the adsorbed CO_2^- intermediate prompts the immediate cleavage of the C–O bond, as opposed to what is proposed in the formaldehyde pathway where this cleavage occurs very late in the process.[406,407] The emergence of CO as a reaction intermediate is not surprising, with further hydrogenation toward hydrocarbon formation being observed. The proposed mechanism additionally accounts for the formation of a carbon residue on the surface and, subsequently, CH radicals, carbine, and a methyl radical prior to the formation of either methane or methanol. A glyoxal-based pathway involving the formation of a unique glyoxal intermediate through the dimerization of adsorbed formyl species is shown in Fig. 27. CO evolution from the aldehyde is a by-product that is commonly observed in the p-CO_2RR. Methyl radicals can also be formed from acetaldehyde along a different pathway, if the aldehyde is oxidized to acetic acid.

4.2. Semiconductors: library and engineering

4.2.1. Benchmark photocatalyst: TiO_2. TiO_2, which is the semiconductor with the most applications in photocatalysis,

has been used in environmental remediation, dye bleaching and water splitting, due to its high-efficiency, cost-effectiveness, non-toxicity, and resistance to photocorrosion. Supported or unsupported TiO_2-based materials with or without the incorporation of a co-catalyst have been proposed as attractive candidates for the p-CO_2RR.[408,409] Low formation rates and a complex (and therefore undesirable) product selectivity toward CH_4, C_2H_6 and C_2H_4 and alcohols were early reported over pristine TiO_2, stimulating an increasing number of exploratory strategies.[410,411]

Variations in the crystal structures delineate the band gaps of anatase (3.2 eV) and rutile (3.0 eV), requiring minimal photon energies of 389 and 413 nm, respectively, and hindering recombination rates on anatase up to ten times lower than rutile.[412,413] With visible and NIR light absorption exclusion accounting for *ca.* 45% and 50% of the total solar spectrum, respectively, the efficiency of TiO_2-based processes remains low. With limited photo-responsivity for large-scale application, efforts to extend the optical absorption edge of TiO_2-based photocatalysts have been pursued.[414] Besides its role in generating and separating electron–hole pairs during photoexcitation, the rational structural and morphological control of TiO_2 may further induce CO_2 activation through facile electron transfer from the surface of the semiconductor to CO_2.[415–417] Analogously, surface defects such as oxygen vacancies and step edges have been claimed to be among the most reactive sites on the surface of metal oxides.[413,418] Through scanning tunneling microscopy studies on a TiO_2(110) surface, the surface oxygen vacancies were shown to lower the activation barrier and enhance the trapping and activation of CO_2.[419] To enhance CO_2 activation on surface electron centers or Lewis basic sites, surface modification through the introduction of functional basic sites has been explored.

In order to enhance light harvesting and favor CO_2 activation, strategic steps have included the incorporation of foreign metal/non-metal species[420–422] and upconversion NPs,[423,424] bulk single-electron-trapped oxygen vacancies[425] and self-doping by Ti^{3+} and oxygen vacancies,[426,427] coupling with other semiconductors,[390] addition of hole scavengers during catalytic evaluation,[428] NaOH loading,[429] and the simple incorporation of carbon-based moieties.[430–432] N-Doping has been shown to facilitate CO_2 adsorption and promote photogenerated electron transfer, leading to superior p-CO_2RR rates. Numerous oxygen vacancies on synthesized conductive black TiO_2 can remarkably enhance the formation rate of CH_4 up to 14.3 μmol g^{-1} h^{-1}.[433] The incorporation of Mg in TiO_2 photocatalysts synthesized by the sol–gel method revealed an enhancement of the presence of Ti^{3+} species and oxygen vacancies, ascribed to a 4.5 fold greater CH_4 formation.[434] The results further corroborate reports by Xie where an 11 μmol CH_4 $g_{Ti}{}^{-1}$ h^{-1} production rate in Pt–MgO/TiO_2 systems was attained, in which MgO was proposed to strikingly promote the activation of CO_2.[435] The same authors claimed that a modification of the Pt–TiO_2 using a range of basic oxides, *e.g.* SrO, CaO, BaO, La_2O_3 and Lu_2O_3, could increase the amount of CH_4 and inhibit CO formation.

Nano-structuralization. Numerous TiO_2 morphologies *e.g.* NPs,[436] nanosheets,[437] nanotubes,[438] brookite quasi-nanocubes,[439] and hollow structures[440] with controlled crystal phases, particle sizes and surface structures have been assessed in the CO_2RR. TiO_2 NPs in the 4.5 to 29 nm-range showed an optimal average size of 14 nm for enhanced CH_4 formation activity, attributed to an optimized surface area, charge-carrier dynamics and light-harvesting efficiency.[436] Nano-structuralization may also serve as the ideal groundwork to elucidate the effect of exposed TiO_2 facets.[437] Although surfactants commonly used to control the crystal morphology often induce surface contamination, creative synthesis strategies have gained some attention. TiO_2 nanoplates, nano-octahedrons and nanorods reaching 90% of exposed low-index (001), (101) and (001) facets, respectively, unveiled decreasing CH_4 yields in the order of (010) > (101) > (001).[441] As the ability of electron–hole separation was confirmed to decrease in the opposite order (010) < (101) < (001), the results agreed with previous studies unveiling a higher CB edge for the (010)-dominant TiO_2 nanorods, and stronger CO_2 and H_2O interactions with (010) facets.[440,442] Appropriate manipulation of the ratio of co-existing facets can further boost the activity of CO_2RR to CH_4.[443–445] Recently, TiO_2 nanocrystals with co-exposed (101) and (001) facets showed enhanced CO_2RR activity as a result of the promoted spatial separation of photogenerated charges toward the different facets of TiO_2 nanocrystals.

Nanoporous supports. Works by Anpo established the significance of highly dispersed TiO_2 on zeolite frameworks toward the development of systems with high catalytic efficiency and selectivity.[446,447] Later, mesoporous and mesostructured materials, exhibiting well-dispersed active centers and large pores suitable for the facile diffusion of sterically hindered molecules, were suggested as potential host candidates in photocatalytic systems. These have included hierarchical silica materials and corresponding aluminosilicates; *e.g.*, MCM-41, MCM-48, SBA-15, KIT-6, and FSM-16 have been commonly reported.[448–451] CH_4 product yields commonly reported per wt of Ti attained values notably superior to the P25 reference. A 100 μmol CH_4 $g_{Ti}{}^{-1}$ h^{-1} production rate with Ti-SBA-15 remains the highest reported value, although a calculation inaccuracy may arise from the reported Si/Ti ratio (270) in this case.[450] The development of TiO_2 mesoporous and macroporous architectures and more recently other metal oxide mesostructures of relevance has emerged in recent years as an expected follow-up to these studies.

Results discussed herein have been summarized in Table 3, providing a direct comparison of corresponding CH_4 production rates. Improvements in the efficiency of TiO_2 as evidenced in this section appear, however, to remain mostly ineffectual toward desirable CH_4 formation rates and denote the need to study other semiconductors and develop innovative catalytic systems. In addition, several of the reported strategies fail to uniquely promote the CO_2RR, favoring the undesirable HER and reducing the overall efficiency of the process.

4.2.2. Reduction of CO_2 on other semiconductors. Since the early stages of the p-CO_2RR, an extensive library of

Table 3 Formation rates (μmol g^{-1} h^{-1}) for CH_4 (unless otherwise indicated) on representative TiO_2-based photocatalysts reported in the literature. Photocatalysts are organized in accordance with the underlying synthesis strategy in the corresponding papers for an effective comparison with commonly reported pristine TiO_2 (a). In detail, (b) single crystal TiO_2, (c) nanostructures, (d) highly dispersed TiO_2 on aluminosilicate frameworks, (e) phase junctions between TiO_2 polymorphs, (f) materials following surface modification, (g) quantum-dots sensitization, (h) co-catalyst incorporation, and (i) carbon-incorporation. Catalysts reflecting the most promising results in the current state-of-the-art have been conveniently italicized

	Catalyst	Co-catalyst	Light source	Rate (μmol g^{-1} h^{-1})	Ref.
a	TiO_2 (pellets)	—	4.8 W UVC (253.7 nm)	0.001	409
	Anatase TiO_2	—	300 W Xe lamp	0.04	413
	P25	—	100 W Hg lamp (>250 nm)	0.37	447
	Anatase TiO_2 (presence of 2-propanol as a hole scavenger)	—	350 nm light source	0.88	428
	TS-1	—	100 W Hg lamp (>250 nm)	1.27	447
	P25	—	300 W Xe lamp (<700 nm)	2.52	417
b	Anatase TiO_2(001)	—	300 W Hg lamp	0.19	441
	Anatase TiO_2(101)	—	300 W Hg lamp	0.74	441
	Anatase TiO_2(010)	—	300 W Hg lamp	1.25	441
c	TiO_2 nanocubes	—	100 W Hg vapor (365 nm)	3.6 μmol m^{-2} h^{-1}	438
	TiO_2 cuboids	—	300 W Xe lamp (>300 nm)	8 ppm g^{-1} h^{-1}	437
	Anatase TiO_2 nanosheets, 95% (100) facets	—	300 W Xe lamp (>300 nm)	35 ppm g^{-1} h^{-1}	437
	Fluorinated anatase TiO_2 NS, (001) : (101) of 72 : 28	—	18 W Hg lamp (245 nm)	0.21	443
	Anatase TiO_2 nanoparticles (14 nm)	—	Hg lamp (254 nm)	0.40	436
	Hollow anatase TiO_2 single crystals	1 wt% RuO_2	300 W Xe lamp	1.2	440
	Anatase TiO_2, co-exposed (001) and (101) facets	—	300 W Xe lamp	1.35	444
	Titania ($Ti_{0.91}O_2$) nanosheets	—	300 W Xe lamp	1.43	534
	Hollow anatase TiO_2 mesocrystals, dominant (101) facets	1 wt% RuO_2	300 W Xe lamp	1.75	440
	Nano-sized anatase rods, dominant (010) facets	1 wt% Pt	300 W Xe lamp	2.5	442
	Cubic anatase TiO_2 nanocrystals (100 ± 13 nm)	—	300 W Xe lamp	4.6	445
d	Ti-BEA zeolite (synthesis under OH^- conditions)	—	100 W Hg lamp (>250 nm)	5.76	447
	Ti-MCM-48 zeolite (Si/Ti = 80)	—	100 W Hg lamp (>250 nm)	7.5	450
	Ti-MCM-48 zeolite	1 wt% Pt	Hg lamp (>280 nm)	12.26	449
e	Anatase-rutile TiO_2 (sintered in air at 773 K)	—	450 W Hg lamp	35.4	487
	Rutile TiO_2 NP decorated on anatase TiO_2 nanorods	—	300 W Hg lamp (365 nm)	2.36	489
f	Brookite TiO_2 (treated under He at 493 K)	—	300 W Xe lamp	0.31	413
	Anatase TiO_2 (treated under He at 493 K)	—	300 W Xe lamp	0.42	413
	0.2% MgO–TiO_2	—	550 W Xe lamp, AM 1.5G filter	1.0	434
	3% NaOH-surface modification TiO_2 (ST01)	—	300 W Xe lamp	8.7	429
	1.0% MgO–TiO_2	2 wt% Pt	100 W Xe lamp (320–780 nm)	11.0	435
	Crystalline core–amorphous shell black TiO_2 (TiO_2@TiO_{2-x})	—	Solar irradiation	14.3	433
g	4 nm PbS quantum dots sensitized-TiO_2	2 wt% Cu	300 W Xe lamp	0.58; 0.31 (C_2H_6)	492
	1 at% CdSe quantum dots sensitized-TiO_2	0.5 at% Pt	300 W Xe lamp (>420 nm)	0.6	491
h	TiO_2	0.5 : 0.5 wt% Cu : Fe	UVA (320–500 nm)	0.91; 0.58 (C_2H_4)	511
	TiO_2	Pt–Cu_2O	300 W Xe lamp (300–400 nm)	1.42	455
	TiO_2	0.5% Ag	100 W Xe lamp (320–780 nm)	2.1	507
	TiO_2	0.5% Au	100 W Xe lamp (320–780 nm)	3.1	507
	TiO_2	0.5% Rh	100 W Xe lamp (320–780 nm)	3.5	507
	TiO_2	0.5% Pd	100 W Xe lamp (320–780 nm)	4.3	507
	TiO_2	0.5% Pt	100 W Xe lamp (320–780 nm)	5.2	507
	TiO_2	1.5 wt% Cu	200 W Xe lamp (320–780 nm)	8.7	514
	TiO_2–SiO_2	0.5 wt% Cu	Xe lamp	10	509
	TiO_2	0.89 wt% Pt	200 W Xe lamp (320–780 nm)	11	514
	TiO_2	12.5 wt% Pd_7Cu_1	300 W Xe lamp	19.6	513
	TiO_2	0.92 : 1.7 wt% Pt : Cu	200 W Xe lamp (320–780 nm)	33	514
	TiO_2	1.0 wt% Pd	150 W Hg lamp	118.2	508
	TiO_2 (thin film)	*1.5 wt% Au*	*1000 W Xe lamp (AM 1.5)*	*210*	*407*
	TiO_2 (thin film)	*1.5 wt% Cu*	*1000 W Xe lamp (AM 1.5)*	*280*	*407*
	$SrTiO_3$/TiO_2	*Au_3Cu*	*300 W Xe lamp*	*3770 (CO)* *421.2* *190.1 (C_2H_6)* *73.3 (C_2H_4)* *40.8 (C_3H_6)*	*538*
	1D TiO_2 single crystals	*0.94 at% Pt (1.04 nm)*	*400 W Xe lamp (250–388 nm)*	*1361*	*397*
	TiO_2 (thin film)	*1.5 wt% Au_1Cu_2*	*1000 W Xe lamp (AM 1.5)*	*2200*	*407*
i	TiO_2-Activated carbon	—	15 W UVA (365 nm)	4.31	535
	Carbon@TiO_2 hollow structure	—	Simulated solar light (>200 nm)	4.79	536
	TiO_2–graphene 2D sandwich-like hybrid nanosheets	—	500 W Xe lamp	8; 16.8 (C_2H_6)	537
	TiO_2–multi-walled carbon nanotube	—	15 W UVA (365 nm)	11.74	535

semiconductors, including transition or main group metal oxides, oxynitrides, sulfides, phosphides, and chalcogenides with both narrow and wide band gap semiconductors, has been evaluated as valuable alternatives to TiO_2-based photocatalysts.[391,394] Recent research has focused on novel visible-light-responsive semiconductors, *e.g.* ZnTe, $BiVO_4$, $InTaO_4$, and $CuFeO_2$, reflecting the progress made in the past decade in the synthesis of mesoporous metal oxides containing more than one type of metal. For instance, a 4.97 μmol g^{-1} h^{-1} CH_4 production rate could be attained with unprecedented cobalt telluride superstructures.[452] Following inspiring water splitting reports, Cu_2O has been the object of many recent studies.[453–455] In contrast, non-traditional semiconductor materials, *e.g.* zeolite and zeotype molecular sieves and layered double hydroxides (LDHs), have remained relatively unexplored in this field. The facilitated activation of CO_2 coupled with the development of catalyst architectures displaying high surface area may however be of relevance in the future, as recently demonstrated by Wang and colleagues over silicoaluminophosphate SAPO-5 nanosheets.[456] Similarly, water splitting-inspired functionalized LDHs have been suggested as alternative and promising candidates in the reduction of CO_2 to CO.[457–459]

Strategies followed for the enhancement of the performance of TiO_2 have been applied in other semiconductors. Carbon and nitrogen co-doped sodium titanate nanotubes showed enhanced CH_4 formation (9.75 μmol g^{-1} h^{-1}) that was 2.7 times higher as compared to the un-doped counterpart (3.7 μmol g^{-1} h^{-1}).[460] Oxygen-vacancy-rich ultrathin $W_{18}O_{49}$ nanowires up to several micrometers long with unique optical properties, *i.e.* NIR absorption and blue-light emission, revealed an unexpected ability to photochemically reduce carbon dioxide to methane as a result of the defect structure.[461] Nano-structuralization approaches have been shown to facilitate efficient charge separation and transportation, and superior p-CO_2RR performance,[462–465] as recently reviewed by Kang and colleagues.[466] A resulting advantage is to tune different crystal facets to optimize the reactivity of a photocatalyst for targeted reactions. Although quasi-cubic-like WO_3 crystals with nearly equal percentages of (002), (200) and (020) facets remained relatively inactive for the p-CO_2RR, rectangular sheet-like WO_3 crystals with predominant (002) facets and CB elevated to *ca.* 0.3 eV were able to generate CH_4 in the presence of H_2O vapor.[467]

Among the non-titania evaluated photocatalysts, Zn_2GeO_4 and $ZnGa_2O_4$ have shown great promise to facilitate the p-CO_2RR to CH_4 due to their high CB positions (Fig. 25). When compared with TiO_2, however, both materials exhibited significantly larger band gaps, 4.5 and 4.45 eV, respectively, limiting their light absorption. To tentatively narrow the band gap of these materials and improve light harvesting, several approaches have been pursued.[468,469] Ultra-long 7 nm-thick 20–50 nm-wide Zn_2GeO_4 nanobelts were shown to greatly enhance the activity to CH_4 in the presence of water vapor,[470] with the results being ascribed to an enhancement of its intrinsically low specific surface area as later corroborated by analogous studies.[471,472] Similarly porous Ga_2O_3 with a 2-fold enhanced specific surface area unveiled a 3-fold CO_2 uptake and a 4-fold CH_4 yield, as compared to commercial counterparts.[473] CO_2 adsorption on Zn_2GeO_4(001) was shown to be higher than on (010) facets and, in particular, near surface oxygen vacancy centers, where CO_2 dissociates to CO filling the vacancy with its oxygen atom.[403] Single-crystalline ultrathin $ZnGa_2O_4$ nanosheets with exposed (110) facets attained a 35% enhanced CH_4 yield with an apparent quantum efficiency (AQE) of 0.035% at a wavelength of 280 ± 15 nm as compared to *meso*-$ZnGa_2O_4$, despite the latter possessing a 2-fold larger surface area.[474] Similarly, Yan demonstrated the impact of surface energetics as compared with sole surface area enhancement.[475] $ZnGa_2O_4$ nanocubes with preferentially exposed (100) facets exhibited improved performance in the p-CO_2RR to produce CH_4 (6.7-fold yield enhancement), or water splitting into H_2, when compared with a mesoporous counterpart with a 10-fold larger specific surface area. In accordance with results previously discussed for N-doped TiO_2, the incorporation of nitrogen over Ga and Ge-based semiconductors has been shown to dramatically narrow the band gap to *ca.* 2.6 eV, enhancing light absorption in the visible region.[476–478]

A well-known limitation of using sulfides is reflected in their poor photostability and short lifetimes. However, attractive native candidates for visible light-driven photocatalysis, *e.g.* cadmium sulfide (CdS) with a narrow bandgap, have shown adequate thermodynamic requirements for water splitting, CO_2RR, and dye degradation.[479] The CB edge position is relatively more negative than that of TiO_2, indicating that the photogenerated electrons possess stronger reduction power in the reaction. In addition to the observed tendency toward photocorrosion, deficient adsorption capacity toward reactants, and interparticle aggregation, the photocatalytic activity of the pure CdS semiconductor material remains far from the requirements for practical application.[480] Following an obvious parallelism to the incorporation of oxygen vacancies on oxide materials, sulfide-based photocatalysts have shown enhanced p-CO_2RR activity in the presence of induced sulfur vacancies on the surface acting as adsorptive sites for the CO_2 molecule.[481] Vertically oriented Cu_2S and CuS nanowalls, nanoleafs and rods bearing three-dimensional (3D) dendritic nanobranches were additionally assessed under AM 1.5 simulated light irradiation in the p-CO_2RR toward CH_4 formation with a production rate as high as 38 μmol m^{-2} h^{-1}.[482]

The slightly more reductive CB niobates, with a perovskite structure, share several properties with titanates (nontoxicity, stability, indirect wide band gap).[483,484] $NaNbO_3$ nanowires with a diameter of about 100 nm and a length up to several tens micrometers showed enhanced activity as compared with microstructured-counterparts for CH_4 production, possibly due to crystallinity, surface-to-volume ratio and anisotropic aspect.[485] Conversely, lamellar perovskite niobates showed great promise for the separation and transfer of photoexcited charges, deposition of co-catalysts, and selective intercalation of reactants. Because of the hydrophilic nature and Brønsted acidity, 50 nm-thick, 300–500 nm-wide acidic HNb_3O_8 nanobelts prepared by a hydrothermal method also showed a two-fold and ten-fold enhanced photocatalytic activity toward CH_4 formation as compared with a KNb_3O_8-counterpart and P25 particles, respectively.[486]

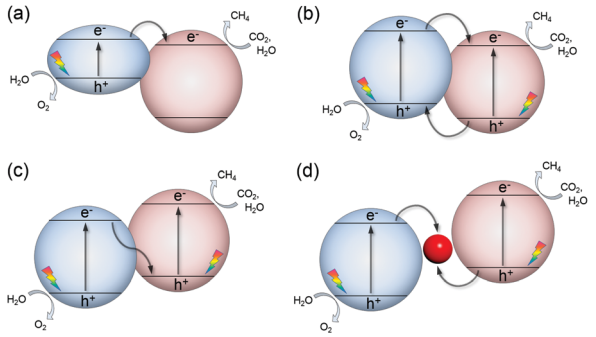

Fig. 28 Schematic representation of formed heterojunctions in the p-CO_2RR. (a) Sensitization, (b) staggered type heterojunctions, and Z-scheme systems (c) in the absence of a mediator or (d) in the presence of conductive solid mediators (*e.g.* Au nanoparticles).

4.2.3. Heterojunctions. The separation of photogenerated charge carriers can be strategically promoted at the interface between two or more semiconductors possessing different band-edge positions (Fig. 28). Following the same principle, the design of phase junctions has been similarly established in a simple manner between TiO_2 polymorphs toward higher CH_4 production.[487–489]

In quantum confined spherical NPs, or quantum dots (QDs), the quantum confinement effect gives rise to new properties that are unachievable in traditional bulk materials.[490] Acting as an antenna in the adsorption of visible light, the incorporation of QDs with tunable size (and therefore tunable band gaps) has been assessed in the p-CO_2RR. Toward the enhancement of Pt–TiO_2 photocatalytic systems under visible light irradiation ($\lambda > 420$ nm), the incorporation of CdSe QDs primarily yielded CH_4.[491] The sensitization mechanism was achieved through the transfer of generated electrons from the CB of CdSe to that of TiO_2, as the quantum confinement shifts the CB of CdSe QDs to higher energies, facilitating charge injection (Fig. 28a). The authors later incorporated PbS QDs within a 3 to 5 nm range over Cu–TiO_2, with similar CH_4 formation rates (below 1 μmol g^{-1} h^{-1}) being obtained in both studies.[492] In addition, on the basis of its well-known propensity to photocorrosion, the PbS QD-incorporated photocatalyst became inactive after *ca.* 8 h of continuous visible light illumination. With increasing application in the development of solar cells, photodetectors and biological labels, PbS QD are nonetheless expected to benefit from recent works toward efficient synthesis methods within a wide size range employing lower cost, less toxicity and safer precursors.[493] Recently, halide perovskite $CsPbBr_3$ QDs under AM 1.5G simulated illumination showed steady generation and injection of electrons into CO_2 with a selectivity of over 93.3% and a CO_2 reduction up to 23.7 μmol g^{-1} h^{-1}.[494] The rate of electron consumption could be increased by 25.5% upon incorporation into a graphene oxide support, due to enhanced electron extraction and transport.

In staggered-type heterojunctions, the photogenerated electrons in the higher CB of one semiconductor are transferred to the lower CB of the other semiconductor, while holes are transferred from the lower valence band (VB) to the higher VB (Fig. 28b). In composite semiconductors with a p–n junction mechanism, charge carrier separation results in the additional separation of occurring redox reactions, which prevents back and side reactions and benefits the product yield. In addition to appropriate band-gaps, high surface areas and enhanced surface basicity to improve CO_2 activation are desirable features in the selection of these semiconductors. Cases of interest have been reported in recent years.[495,496] Z-scheme structures, composed of two semiconductors with the staggered alignment of band structures, have received increasing attention in water splitting research. The CB and VB of the two semiconductors do not satisfy the redox potential requirements for an overall reaction alone, but they can separately perform reduction or oxidation half reactions. The semiconductor-based system performs in the absence of a mediator, or alternatively in the presence of a reversible redox mediator (Fig. 28c) or conductive solid mediators *e.g.* Au NPs or graphene (Fig. 28d).[497]

4.3. Co-catalyst effect

Previous sections have highlighted how the reported activity of semiconductor materials for p-CO_2RR, although promising, remains relatively low (significantly below 10 μmol CH_4 g^{-1} h^{-1} for individually evaluated TiO_2), with poor selectivity toward methane and, in particular, longer carbon-chains being reported. Water splitting-inspired incorporation of co-catalysts has emerged as a promising strategy to promote the quantum yield and enhance the activity of the resulting photocatalysts. Upon illumination, electrons are expected to flow from the semiconductor to the metallic surface having a larger work function at the interface and therefore act as an electron-sink, facilitating CO_2 activation for the formation of bent $CO_2^{\bullet-}$ species (Fig. 29a).[498] With enriched electron density, metal co-catalysts are prone to promote CH_4 formation, which, although being thermodynamically more feasible than the formation of CO, requires a higher number of transferred electrons.[499] While possibly participating in the reaction, it is also important to highlight that the co-catalyst may further compete for light absorption, direct product selectivity, or impact the overall process efficiency in an undesirable way, *e.g.* by promoting the HER.[500] Because the co-catalyst can act as a light absorber and the catalyst, questions arise regarding the possibility of the photoexcitation of carriers in the metal being central to the activity, with the semiconductor acting only as a support. While

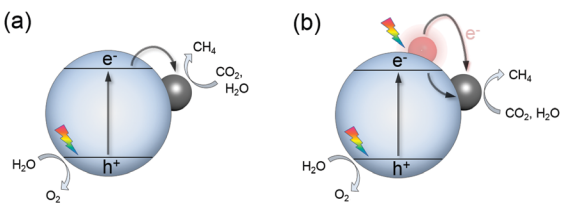

Fig. 29 (a) Schematic representation of light-induced CO_2RR in the presence of a co-catalyst acting as an electron-sink, with electron flow from the semiconductor to the metallic surface having a larger work function at the interface. (b) Plasmon-enhanced p-CO_2RR as typically explained by the direct charge transfer mechanism and local electric field enhancement.

this issue has been assessed in the literature, it deserves further attention in upcoming studies.[501]

4.3.1. Noble metals. In addition to preventing the recombination of photogenerated electron–hole pairs and facilitating mechanistic pathways requiring multiple electron transfer, suppressing photocorrosion and enhancing the stability of the resulting photocatalysts have been reported following the incorporation of noble metal co-catalysts. The co-catalyst loading level may be further adjusted to directly or indirectly affect charge transfer mechanisms, adsorption properties and light harvesting to subsequently tune the activity and product selectivity of the catalyst.[439] As hinted in previous sections, among the investigated metal co-catalysts,[502–505] Pt is one of the most promising for hydrocarbon synthesis over TiO_2-based nanostructures and other photocatalysts, *e.g.* g-C_3N_4.[412,442,506] Following their above-cited studies on the simultaneous impact of Pt and MgO incorporation leading to CH_4 rates up to 11 μmol g^{-1} h^{-1}, Wang and colleagues later confirmed that within a library of co-catalysts incorporated in bare TiO_2, CH_4 rates decreased in the order of Ag < Rh < Au < Pd < Pt.[507] Recently, palladium species loaded on TiO_2 were claimed to not only capture migrating electrons to separate electron–hole pairs but also to promote the activation of CO_2 molecules, forming active sites for CH_4 formation. Although particularly high CH_4 formation rates could be attained (118.5 μmol g^{-1} h^{-1}), it should be noted that individually evaluated TiO_2 similarly attained rather high values (14.2 μmol g^{-1} h^{-1}) as compared to the pristine TiO_2 photocatalysts assessed in analogous reports.[508] The enhancement rate (8.3-fold) upon Pd incorporation was in fact found to be similar to the values reported by Wang over Pd/TiO_2 (11.3-fold).[507] In light of similar discrepancies, the analysis of the effect of co-catalyst incorporation is preferably conducted on the basis of a reference sample evaluated under the same operating conditions, light sources and reactor configurations.

While assessing the size effect of Pt NPs coated on films with a unique one-dimensional structure of TiO_2 single crystals, the activity of these catalysts under UV light irradiation was shown to be optimal at a particle size of 1.04 ± 0.08 nm, with a calculated quantum yield of CH_4 of 2.41%, a methane production rate of *ca.* 1361 μmol g^{-1} h^{-1}, and a dramatic enhancement as compared with a pristine TiO_2-film and a P25 reference.[397] With smaller particle sizes, the energy level of Pt clusters was hinted to increase to a level higher than the CB edge of TiO_2, thus hindering the transfer of photogenerated electrons. The proposed mechanism and strategy are depicted in Fig. 30.

4.3.2. Transition metal-based materials. Despite Cu-based materials offering relative low work functions, an increasing number of works has assessed their potential in the p-CO_2RR.

Cu (identified to be Cu_2O by XPS) incorporated on TiO_2–SiO_2 systems[509] and Cu-moieties on the surface of nitrogen-doped TiO_2 nanotubes revealed enhanced CH_4 formation.[510] The presence of Fe as a co-dopant in Cu/TiO_2 systems was found to synergistically reduce CO_2 to C_2H_4 (0.58 μmol g^{-1} h^{-1}), while suppressing the production of CH_4 (0.91 μmol g^{-1} h^{-1}).[511] CH_4, C_2H_4 and C_2H_6 were obtained as major hydrocarbon products (total production rate of 574 mmol cm^{-2} h^{-1}) over bimetallic Cu–Pt co-catalysts ($Cu_{0.33}$–$Pt_{0.67}$) loaded on periodically modulated double-walled TiO_2 nanotube arrays.[512] Similar highly isolated Cu sites in a Pd lattice were shown to generate selective sites for CH_4 synthesis (19.6 μmol g^{-1} h^{-1}).[513] According to synchrotron–radiation characterizations and theoretical simulations, the isolation of Cu atoms in the Pd_7Cu_1–TiO_2 photocatalyst was claimed to (1) provide active sites for enhanced CO_2 adsorption and suppressed HER and (2) elevate the d-band center of Cu sites for improved CO_2 activation. The Cu/Pt/TiO_2 catalyst prepared by stepwise photodeposition gave a significantly enhanced CH_4 formation rate and was characterized using XPS, AES and high-sensitivity low-energy ion scattering spectroscopy.[514] These findings suggest the formation of a Pt@Cu_2O core–shell structure with optimal Cu content when the latter reached 1.7 wt%. The Cu_2O shell was believed to provide the active sites for the activation of CO_2, whereas the Pt core mainly worked for the extraction of photogenerated electrons from TiO_2.

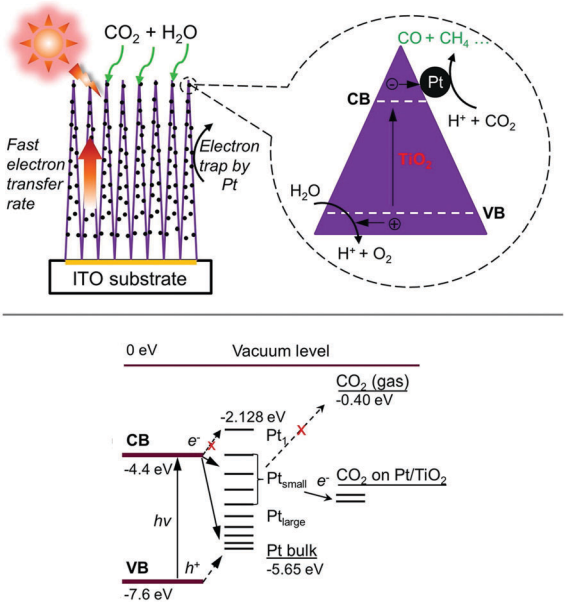

Fig. 30 Schematic diagram of the p-CO_2RR in the presence of Pt–TiO_2 nanostructured films with a remarkable CH_4 production rate (1361 μmol g^{-1} h^{-1}). Photogenerated electrons are proposed to move fast inside the highly oriented TiO_2 single crystals, flowing to the Pt deposits where the redox reaction occurs to convert CO_2 into CH_4. Readapted with permission from ref. 397. Copyright 2017 American Chemical Society.

4.3.3. Plasmonic effects. Some of the metal nanomaterials listed above, *e.g.*, Au, Ag, Cu, exhibit optical surface plasmon resonance (SPR) properties derived from the collective coherent oscillation of surface electrons, which can find desirable applications toward enhanced light harvesting efficiency. Possessing broadly tunable optical properties, plasmonic structures have found suitable applications in the fields of sensing, light-emitting materials and devices, photodetectors, plasmofluidics, photocatalysis, and photovoltaics.[515–518] High-performance plasmon-mediated electrocatalysis has recently emerged as a

valuable pathway to significantly enhance the electrochemical conversion of water and CO_2 and fuel cell reactions, as recently summarized by our group.[519]

In the photochemical society, the integration of plasmonic metal NPs on the surface of semiconductors has been largely assessed.[520] Most importantly, it has been shown that in contrast to semiconductor-based photocatalysts, photocatalytic quantum efficiencies on these plasmonic metal nanostructures can be enhanced by selected light intensities and operating temperatures.[521] The resulting plasmon-enhanced performance is typically explained either by the direct charge transfer mechanism or local electric field enhancement (Fig. 29b).[501] SPR excitation can be alternatively used to transfer photon energy in an indirect photocatalytic approach, *via* a plasmon-mediated electron-transfer pathway to molecular photocatalysts or other adjacent metals,[522] or directly utilized by the reactants and reaction intermediates adsorbed on the metal surface.[523] Over the surface of metal NPs, proposed mechanistic paths for CO_2RR have been recently presented by Jain and colleagues, as depicted schematically in Fig. 31.[263] Establishing relationships between the electronic structures of adsorbate species and plasmonic photocatalytic signatures have been pinpointed as a requirement for optimizing the rational design of these systems toward the unique control of the reaction selectivity.[524] Of equal importance, when CO_2RR occurs directly over the surface of these metal NPs, the geometry of the plasmonic nanostructure, which is well established to determine their SPR wavelength and primary plasmon decay mechanism, has not yet been evaluated in detail regarding the resulting efficiency, selectivity, and stability of the overall photocatalytic system. In each case nonetheless, the presumed existence of abundant charge-carriers has been expected to enhance the likelihood for the occurrence of multiple e^-/H^+ reactions. The assumption remains, however, under examination in the literature. Very recently, Linic highlighted a plausible skepticism for the presumed correlation between multiple electronic excitations required in multi-electron reactions (with at least 8 for the simplest hydrocarbon) utilizing plasmonic nanostructures, based on the limited occurrence of single-electron excitations taking place in these nanostructures, the corresponding short lifetimes of the photoinduced charge carriers, and the relatively long period between excitation events, particularly at low light intensities.[525] Despite the need for further investigation of the mechanistic utilization of the properties of plasmonic nanostructures, emerging examples have continuously fomented interest in this domain. Recently, Ag-loaded TiO_2 nanotube arrays showed enhanced performance in the CO_2RR to produce CH_4 under visible light, with only minor amounts of CH_3OH being detected.[526] This unique SPR effect and underlying hot electron generation induced by Ag NPs was further ascribed to coupling with the light scattering enhancement within the TiO_2 nanotube arrays effectively increasing light absorption and utilization by the Ag NP deposited in the inner spaces of these nanotubes. Similarly, Au has found suitable use in a wide range of photo and electrocatalytic applications, assuring cost-effectiveness on the basis of low required loadings and the durability of the materials toward photocorrosion. Coupling Au NPs with TiO_2 in the design of visible-light-responsive nanohybrid architectures with synergistically strong SPR effects has been shown to enhance charge separation and photocatalytic efficiency.[527] Experimental and calculated results based on Au@TiO_2 yolk–shell hollow spheres have even demonstrated the formation of C_2H_6.[528] Excluding resonance photon scattering and the direct transfer of hot electrons from Au NPs to TiO_2, in agreement with a lack of intimate contact between both components to allow the SPR-excited hot electrons to overcome the Schottky barrier between the metals and semiconductors, Zou and coworkers have attributed the observed results to local electromagnetic field enhancement. Equally remarkable, a commercial P25 modified by Au–Cu alloy NPs as a thin film unveiled a CH_4 formation rate greater than 2200 μmol g^{-1} h^{-1}, resulting in a 44-fold and a 10-fold enhancement as compared to bare TiO_2 films and corresponding Au/TiO_2 and Cu/TiO_2, respectively.[407] The selectivity toward CH_4 was claimed to arise from the presence of Cu bonding to the reaction intermediates (CO*), while the surface plasmon band of Au could introduce a visible

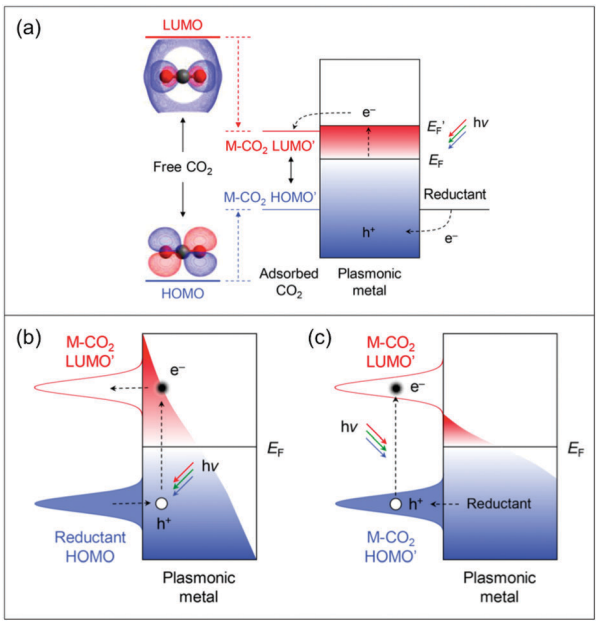

Fig. 31 Potential mechanistic scenarios for CO_2RR by plasmonic photocatalysis, as summarized by Jain and colleagues. Adsorption of CO_2 onto the surface of a metal NP prompting orbital hybridization, with a reduction of its HOMO–LUMO energy gap from the gas-phase value to a new HOMO′–LUMO′ gap, which can be excited under visible light irradiation. (a) Under steady-state light irradiation, the resulting electron injection/hole removal cathodically charges the NP, elevating the Fermi level to a quasi-Fermi level (EF′). Energetic electrons occupying states above the EF′ are thus injected into the LUMO′ of the adsorbed CO_2. (b) LSPR excitation followed by dephasing or energy relaxation within the metal NP transiently produces hot electrons above the EF. A fraction of these hot electrons has been proposed to be scattered into the unoccupied LUMO′ states of the CO_2 adsorbate, thus prompting a vibrational CO_2 activation on the surface of the NPs. (c) Direct HOMO′–LUMO′ photoexcitation of the M–CO_2 complex is facilitated in accordance with the reduction of the HOMO′–LUMO′ gap of the M–CO_2 complex. Readapted with permission from ref. 263. Copyright 2017 American Chemical Society.

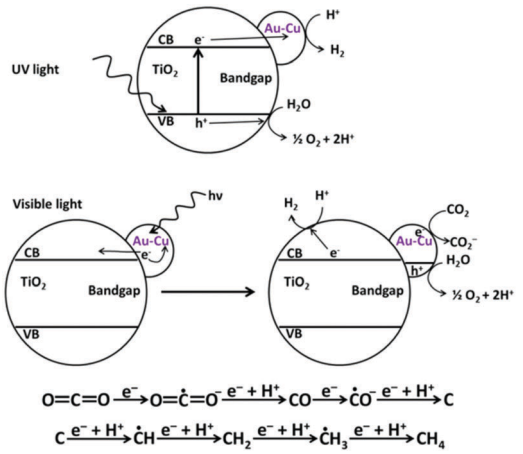

Fig. 32 Schematic representation of the proposed mechanism under UV and visible light for Au–Cu alloy NPs decorated on TiO_2 as photocatalysts, to rationalize the influence of the irradiation wavelength range on the product distribution. A proposed route for CO_2RR to CH_4 in water is represented and in accordance with the carbine mechanism given in Fig. 27. Reprinted with permission from ref. 407. Copyright 2014 American Chemical Society.

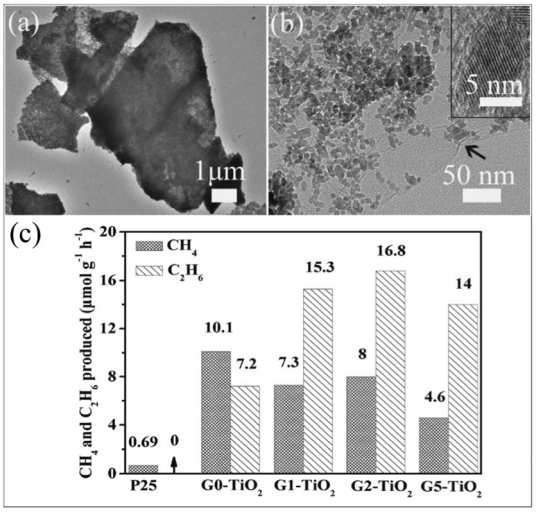

Fig. 33 (a and b) TEM photographs of sandwich-like TiO_2–graphene hybrid nanosheets (G_2–TiO_2). The inset of (b) shows an HR-TEM image evidencing the lattice fringes of the TiO_2 nanoparticles, corresponding to the (101) plane of anatase TiO_2. (c) Catalytic assessment results showing a remarkable C_2H_6 production. The weight contents of graphene were designated as *x* (wt%) in these G_x–TiO_2 nanocomposites, with the evaluated samples having 0, 1%, 2%, and 5% graphene. Readapted with permission from ref. 537. Copyright 2013 John Wiley and Sons.

light photoresponse. In agreement, hot electrons on TiO_2 favored proton reduction through the HER, and the hot-electron-induced reduction of Cu_2O to metallic Cu promoted selective activation of CO_2 to CH_4. A schematic representation of the overall mechanism is depicted in Fig. 32.

4.3.4. Carbon-based materials. Due to their appealing optoelectronic properties and creative architectural designs that often offer large specific surface areas, there has been significant growth in the application of carbon-based materials, *e.g.* graphene, graphene oxide (GO), and carbon nanotubes (conducting or semiconducting depending on their structure). The incorporation of semiconductor-based systems promotes a facile and cost-effective enhancement of light absorption in the visible range, improving light harvesting and enhanced charge separation and transport. Graphitic carbon nitrides (g-C_3N_4) have continued to attract attention due to the theoretical prediction of their promising properties.[529] With rich N-containing groups on the surface and a narrow band gap (2.7 eV), C_3N_4 is expected to facilitate CO_2 activation, and to serve as an excellent photocatalyst for the p-CO_2RR.[530] Despite their additional cost-effectiveness, C_3N_4 materials remain relatively unexplored toward the synthesis of hydrocarbons.

Electrons in the CB of TiO_2 are believed to easily migrate to graphene and to still possess enough reduction potential to promote p-CO_2RR.[531] Solvent-exfoliated graphene on GO–TiO_2 was reported to exhibit improved p-CO_2RR activity, especially under visible light.[532] Alternatively, the material dimensionality has been claimed to play a key role in determining the spectral response, charge transfer and reaction specificity of carbon–TiO_2 nanohybrid composites.[533–535] Carbon@TiO_2 hollow spherical structures with enhanced visible-light absorption and CO_2 adsorption have unveiled an improved photogenerated charge transfer efficiency and a CH_4 formation rate of 4.79 μmol g^{-1} h^{-1}.[536] Ascribed to facilitated charge carrier transfer, sandwich-like TiO_2–graphene hybrid nanosheets showed a remarkable C_2H_6 production of 16.8 μmol g^{-1} h^{-1} (Fig. 33).[537]

4.3.5. Concluding remarks. An effective comparison of the wide range of approaches reported herein toward the enhanced synthesis of CH_4 over TiO_2-based systems, and a presumed valuable guideline for the efficiency of the proposed systems is presented in Fig. 34. The compared systems reflect the strategies incorporating co-catalysts, single crystals, nanostructures, phase junctions, and surface modifications amongst other strategies thoroughly revised in Section 4.2. A summary of the detailed experiments is provided in Table 3, in which the most promising results have been highlighted. As observed earlier, most of the reports lead to CH_4 production rates that are significantly below the 10^2 μmol g^{-1} h^{-1} mark. The results categorized (h*) followed the incorporation of metal co-catalysts and underline the value of this strategy. Reflecting a currently common trend in H_2 technologies, attempting to generate a synergism between several of the above-discussed strategies will probably result in an enhancement of the rates in the near future. A representative example is the work of Ye, reporting the synthesis of a Au–Cu alloy supported on $SrTiO_3$/TiO_2 coaxial nanotube arrays. By simultaneously focusing on the effect of the incorporated Au–Cu as a co-catalyst, the design of a nanostructure and the creation of a heterojunction mechanism, the authors reported the significant production of CH_4 (421.1 μmol g^{-1} h^{-1}), although CO remained the main product (3770 μmol g^{-1} h^{-1}).[538]

4.4. The photoelectrocatalytic (PEC) CO_2RR

Despite the evident advantages of electrocatalysis as a renewable source of energy in the reduction of CO_2, the above-discussed section on the e-CO_2RR has largely underlined the large amounts

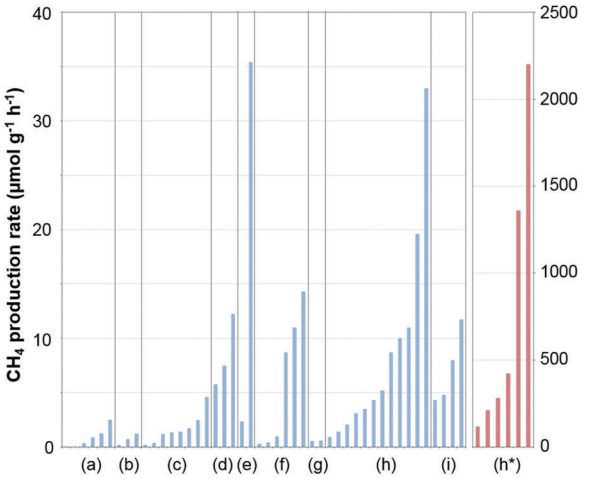

Fig. 34 Reported CH_4 production rates (μmol g^{-1} h^{-1}) on TiO_2-based catalytic systems. Reports were organized by attempted strategy and compared with (a) commonly reported pristine TiO_2 references. (b) Single crystal electrodes, (c) nanostructures, (d) highly dispersed TiO_2 on aluminosilicate frameworks, (e) phase junctions between TiO_2 polymorphs, (f) following surface modification, (g) quantum-dot sensitization, (h) co-catalyst incorporation, and (i) carbon-incorporation. Results for (h*) represent exceptionally high reports in the literature following co-catalyst incorporation, with results being discussed in corresponding sections. Details have been summarized in Table 3.

of electricity required to overcome the high-energy barriers for the reutilization of CO_2. PEC materials rationally integrate light-responsive materials prompting a significant reduction in electricity consumption and higher overall process efficiency. The use of PEC systems comprising a working photoelectrode, a counter electrode and a reference electrode has gained traction as an attractive alternative in analogous H_2 technologies. The PEC system is expected to attain higher efficiency levels with the application of an external bias to promote the separation of photogenerated charge carriers. Semiconductors have been reported as photoanodes, photocathodes, or simultaneously applied in designed PEC systems. As photocathodes, p-type semiconductors have been featured in a number of exploratory works with Pt or carbon rods as dark anodes of choice. Here, the photoelectrode harvests light to generate charge electrons and holes and performs a half-cell reaction to reduce CO_2. Assessed materials listed in recent comprehensive reviews include p-GaP, p-Si, p-GaAs, p-InP, p-Si, p-ZnTe, p-NiO, p-Co_3O_4, N-Ta_2O_5, and CuO.[539] Nonetheless, along with stability concerns, the efficiency toward CO_2RR has remained low as the reduction of water is prone to preferentially occurring over the surface of p-type semiconductors. In addition, on photocathode-driven PEC systems, the selectivity toward HCOOH and CO is notably superior to that of the CH_4, which emerges as a by-product with low FE values.

Alternatively, the integration of n-type semiconductor photoanodes with superior cost-effectiveness as compared to p-type cathodes has emerging potential.[540] In particular, photoanode-driven systems, *e.g.* WO_3, TiO_2, $BiVO_4$, Ge-doped GaN, may in a seemingly facile manner couple with the above-listed electrocatalysts of choice for the e-CO_2RR (*cf.* Section 3). In 1996, Ichikawa reported a TiO_2 photoanode-driven single unit PEC system operated under pulse bias that was claimed to have superior activity and selectivity toward a stable hydrocarbon formation over the Cu cathode with FE of 44% and 24% for CH_4 and C_2H_4, respectively.[541] A PEC system incorporating TiO_2 photoanodes illuminated with 100 mW cm^2 AM 1.5G light and a Cu_2O cathode was reported by Chang for CH_4 synthesis, attaining FE of 54.6%.[542] In a similar fashion, Grimes and colleagues reported a PEC photocathode comprised of p-type Si nanowire arrays, with and without copper sensitization, paired with n-type TiO_2 nanotube array films as the photoanode. Along with CO and substantial rates of hydrogen generation due to water photoelectrolysis, CH_4, C_2H_4 and even traces of C_3–C_4 hydrocarbons could be observed at an applied potential of 1.5 $V_{Ag/AgCl}$.[543] A Cu cathode coupled with visible-light responsive WO_3 as the photoanode unveiled superior energy efficiency and FE toward CH_4 and C_2H_4 of 42.3% and 4.0% at 0.55 V_{RHE}, or alternatively 67.0% and 0.6% at 0.75 V_{RHE}.[544] Prior e-CO_2RR reports on a Cu cathode include the works of Lee and colleagues using a carbonate-coordinated cobalt/$BiVO_4$/WO_3 photoanode exhibiting unique effectiveness as a water oxidation activity catalyst, comparable to state-of-the-art values.[545] Most importantly, the PEC system showed stable photocurrent and a FE of 51.9% for CO and hydrocarbons in the C_1–C_2 range, balanced by an exclusive H_2 formation.

Although the above reports and the underlying FE attained for CH_4 and C_2H_4 may emerge as pale comparisons to the exemplary e-CO_2RR reports scrutinized in Section 3, exploring the energetic advantages of PEC cells as compared to electrocatalytic platforms deserves more attention in the future. In particular, the knowledge acquired to date on Cu-based electrocatalysts could serve as a valuable guideline toward notably superior efficiencies of the systems discussed herein.

4.5. Stability issues

To date, exploratory works for the development of CO_2RR photocatalysts have only sparingly assessed the durability of the reported materials. Measured stability ranges and ascribed bottlenecks either related to the material itself or the selected operating conditions have received little attention as compared to their electrocatalytic CO_2RR counterparts. The number of available reports is further narrowed when solely reports regarding the synthesis of hydrocarbons are considered. In photocatalytic applications, the stability is measured in continuous cycles of 6 to 8 hours. Among the current listed state-of-the-art catalysts having competitive results, Au–Cu NPs on $SrTiO_3$/TiO_2 coaxial nanotube arrays were stable for five cycles during a 34 h test.[538] Garcia corroborated the stability of the reported 1.5 wt% Au_1Cu_2/TiO_2 (thin film) for a period of 46 h of irradiation based on the linearity found for the temporal evolution of H_2 and CH_4 production.[407] For possible practical applications, the development of technologies for prolonging the catalyst lifetime is imperative.

The photocorrosion of selected photocatalysts has emerged as one of the main issues in the development and application

of durable materials in p-CO_2RR systems. As the benchmark photocatalyst with high catalytic efficiency in p-CO_2RR, anatase TiO_2 exhibits high stability and durability with a low tendency to undergo deactivation and photocorrosion.[408] In attempts to enhance light harvesting, doping with transition metals in minute quantities can replace titanium atoms in the lattice and introduce empty orbitals at energies below the CB of pure TiO_2. This has been shown to lead to the reorganization of the crystal lattice, resulting in the leaching of the dopant metal out of the crystal framework, undesirable photodissolution, and enhanced catalytic decay.[546] Alternatively, doping with non-metallic elements, *e.g.*, N, S, and C, results in the introduction of occupied orbitals above the energy of the VB, narrower energy gaps and a proposed enhancement in the durability of TiO_2-based photocatalysts.[547]

Along with studies utilizing TiO_2-based materials, most reported architectures exhibit pronounced catalytic decay within the first hours of catalytic assessment. In parallel water splitting applications, preventing photocatalysts from coming into contact with the electrolyte through the introduction of dense coatings has been shown to lead solely to a limited enhancement in the resulting stability. In p-CO_2RR, an example worth highlighting involves metal sulfides with photogenerated holes in their valence band not being energetic enough to oxidize water and resulting instead in their irreversible photo-corrosion. Here, hole scavengers may serve as a simplified approach to extend their stability. Serving as electron sink and thus enhancing the activity of photocatalytic platforms, the incorporation of metal co-catalysts should be cautiously pondered in slowing down the photocorrosion of semiconductors by enhancing the timely consumption of photogenerated charges. The stability of the incorporated co-catalyst deserves additional attention. With plasmon-enhanced nanostructures, the stability of the incorporated noble metals depends on their redox potential, with Au emerging as the most promising candidate in these studies due to the absence of photo-corrosion. Although at an underdeveloped stage, the utilization of plasmonic Au photocatalysts, with the reaction occurring directly over the surface of these metal NPs, could promising in the near future.[524]

4.6. Photocatalytic reactors

Although solar energy conversion continues to emerge as a valuable pathway to replace traditional fossil energy, the design and underlying viability of photocatalytic reactors are topics of concern. In a photocatalytic system, CO_2 can be reduced over the photocatalyst suspended on a CO_2-containing electrolyte in a rather simplified reactor, with both p-CO_2RR and water oxidation occurring on different active sites present in the surface of the said photocatalyst. In the absence of hole scavengers, *e.g.* H_2O_2 and Na_2SO_3, which require additional costs and significantly contribute to implementation limitations, the formed p-CO_2RR products are susceptible to re-oxidation by photogenerated holes or the evolved oxygen. PEC cells and, as discussed for e-CO_2RR, the possibility of designing photoreactors with two separate compartments, *e.g.* using a cation exchange membrane (*e.g.* Nafion 117) are highly desirable. Schematic representations of photoelectrocatalytic reactors in two-compartment cells separated by proton-exchange membranes have been presented in Fig. 35. They reflect the configurations corresponding to the commonly utilized H-type cells in the e-CO_2RR, and in PEC systems discussed in Section 4.4, for the utilization of semiconductors as photoelectrodes, photocathodes, or both. Reducing the chance of back reactions not only enhances the overall efficiency of the process but also facilitates product separation, reducing energy costs in subsequent purification processes.[548] In addition to separation cost motivations, on a larger scale, physically separating the production of O_2 and H_2 in the reactor is necessary for safety reasons. Toward a facile process implementation however, photocatalytic-based platforms have a greater potential to be applied on a large scale as compared to photoelectrocatalytic technologies.

The investigation of alternative photo-reactors, in addition to reactor sizing and selected configurations, catalyst loading, mass transfer considerations and selected operating conditions, has remained insufficient. Recent studies, carried out in an innovative photoreactor operating under high pressure, have shed

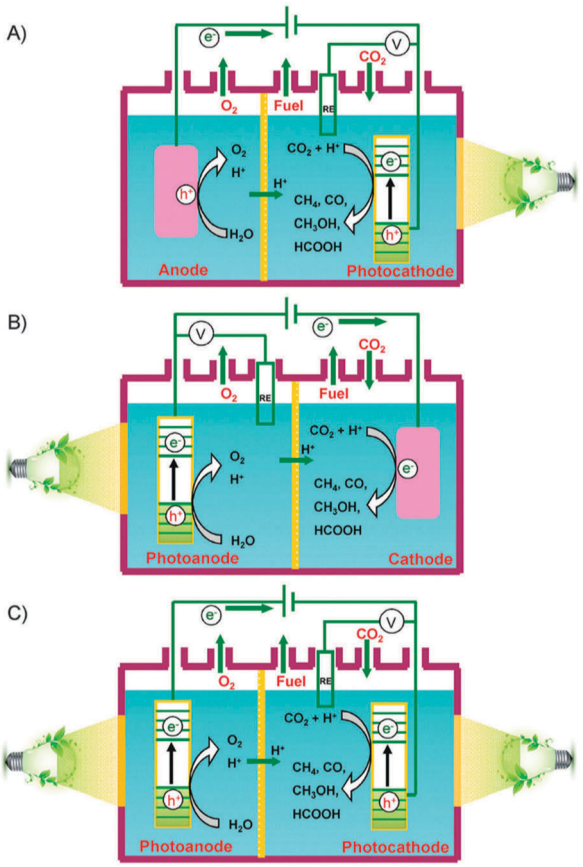

Fig. 35 Schematic representation of photoelectrocatalytic reactors in two-compartment cells separated by proton-exchange membranes. CO_2RR and water oxidation occur over the cathode and the anode sides, respectively. The alternative or simultaneous utilization of photocatalysts under light irradiation on the cathode and anode side is represented in each case. Reprinted with permission from ref. 539. Copyright The Royal Society of Chemistry 2016.

light on the complex mechanistic pathways toward both liquid and gas phase p-CO_2RR products.[549] The design of photocatalytic reactors often falls into two main categories, *i.e.* the most commonly used slurry reactor and the fixed bed reactor. In slurry-type reactors, the selected photocatalyst is vigorously stirred to attain high dispersion and prevent sedimentation as scattering properties largely depend on time-dependent agglomeration phenomena and porosity. In the development and validation of photocatalytic tests, the reactor should be additionally designed to allow the optimized exposure of catalytically active sites to light for enhanced light harvesting efficiency. The effect of selected illumination sources and lamp position are to be taken into account in the reported rates, along with a detailed investigation of the resulting radiation field and the impact of irradiation on the reaction temperature. The importance of such requirements is directly reflected in the variations found with reference catalysts as discussed above. In addition to the reactivity of the catalyst in terms of molecules of CO_2 converted, the quantum yield or efficiency, which requires measurement of the quantity of photons absorbed by the catalysts, is a measure of the effectiveness of the evaluated photocatalysts. A cautious estimation of the total transmitted radiation, transmitted non-scattered radiation, and photon back-scattered radiation exiting the system has been assessed in a limited number of works.[550]

4.7. Concluding remarks and analytical prospects

The production of hydrocarbons from CO_2 using solar energy is a promising alternative for tackling the current climate and energy problem. To date, the design and development of p-CO_2RR platforms have substantially followed the growth of water splitting technologies and the corresponding strategic pathways, which have prominently accelerated the first two mutual process steps, namely photon absorption and charge separation and transfer (*i.e.* electron and hole transport to surface reaction sites). Notwithstanding the exciting developments with the incorporation of visible light and NIR-responsive components, the low efficiency in the utilization of solar light in the process is still of marked concern. Similarly, H_2 technologies have guided the design of CO_2RR photocatalysts within a noteworthy range of materials, which is largely in contrast to the converging focus on Cu or copper oxide-derived catalysts in the e-CO_2RR. Over TiO_2-based photocatalysts, the most commonly applied photoresponsive material, CH_4 (and alternatively CH_3OH) can be the prevalent product. However, as reflected in this review, no concrete guidelines have been produced toward the synthesis of long-chain hydrocarbons to date. Reports on the formation of C_2H_4 or C_2H_6 offer limited groundwork in the establishment of analogous strategies and often fail to provide concrete mechanistic assumptions. Metal oxides and compound semiconductors with non-porous or porous nanostructures with meaningful photocatalytic activity and long-term stability remain scarce. 1D or 2D architectures can accelerate the transfer of generated carriers, with corresponding research focus being expected in the future.[539] Great progress is needed in the clarification of the reaction mechanism toward the rationalization of product distribution and enhancement of the catalytic activity in the design of innovative systems.

With limitations similar to the e-CO_2RR systems, final gaseous and liquid photoreduction products are commonly identified and quantified separately through GC and HPLC analyses, respectively. As suggested by Gong and co-workers, a number of approaches, *e.g.* EPR spectroscopy, *in situ* DRIFTS, transient absorption spectroscopy (TAS), and scanning tunneling microscopy (STM), are expected to accelerate the chances for the discovery of results of significance by unlocking unknown mechanistic details.[395] In p-CO_2RR systems, the overall process effectiveness may be drawn in terms of photon efficiency or based on the amount of loaded photocatalyst. To date, however, there is no single measure to establish a direct and unambiguous comparison between increasingly complex systems. In mapping the current literature, it is hard to find a suitable baseline among the variables of the type of light, pH of the solution, CO_2 pressure, and selected experimental conditions. As with other photocatalytic applications, p-CO_2RR suffers from a broad selection of light sources (sunlight, solar simulators or visible light), position and distance, and a lack of comparison with results under dark conditions. In each study, detailed mass balance, product distribution and catalytic stability assessments are requested.

The results assessed herein confirm that the photo-driven production of hydrocarbons from CO_2 is still far from practical consideration. The current average CH_4 productivities remain below the 10^2 μmol g^{-1} h^{-1} mark under light irradiation, requiring an increase by orders of magnitude. To date, only a few reports have attained (limiting) production rates up to 10^3 μmol g^{-1} h^{-1}, although the said findings and underlying conclusions are insufficient to dictate a clear direction for upcoming research works. Establishing synergetic effects in rationally designed architectures bridging a number of research strategies has appeared meaningful to date. The incorporation of co-catalysts and the effective enhancement of plasmonic nanostructures in these multi-electron processes have been underscored in this review. Nonetheless, the utilization of charge scavengers considered in the majority of the exploratory works revised here and beneficial in stability issues, impose important limitations. From the engineering and technological point of view, hole scavengers demand additional costs and significantly contribute to the projected implementation constraints. In addition, it is important to establish that the reported reaction products do not arise from the incorporated hole scavenger species, as recently outlined by Linic and colleagues.[525] Finally, (often undisclosed) solar-to-fuel energy conversion efficiencies unveil the technological underdevelopment of these systems as compared with water-splitting HER systems exhibiting remarkably higher solar-to-hydrogen values.[551–553] Significant improvements in the attained low conversion efficiency, product selectivity and quantum yields are required to bring p-CO_2RR in aqueous solutions closer to practical application.

5. Conclusions and outlook

In this review, the recent developments and future perspectives in CO_2 reutilization for its sustainable conversion to hydrocarbons

have been outlined. Tentatively closing the carbon cycle through the catalytically assisted thermochemical, electrochemical, and photochemical CO_2RR has unveiled promising results that may provide an answer to the growing environmental concerns and a source of alternative fuels for a sustainable future. The synthesis of longer chain hydrocarbons, toward typical gasoline and diesel carbon-chain ranges, provides the promise of a smooth transition in the utilization of alternative liquid fuels in already established infrastructures currently served by fossil fuels. Ground-breaking outcomes in this research field have, however, remained subtle to date. Mechanistic uncertainties and unidentified activation barriers for key reaction steps represent fundamental limitations to all the technologies discussed herein. Significant light is required in the identification of the nature and adsorption configuration of involved intermediate species through, for example, DFT calculations in the establishment of structure–property descriptors required in the rational design of novel catalytic systems. In addition, while the optimization of the activity, selectivity, and stability of designed catalytic systems represent decisive steps toward the eventual commercialization of such catalyst-based platforms, both CO_2 capture and distillation, along with the availability of large-volume sources of pure CO_2 remain acute drawbacks to the economic viability of these technologies.

Although only briefly assessed, it is important to further establish potential synergies between the technologies presented herein. Within the possibilities for potential commercial breaks and large-scale application of the introduced CO_2RR systems, electro- and photo-driven platforms may be valuable in the development of conventional thermochemical processes. Technical and economical analyses may be required to establish the premise of utilizing photovoltaic energy or renewable electricity to produce H_2 from water to be used in t-CO_2RR systems, or to directly reduce CO_2 in water in either electro- or photocatalytic reactors. Although the former pathway may require up to three consecutive steps in the transformation of CO_2 to hydrocarbons, the final long-term production goal should be to develop one step with the eventual facile integration of CO_2 capture from the atmosphere. Evidently, this will markedly depend on the development of the technologies reviewed herein and parallel water splitting platforms as the most promising sources of renewable H_2.

Fig. 36 establishes a comparison of the current the state-of-the-art thermochemical, electrochemical, and photochemical CO_2RR technologies, their levels of progress, and the promise of their development. Please note that the selected scales are a mere qualitative comparison of said parameters for the three technologies and represent the authors' analysis of the discussed problems. Currently, thermochemically-driven CO_2RR processes have the greatest potential to be applied on a large scale, offering the highest reaction rates and product yields, and being receptively compatible with the existing industrial plants as compared to the photo- or electrocatalytic platforms. These platforms have unveiled the most favorable shifts to long-chain hydrocarbons with high activity and selectivity in CO_2 methanation. In addition, benefiting from decades of

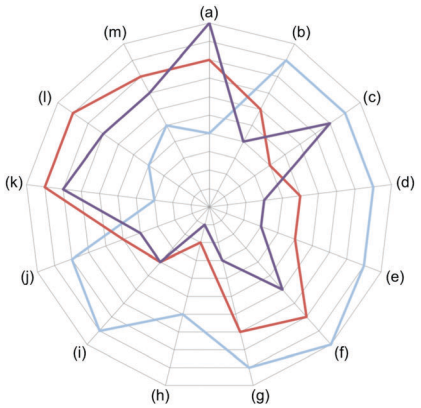

Fig. 36 A comparison of catalytically assisted thermochemical (blue), electrochemical (red), and photochemical (purple) CO_2RR platforms according to (a) the corresponding ideally predicted energy efficiency of these technologies, (b) the potential breakdown of the commercial barriers based on current reports, (c) relative scalability, (d) compared activity of state-of-the-art catalysts, (e) attained shifts to longer chain hydrocarbons, reported selectivity levels toward (f) methane, (g) olefins, and (h) long-chain hydrocarbons, (i) currently reported catalyst stability, and (j) current mechanistic clarity driving the design of novel catalytic systems. (k and l) Compare recent catalyst development and the emergence of published breakthroughs of high impact. (m) Reflects the current number of reports involving the facile synthesis of the employed catalyst. Please note that the selected scales are a mere qualitative comparison of the above-listed technological metrics for each platform and represent the authors' analysis of the discussed problems based on the extensive list of exploratory works included in this review article.

thoroughly documented research and light shed from conventional FT works, we have illustrated the promising features of Ni and Co-based, and Fe-based catalytic systems on CO_2RR to methane and long-chain hydrocarbons, respectively. Most of the current catalytic libraries reflect the increasing complexity of synthesis and therefore the need to urgently inspect new approaches to the design of novel catalytic systems. Energetic demands and associated costs to the production of renewable H_2 from additional sources represent the most notable limitations to the economically sustainable implementation of t-CO_2RR. The production of CO_2-neutral renewable fuels simultaneously demands the production of H_2 from a sustainable source, with H_2O, the most naturally abundant source of hydrogen that is inexpensive and readily available, being the ideal candidate. While thermochemical approaches have largely established the use of H_2 from alternative sources, photochemical and electrochemical approaches aspire to the *in situ* supply of hydrogen from water. However, the simultaneous activation of two very stable molecules in the synthesis of hydrocarbons reflects extensive energy consumption. Insufficient socio-economic driving forces and a clear lack of industrial commitment and investment incentives are additional drawbacks to the technological development of the CO_2RR.

Considering the use of renewable photovoltaic or wind-derived electricity, in the electrochemical reduction of CO_2 noteworthy breakthroughs have been achieved in recent years toward the enhancement of the formation of C_2H_4 at the expense of reduced CH_4 yields, combining lower overpotentials with increasingly high

Faradaic efficiencies. This effort toward highly selective C_2H_4 to CH_4 ratios further evades costly paraffin–olefin separation processes.[554] We have highlighted the significance of works carried out with Cu_2O-derived electrodes and the derived number of currently intertwined possible contributions to these findings, *e.g.* grain boundaries, subsurface oxygen species and surface roughness. The conversion of CO_2 to C_2–C_4 olefins is a major pursuit in clean energy research, further believed herein to unlock the desirable mechanistic pathways toward C–C bonding required for the production of long-chain hydrocarbons. In addition, the electrochemical production of valuable ethylene and *n*-propanol products is preferable toward CH_4 production, since these are in strong price competition with the abundant and cheap natural gas. To date, however, steps toward the envisioned commercialization still require practical reaction rates above 300 mA cm^{-2}, superior FE, and catalytic stability, which currently remains below the 50 h mark.

The solar-driven reutilization of CO_2 is ideal from an economic point of view and offers significant potential in scalability as compared to electro- and photoelectrocatalytic platforms. Although the state-of-the-art production of fuels or chemicals from CO_2 using solar energy is still far from a practical consideration, rich knowledge has been accumulated for understanding the key factors that determine the catalytic performances. Following analogous studies in H_2 technologies, the research on the photo-driven CO_2RR is wide and urgently requires unifying guidelines such as mechanistic details and enhanced material characterization. The need for better quantification, *i.e.* CH_4 formation rates and solar-to-fuel efficiencies, toward the possible comparison of current advances is desirable. To date, such alternative approaches in the CO_2RR to high-energy-content fuels remain rather primary and face major drawbacks, with reported catalysts failing to yield adequate conversion efficiencies or produce long-chain products. Research on both the photo- and electro-driven reduction of CO_2, currently based on traditional trial and error approaches, would largely benefit from investments in experimental *in situ* and *operando* techniques and model systems, complemented with theoretical efforts to unveil performance descriptors in the rational design of new catalytic systems. Equally, in both fields, efforts are expected in the development of suitable reactors and operating conditions, reflecting a parallelism with water splitting technologies to serve as a major guideline in these research fields.

Conflicts of interest

There are no conflicts to declare.

Acknowledgements

This work was supported by the Korea Research Fellowship Program through the National Research Foundation of Korea (NRF) funded by the Ministry of Science and ICT (2017H1D3A1A02054206), and the mid-career researcher program (2017R1A2A1A05022387).

Notes and references

1 M. Sudiro and A. Bertucco, *Energy*, 2009, **34**, 2206.
2 M. Sudiro, A. Bertucco, F. Rugger and M. Fontana, *Energy Fuels*, 2008, **22**, 3894.
3 C. Knocke and J. Vogt, *Eng. Life Sci.*, 2009, **9**, 96.
4 P. J. le, B. Williams and L. M. L. Laurens, *Energy Environ. Sci.*, 2009, **3**, 554.
5 S. Chu, Y. Cui and N. Liu, *Nat. Mater.*, 2017, **16**, 16.
6 BP, *BP Statistical Review of World Energy June 2015*, 2015.
7 T. R. Karl and K. E. Trenberth, *Science*, 2003, **302**, 1719.
8 IPCC 2014, *Climate Change 2014: Mitigation of Climate Change*, Cambridge University Press, UK and New York, NY, USA, 2014.
9 S. Chu and A. Majumdar, *Nature*, 2012, **488**, 294.
10 D. Roemmich, J. Church, J. Gilson, D. Monselesan, P. Sutton and S. Wijffels, *Nat. Clim. Change*, 2015, **5**, 240.
11 A. Bernstein, E. H. Sargent, A. Aspuru-Guzik, R. Cogdell, G. R. Fleming, R. Van Grondelle and M. Molina, *Nature*, 2016, **538**, 30.
12 IEA, *World Energy Investment Outlook 2014 Factsheet*, 2014.
13 D. Y. C. Leung, G. Caramanna and M. M. Maroto-Valer, *Renewable Sustainable Energy Rev.*, 2014, **39**, 426.
14 W. M. Budzianowski, *Energy efficient solvents for CO_2* capture by gas-liquid absorption, Springer, 2017, pp. 1–11.
15 G. Centi, E. A. Quadrelli and S. Perathoner, *Energy Environ. Sci.*, 2013, **6**, 1711.
16 J. Liu, P. K. Thallapally, B. P. McGrail, D. R. Brown and J. Liu, *Chem. Soc. Rev.*, 2012, **41**, 2308.
17 N. Mac Dowell, P. S. Fennell, N. Shah and G. C. Maitland, *Nat. Clim. Change*, 2017, **7**, 243.
18 IEA, *Energy Technology Perspectives 2012—How to Secure a Clean Energy Future*, 2012.
19 B. I. McNeil, R. J. Matear, R. M. Key, J. L. Bullister and J. L. Sarmiento, *Science*, 2003, **299**, 235.
20 T. Coffey, D. R. Hardy, G. E. Besenbruch, K. R. Schultz, L. C. Brown and J. P. Dahlburg, *Def. Horiz.*, 2003, **36**, 1.
21 R. W. Dorner, D. R. Hardy, F. W. Williams and H. D. Willauer, *Energy Environ. Sci.*, 2010, **3**, 884.
22 H. Kolbe and E. Lautemann, *Justus Liebigs Ann. Chem.*, 1869, **113**, 125.
23 E. Solvay, *US Pat.*, 263981 A, 1882.
24 B. Carl and M. Wilhelm, *US Pat.*, 1429483 A, 1922.
25 Z. Xie, X. Zhang, Z. Zhang and Z. Zhou, *Adv. Mater.*, 2017, **29**, 1605891.
26 S. Yang, Y. Qiao, P. He, Y. Liu, Z. Cheng, J. Zhu and H. Zhou, *Energy Environ. Sci.*, 2017, **10**, 972.
27 Y. Qiao, J. Yi, S. Wu, Y. Liu, S. Yang, P. He and H. Zhou, *Joule*, 2017, **1**, 359.
28 Z. Yang, X. Gao and Z. Liu, *Curr. Opin. Green Sustain. Chem.*, 2016, **1**, 13.
29 A. Goeppert, M. Czaun, J.-P. Jones, G. K. S. Prakash and G. A. Olah, *Chem. Soc. Rev.*, 2014, **43**, 7995.
30 S. Moret, P. J. Dyson and G. Laurenczy, *Nat. Commun.*, 2014, **5**, 4017.

31 J. Graciani, K. Mudiyanselage, F. Xu, A. E. Baber, J. Evans, S. D. Senanayake, D. J. Stacchiola, P. Liu, J. Hrbek, J. F. Sanz and J. A. Rodriguez, *Science*, 2014, **345**, 546.
32 W.-H. Wang, Y. Himeda, J. T. Muckerman, G. F. Manbeck and E. Fujita, *Chem. Rev.*, 2015, **115**, 12936.
33 J. Qiao, Y. Liu, F. Hong and J. Zhang, *Chem. Soc. Rev.*, 2014, **43**, 631.
34 M. Cokoja, C. Bruckmeier, B. Rieger, W. A. Herrmann and F. E. Kühn, *Angew. Chem., Int. Ed.*, 2011, **50**, 8510.
35 A. Álvarez, A. Bansode, A. Urakawa, A. V. Bavykina, T. A. Wezendonk, M. Makkee, J. Gascon and F. Kapteijn, *Chem. Rev.*, 2017, **117**, 9804.
36 M. Aresta, A. Dibenedetto and A. Angelini, *Chem. Rev.*, 2014, **114**, 1709.
37 S. Hernández, M. A. Farkhondehfal, F. Sastre, M. Makkee, G. Saracco and N. Russo, *Green Chem.*, 2017, **19**, 2326.
38 H. M. T. Galvis and K. P. de Jong, *ACS Catal.*, 2013, **3**, 2130.
39 S. Lewandowski, *4th Annual Asia Chemical Conference*, 2016.
40 J. M. Spurgeon and B. Kumar, *Energy Environ. Sci.*, 2018, **11**, 1536.
41 D. M. Weekes, D. A. Salvatore, A. Reyes, A. Huang and C. P. Berlinguette, *Acc. Chem. Res.*, 2018, **51**, 910.
42 U.S. Energy Information Administration: www.eia.gov.
43 H. Muroyama, Y. Tsuda, T. Asakoshi, H. Masitah, T. Okanishi, T. Matsui and K. Eguchi, *J. Catal.*, 2016, **343**, 178.
44 S. Kattel, P. Liu and J. G. Chen, *J. Am. Chem. Soc.*, 2017, **139**, 9739.
45 G. A. Mills and F. W. Steffgen, *Catal. Rev.: Sci. Eng.*, 1974, **8**, 159.
46 S. Eckle, H.-G. Anfang and R. J. Behm, *J. Phys. Chem. C*, 2011, **115**, 1361.
47 M. R. Prairie, A. Renken, J. G. Highfield, K. R. Thampi and M. Grätzel, *J. Catal.*, 1991, **129**, 130.
48 S.-J. Choe, H.-J. Kang, S.-J. Kim, S.-B. Park, D.-H. Park and D.-S. Huh, *Bull. Korean Chem. Soc.*, 2005, **26**, 1682.
49 A. Trovarelli, C. Mustazza, G. Dolcetti, J. Kaspar and M. Graziani, *Appl. Catal.*, 1990, **65**, 129.
50 C.-K. Kuei and M.-D. Lee, *Can. J. Chem. Eng.*, 1991, **69**, 347.
51 M. J. L. Ginés, A. J. Marchi and C. R. Apesteguía, *Appl. Catal., A*, 1997, **154**, 155.
52 J. L. Falconer and A. E. Zağli, *J. Catal.*, 1980, **62**, 280.
53 A. de Klerk, *Green Chem.*, 2008, **10**, 1249.
54 A. de Klerk, *Energy Environ. Sci.*, 2011, **4**, 1177.
55 A. Borgschulte, N. Gallandat, B. Probst, R. Suter, E. Callini, D. Ferri, Y. Arroyo, R. Erni, H. Geerlings and A. Züttel, *Phys. Chem. Chem. Phys.*, 2013, **15**, 9620.
56 R. A. Fiato, E. Iglesia, G. W. Rice and S. L. Soled, *Stud. Surf. Sci. Catal.*, 1998, **114**, 339.
57 S.-R. Yan, K.-W. Jun, J.-S. Hong, S.-B. Lee, M.-J. Choi and K.-W. Lee, *Korean J. Chem. Eng.*, 1999, **16**, 357.
58 T. Riedel, G. Schaub, K.-W. Jun and K.-W. Lee, *Ind. Eng. Chem. Res.*, 2001, **40**, 1355.
59 U. Rodemerck, M. Holena, E. Wagner, Q. Smejkal, A. Barkschat and M. Baerns, *ChemCatChem*, 2013, **5**, 1948.
60 G. D. Weatherbee and C. H. Bartholomew, *J. Catal.*, 1984, **87**, 352.
61 E. Iglesia, S. C. Reyes and R. J. Madon, *J. Catal.*, 1991, **129**, 238.
62 B. Zhao, Y.-X. Pan and C. Liu, *Catal. Today*, 2012, **194**, 60.
63 J. A. H. Dreyer, P. Li, L. Zhang, G. K. Beh, R. Zhang, P. H.-L. Sit and W. Y. Teoh, *Appl. Catal., B*, 2017, **219**, 715.
64 K. R. Thampi, J. Kiwi and M. Grätzel, *Nature*, 1987, **327**, 506.
65 X. Su, J. Xu, B. Liang, H. Duan, B. Hou and Y. Huang, *J. Energy Chem.*, 2016, **25**, 553.
66 P. J. Lunde and F. L. Kester, *Ind. Eng. Chem. Process Des. Dev.*, 1974, **13**, 27.
67 F. Masini, C. E. Strebel, D. N. McCarthy, A. U. F. Nierhoff, J. Kehres, E. M. Fiordaliso, J. H. Nielsen and I. Chorkendorff, *J. Catal.*, 2013, **308**, 282.
68 N. M. Gupta, V. S. Kamble, V. B. Kartha, R. M. Iyer, K. Ravindranathan Thampi and M. Grätzel, *J. Catal.*, 1994, **146**, 173.
69 G. D. Weatherbee and C. H. Bartholomew, *J. Catal.*, 1981, **68**, 67.
70 S. Sharma, Z. Hu, P. Zhang, E. W. McFarland and H. Metiu, *J. Catal.*, 2011, **278**, 297.
71 S. Takenaka, T. Shimizu and K. Otsuka, *Int. J. Hydrogen Energy*, 2014, **29**, 1065.
72 P. Panagiotopoulou, *Appl. Catal., A*, 2017, **542**, 63.
73 T. Abe, M. Tanizawa, K. Watanabe and A. Taguchi, *Energy Environ. Sci.*, 2009, **2**, 315.
74 Q. Lin, X. Y. Liu, Y. Jiang, Y. Wang, Y. Huang and T. Zhang, *Catal. Sci. Technol.*, 2014, **4**, 2058.
75 A. Kim, C. Sanchez, G. Patriarche, O. Ersen, S. Moldovan, A. Wisnet, C. Sassoye and D. P. Debecker, *Catal. Sci. Technol.*, 2016, **6**, 8117.
76 A. Kim, D. P. Debecker, F. Devred, V. Dubois, C. Sanchez and C. Sassoye, *Appl. Catal., B*, 2018, **220**, 615.
77 Y. Guo, S. Mei, K. Yuan, D.-J. Wang, H.-C. Liu, C.-H. Yan and Y.-W. Zhang, *ACS Catal.*, 2018, **8**, 6203.
78 F. Solymosi, I. Tombácz and J. Koszta, *J. Catal.*, 1985, **95**, 578.
79 Z. Zhang, A. Kladi and X. E. Verykios, *J. Catal.*, 1994, **148**, 737.
80 C. Deleitenburg and A. Trovarelli, *J. Catal.*, 1995, **156**, 171.
81 S. Ma, W. Song, B. Liu, H. Zheng, J. Deng, W. Zhong, J. Liu, X.-Q. Gong and Z. Zhao, *Catal. Sci. Technol.*, 2016, **6**, 6128.
82 A. Karelovic and P. Ruiz, *Appl. Catal., B*, 2012, **113–114**, 237.
83 A. Karelovic and P. Ruiz, *J. Catal.*, 2013, **301**, 141.
84 P. Panagiotopoulou, D. I. Kondarides and X. E. Verykios, *Appl. Catal., A*, 2008, **344**, 45.
85 M. A. Vannice and R. L. Garten, *Ind. Eng. Chem. Process Des. Dev.*, 1979, **18**, 186.
86 J. Martins, N. Batail, S. Silva, S. Rafik-Clement, A. Karelovic, D. P. Debecker, A. Chaumonnot and D. Uzio, *Catal. Commun.*, 2015, **58**, 11.
87 J.-N. Park and E. W. McFarland, *J. Catal.*, 2009, **266**, 92.
88 H. Y. Kim, H. M. Lee and J.-N. Park, *J. Phys. Chem. C*, 2010, **114**, 7128.

89 F.-W. Chang, M.-T. Tsay and S.-P. Liang, *Appl. Catal., A*, 2001, **209**, 217.
90 F.-W. Chang, M.-S. Kuo, M.-T. Tsay and M.-C. Hsieh, *Appl. Catal., A*, 2003, **247**, 309.
91 S. Rahmani, M. Rezaei and F. Meshkani, *J. Ind. Eng. Chem.*, 2014, **20**, 1346.
92 A. Aljishi, G. Veilleux, J. A. H. Lalinde and J. Kopyscinski, *Appl. Catal., A*, 2018, **549**, 263.
93 J.-K. Lee, B.-I. An, D. Kim, S.-H. Min, J.-S. Jung and S.-H. Lee, *Bull. Korean Chem. Soc.*, 2007, **28**, 121.
94 G. Du, S. Lim, Y. Yang, C. Wang, L. Pfefferle and G. L. Haller, *J. Catal.*, 2007, **249**, 370.
95 M. A. A. Aziz, A. A. Jalil, S. Triwahyono, R. R. Mukti, Y. H. Taufiq-Yap and M. R. Sazegar, *Appl. Catal., B*, 2014, **147**, 359.
96 C.-S. Chen, C. S. Budi, H.-C. Wu, D. Saikia and H.-M. Kao, *ACS Catal.*, 2017, **7**, 8367.
97 W. Zhen, B. Li, G. Lu and J. Ma, *Chem. Commun.*, 2015, **51**, 1728.
98 M. Cai, J. Wen, W. Chu, X. Cheng and Z. Li, *J. Nat. Gas Chem.*, 2011, **20**, 318.
99 G. Zhou, H. Liu, K. Cui, A. Jia, G. Hu, Z. Jiao, Y. Liu and X. Zhang, *Appl. Surf. Sci.*, 2016, **383**, 248.
100 S. Tada, T. Shimizu, H. Kameyama, T. Haneda and R. Kikuchi, *Int. J. Hydrogen Energy*, 2012, **37**, 5527.
101 Z. Cheng, B. J. Sherman and C. S. Lo, *J. Chem. Phys.*, 2013, **138**, 14702.
102 G. Zhou, H. Liu, K. Cui, H. Xie, Z. Jiao, G. Zhang, K. Xiong and X. Zheng, *Int. J. Hydrogen Energy*, 2017, **42**, 16108.
103 L. Atzori, M. G. Cutrufello, D. Meloni, R. Monaci, C. Cannas, D. Gazzoli, M. F. Sini, P. Deiana and E. Rombi, *Int. J. Hydrogen Energy*, 2017, **42**, 32.
104 L. Atzori, M. G. Cutrufello, D. Meloni, C. Cannas, D. Gazzoli, R. Monaci, M. F. Sini and E. Rombi, *Catal. Today*, 2018, **299**, 183.
105 M. Guo and G. Lu, *Catal. Commun.*, 2014, **54**, 55.
106 B. Mutz, H. W. P. Carvalho, S. Mangold, W. Kleist and J.-D. Grunwaldt, *J. Catal.*, 2015, **327**, 48.
107 L. Xu, F. Wang, M. Chen, H. Yang, D. Nie, L. Qi and X. Lian, *RSC Adv.*, 2017, **7**, 18199.
108 A. L. Kustov, A. M. Frey, K. E. Larsen, T. Johannessen, J. K. Nørskov and C. H. Christensen, *Appl. Catal., A*, 2007, **320**, 98.
109 D. Tian, Z. Liu, D. Li, H. Shi, W. Pan and Y. Cheng, *Fuel*, 2013, **104**, 224.
110 S. Hwang, J. Lee, U. G. Hong, J. C. Jung, D. J. Koh, H. Lim, C. Byun and I. K. Song, *J. Ind. Eng. Chem.*, 2012, **18**, 243.
111 K. Ray and G. Deo, *Appl. Catal., B*, 2017, **218**, 525.
112 R. W. Dorner, D. R. Hardy, F. W. Williams, B. H. Davis and H. D. Willauer, *Energy Fuels*, 2009, **23**, 4190.
113 H. Schulz, E. van Steen and M. Claeys, *Top. Catal.*, 1995, **2**, 223.
114 J. Patzlaff, Y. Liu, C. Graffmann and J. Gaube, *Appl. Catal., A*, 1999, **186**, 109.
115 T. Riedel, M. Claeys, H. Schulz, G. Schaub, S.-S. Nam, K.-W. Jun, M.-J. Choi, G. Kishan and K.-W. Lee, *Appl. Catal., A*, 1999, **186**, 201.
116 C. G. Visconti, L. Lietti, E. Tronconi, P. Forzatti, R. Zennaro and E. Finocchio, *Appl. Catal., A*, 2009, **355**, 61.
117 F. Tihay, A. C. Roger, G. Pourroy and A. Kiennemann, *Energy Fuels*, 2002, **16**, 1271.
118 R. Satthawong, N. Koizumi, C. Song and P. Prasassarakich, *J. CO2 Util.*, 2013, **3–4**, 102.
119 J. Lahtinen, T. Anraku and G. A. Somorjai, *Catal. Lett.*, 1994, **25**, 241.
120 M. Voß, G. Fröhlich, D. Borgmann and G. Wedler, *J. Catal.*, 1999, **187**, 348.
121 W. Li, X. Nie, X. Jiang, A. Zhang, F. Ding, M. Liu, Z. Liu, X. Guo and C. Song, *Appl. Catal., B*, 2018, **220**, 397.
122 W. Li, A. Zhang, X. Jiang, C. Chen, Z. Liu, C. Song and X. Guo, *ACS Sustainable Chem. Eng.*, 2017, **5**, 7824.
123 G. Melaet, W. T. Ralston, C.-S. Li, S. Alayoglu, K. An, N. Musselwhite, B. Kalkan and G. A. Somorjai, *J. Am. Chem. Soc.*, 2014, **136**, 2260.
124 V. Iablokov, S. K. Beaumont, S. Alayoglu, V. V. Pushkarev, C. Specht, J. Gao, A. P. Alivisatos, N. Kruse and G. A. Somorjai, *Nano Lett.*, 2012, **12**, 3091.
125 R. Razzaq, C. Li, M. Usman, K. Suzuki and S. Zhang, *Chem. Eng. J.*, 2015, **262**, 1090.
126 F. Diehl and A. Y. Khodakov, *Oil Gas Sci. Technol.*, 2009, **64**, 11.
127 T. N. Phaahlamohlaka, D. O. Kumi, M. W. Dlamini, R. Forbes, L. L. Jewell, D. G. Billing and N. J. Coville, *ACS Catal.*, 2017, **7**, 1568.
128 S. K. Beaumont, S. Alayoglu, C. Specht, W. D. Michalak, V. V. Pushkarev, J. Guo, N. Kruse and G. A. Somorjai, *J. Am. Chem. Soc.*, 2014, **136**, 9898.
129 S. K. Beaumont, S. Alayoglu, C. Specht, N. Kruse and G. A. Somorjai, *Nano Lett.*, 2014, **14**, 4792.
130 S. Alayoglu, S. K. Beaumont, F. Zheng, V. V. Pushkarev, H. Zheng, V. Iablokov, Z. Liu, J. Guo, N. Kruse and G. A. Somorjai, *Top. Catal.*, 2011, **54**, 778.
131 H. H. Shin, L. Lu, Z. Yang, C. J. Kiely and S. McIntosh, *ACS Catal.*, 2016, **6**, 2811.
132 M. Schubert, S. Pokhrel, A. Thomé, V. Zielasek, T. M. Gesing, F. Roessner, M. Lutz and M. Bäumer, *Catal. Sci. Technol.*, 2016, **6**, 7449.
133 A. Karelovic and P. Ruiz, *ACS Catal.*, 2013, **3**, 2799.
134 C. Swalus, M. Jacquemin, C. Poleunis, P. Bertrand and P. Ruiz, *Appl. Catal., B*, 2012, **125**, 41.
135 C. Xie, C. Chen, Y. Yu, J. Su, Y. Li, G. A. Somorjai and P. Yang, *Nano Lett.*, 2017, **17**, 3798.
136 K. Cheng, M. Virginie, V. V. Ordomsky, C. Cordier, P. A. Chernavskii, M. I. Ivantsov, S. Paul, Y. Wang and A. Y. Khodakov, *J. Catal.*, 2015, **328**, 139.
137 H. Schulz, T. Riedel and G. Schaub, *Top. Catal.*, 2005, **32**, 117.
138 T. Riedel, H. Schulz, G. Schaub, K.-W. Jun, J.-S. Hwang and K.-W. Lee, *Top. Catal.*, 2003, **26**, 41.
139 N. Utsis, R. Vidruk-Nehemya, M. V. Landau and M. Herskowitz, *Faraday Discuss.*, 2016, **188**, 545.
140 C. Yang, H. Zhao, Y. Hou and D. Ma, *J. Am. Chem. Soc.*, 2012, **134**, 15814.

141 R. A. Fiato, S. L. Soled, G. W. Rice and S. Miseo, *US Pat.*, 5140049, 1992.
142 C. G. Visconti, M. Martinelli, L. Falbo, A. Infantes-Molina, L. Lietti, P. Forzatti, G. Iaquaniello, E. Palo, B. Picutti and F. Brignoli, *Appl. Catal., B*, 2017, **200**, 530.
143 T. Xie, J. Wang, F. Ding, A. Zhang, W. Li, X. Guo and C. Song, *J. CO2 Util.*, 2017, **19**, 202.
144 M. Albrecht, U. Rodemerck, M. Schneider, M. Bröring, D. Baabe and E. V. Kondratenko, *Appl. Catal., B*, 2017, **204**, 119.
145 N. G. Gallegos, A. M. Alvarez, M. V. Cagnoli, J. F. Bengoa, S. G. Marchetti, R. C. Mercader and A. A. Yeramian, *J. Catal.*, 1996, **161**, 132.
146 G. Kishan, M.-W. Lee, S.-S. Nam, M.-J. Choi and K.-W. Lee, *Catal. Lett.*, 1998, **56**, 215.
147 L. Torrente-Murciano, R. S. L. Chapman, A. Narvaez-Dinamarca, D. Mattia and M. D. Jones, *Phys. Chem. Chem. Phys.*, 2016, **18**, 15496.
148 M. C. Bahome, L. L. Jewell, D. Hildebrandt, D. Glasser and N. J. Coville, *Appl. Catal., A*, 2005, **287**, 60.
149 P. Serp and E. Castillejos, *ChemCatChem*, 2010, **2**, 41.
150 H. M. T. Galvis, J. H. Bitter, C. B. Khare, M. Ruitenbeek, A. I. Dugulan and K. P. de Jong, *Science*, 2012, **335**, 835.
151 D. Mattia, M. D. Jones, J. P. O'Byrne, O. G. Griffiths, R. E. Owen, E. Sackville, M. McManus and P. Plucinski, *ChemSusChem*, 2015, **8**, 4064.
152 D. R. Minett, J. P. O'Byrne, S. I. Pascu, P. K. Plucinski, R. E. Owen, M. D. Jones and D. Mattia, *Catal. Sci. Technol.*, 2014, **4**, 3351.
153 P. H. Choi, K.-W. Jun, S.-J. Lee, M.-J. Choi and K.-W. Lee, *Catal. Lett.*, 1996, **40**, 115.
154 M.-J. Choi, J.-S. Kim, H.-K. Kim, S.-B. Lee, Y. Kang and K.-W. Lee, *Korean J. Chem. Eng.*, 2001, **18**, 646.
155 R. W. Dorner, D. R. Hardy, F. W. Williams and H. D. Willauer, *Appl. Catal., A*, 2010, **373**, 112.
156 L. Xu, Q. Wang, D. Liang, X. Wang, L. Lin, W. Cui and Y. Xu, *Appl. Catal., A*, 1998, **173**, 19.
157 M. Amoyal, R. Vidruk-Nehemya, M. V. Landau and M. Herskowitz, *J. Catal.*, 2017, **348**, 29.
158 T. Numpilai, T. Witoon, N. Chanlek, W. Limphirat, G. Bonura, M. Chareonpanich and J. Limtrakul, *Appl. Catal., A*, 2017, **547**, 219.
159 S.-R. Yan, K.-W. Jun, J.-S. Hong, M.-J. Choi and K.-W. Lee, *Appl. Catal., A*, 2000, **194–195**, 63.
160 T. Li, Y. Yang, C. Zhang, X. An, H. Wan, Z. Tao, H. Xiang, Y. Li, F. Yi and B. Xu, *Fuel*, 2007, **86**, 921.
161 M. Al-Dossary, A. A. Ismail, J. L. G. Fierro, H. Bouzid and S. A. Al-Sayari, *Appl. Catal., B*, 2015, **165**, 651.
162 S. Li, A. Li, S. Krishnamoorthy and E. Iglesia, *Catal. Lett.*, 2001, **77**, 197.
163 T. Herranz, S. Rojas, F. J. Pérez-Alonso, M. Ojeda, P. Terreros and J. L. G. Fierro, *Appl. Catal., A*, 2006, **311**, 66.
164 R. W. Dorner, D. R. Hardy, F. W. Williams and H. D. Willauer, *Catal. Commun.*, 2011, **15**, 88.
165 S.-C. Lee, J.-H. Jang, B.-Y. Lee, J.-S. Kim, M. Kang, S.-B. Lee, M.-J. Choi and S.-J. Choung, *J. Mol. Catal. A: Chem.*, 2004, **210**, 131.
166 A. Erdöhelyi, M. Pásztor and F. Solymosi, *J. Catal.*, 1986, **98**, 166.
167 F. Solymosi, A. Erdöhelyi and T. Bánsági, *J. Catal.*, 1981, **68**, 371.
168 M. A. Henderson and S. D. Worley, *J. Phys. Chem.*, 1985, **89**, 1417.
169 E. Jwa, S. B. Lee, H. W. Lee and Y. S. Mok, *Fuel Process. Technol.*, 2013, **108**, 89.
170 M. Yamasaki, H. Habazaki, K. Asami, K. Izumiya and K. Hashimoto, *Catal. Commun.*, 2006, **7**, 24.
171 C. de Leitenburg, A. Trovarelli and J. Kaspar, *J. Catal.*, 1997, **166**, 98.
172 H. Song, J. Yang, J. Zhao and L. Chou, *Chin. J. Catal.*, 2010, **31**, 21.
173 N. Takezawa, H. Terunuma, M. Shimokawabe and H. Kobayashib, *Appl. Catal.*, 1986, **23**, 291.
174 A. M. Abdel-Mageed, D. Widmann, S. E. Olesen, I. Chorkendorff, J. Biskupek and R. J. Behm, *ACS Catal.*, 2015, **5**, 6753.
175 S. J. Tauster, S. C. Fung and R. L. Garten, *J. Am. Chem. Soc.*, 1978, **100**, 170.
176 C. K. Vance and C. H. Bartholomew, *Appl. Catal.*, 1983, **7**, 169.
177 J. Xu, X. Su, H. Duan, B. Hou, Q. Lin, X. Liu, X. Pan, G. Pei, H. Geng, Y. Huang and T. Zhang, *J. Catal.*, 2016, **333**, 227.
178 F. Wang, S. He, H. Chen, B. Wang, L. Zheng, M. Wei, D. G. Evans and X. Duan, *J. Am. Chem. Soc.*, 2016, **138**, 6298.
179 S. Tada, O. J. Ochieng, R. Kikuchi, T. Haneda and H. Kameyama, *Int. J. Hydrogen Energy*, 2014, **39**, 10090.
180 Q. Sun, J. Ye, C. Liu and Q. Ge, *Greenhouse Gases: Sci. Technol.*, 2014, **4**, 140.
181 M. D. Porosoff, X. Yang, J. A. Boscoboinik and J. G. Chen, *Angew. Chem., Int. Ed.*, 2014, **53**, 6705.
182 J. Wu, C. Wen, X. Zou, J. Jimenez, J. Sun, Y. Xia, M.-T. Fonseca Rodrigues, S. Vinod, J. Zhong, N. Chopra, I. N. Odeh, G. Ding, J. Lauterbach and P. M. Ajayan, *ACS Catal.*, 2017, **7**, 4497.
183 T. Inui, H. Hara, T. Takeguchi, K. Ichino, J. B. Kim, S. Iwamoto and S. B. Pu, *Energy Convers. Manage.*, 1997, **38**, S385.
184 O. Martin and J. Pérez-Ramírez, *Catal. Sci. Technol.*, 2013, **3**, 3343.
185 U. Olsbye, S. Svelle, K. P. Lillerud, Z. H. Wei, Y. Y. Chen, J. F. Li, J. G. Wang and W. B. Fan, *Chem. Soc. Rev.*, 2015, **44**, 7155.
186 S. Kuld, M. Thorhauge, H. Falsig, C. F. Elkjær, S. Helveg, I. Chorkendorff and J. Sehested, *Science*, 2016, **352**, 969.
187 B. Rungtaweevoranit, J. Baek, J. R. Araujo, B. S. Archanjo, K. M. Choi, O. M. Yaghi and G. A. Somorjai, *Nano Lett.*, 2016, **16**, 7645.
188 S. Kattel, P. J. Ramírez, J. G. Chen, J. A. Rodriguez and P. Liu, *Science*, 2017, **355**, 1296.
189 B. An, J. Zhang, K. Cheng, P. Ji, C. Wang and W. Lin, *J. Am. Chem. Soc.*, 2017, **139**, 3834.
190 M. Behrens, S. Zander, P. Kurr, N. Jacobsen, J. Senker, G. Koch, T. Ressler, R. W. Fischer and R. Schlögl, *J. Am. Chem. Soc.*, 2013, **135**, 6061.

191 P. Gao, F. Li, H. Zhan, N. Zhao, F. Xiao, W. Wei, L. Zhong, H. Wang and Y. Sun, *J. Catal.*, 2013, **298**, 51.
192 U. Olsbye, S. Svelle, M. Bjørgen, P. Beato, T. V. W. Janssens, F. Joensen, S. Bordiga and K. P. Lillerud, *Angew. Chem., Int. Ed.*, 2012, **51**, 5810.
193 T. Liang, J. Chen, Z. Qin, J. Li, P. Wang, S. Wang, G. Wang, M. Dong, W. Fan and J. Wang, *ACS Catal.*, 2016, **6**, 7311.
194 Y. Wang, S.-L. Chen, Y.-L. Gao, Y.-Q. Cao, Q. Zhang, W.-K. Chang and J. B. Benziger, *ACS Catal.*, 2017, **7**, 5572.
195 Y. Tan, M. Fujiwara, H. Ando, Q. Xu and Y. Souma, *Ind. Eng. Chem. Res.*, 1999, **38**, 3225.
196 F. Jiao, J. Li, X. Pan, J. Xiao, H. Li, H. Ma, M. Wei, Y. Pan, Z. Zhou, M. Li, S. Miao, J. Li, Y. Zhu, D. Xiao, T. He, J. Yang, F. Qi, Q. Fu and X. Bao, *Science*, 2016, **351**, 1065.
197 L. Zhong, F. Yu, Y. An, Y. Zhao, Y. Sun, Z. Li, T. Lin, Y. Lin, X. Qi, Y. Dai, L. Gu, J. Hu, S. Jin, Q. Shen and H. Wang, *Nature*, 2016, **538**, 84.
198 Z. Li, J. Wang, Y. Qu, H. Liu, C. Tang, S. Miao, Z. Feng, H. An and C. Li, *ACS Catal.*, 2017, **7**, 8544.
199 P. Gao, S. Li, X. Bu, S. Dang, Z. Liu, H. Wang, L. Zhong, M. Qiu, C. Yang, J. Cai, W. Wei and Y. Sun, *Nat. Chem.*, 2017, **9**, 1019.
200 R. A. Dalla Betta, A. G. Piken and M. Shelef, *J. Catal.*, 1975, **40**, 173.
201 T. Szailer, É. Novák, A. Oszkó and A. Erdőhelyi, *Top. Catal.*, 2007, **46**, 79.
202 R. Ryoo, K. Cho and F. Marques Mota, in *Zeolites in Sustainable Chemistry: Synthesis, Characterization and Catalytic Applications*, ed. F.-S. Xiao and X. Meng, 2015, pp. 101–148.
203 J. Martins, N. Batail, S. Silva, S. Rafik-Clement, A. Chaumonnot, D. Uzio, T. S. Nguyen and L. Piccolo, *Appl. Catal., A*, 2015, **504**, 504.
204 F. Goodarzi, L. Kang, F. R. Wang, F. Joensen, S. Kegnæs and J. Mielby, *ChemCatChem*, 2018, **10**, 1566.
205 Y. Li, G. Lu and J. Ma, *RSC Adv.*, 2014, **4**, 17420.
206 W. Zhen, F. Gao, B. Tian, P. Ding, Y. Deng, Z. Li, H. Gao and G. Lu, *J. Catal.*, 2017, **348**, 200.
207 C. Janke, M. S. Duyar, M. Hoskins and R. Farrauto, *Appl. Catal., B*, 2014, **152–153**, 184.
208 M. Agnelli, M. Kolb and C. Mirodatos, *J. Catal.*, 1994, **148**, 9.
209 F. Ocampo, B. Louis and A.-C. Roger, *Appl. Catal., A*, 2009, **369**, 90.
210 S. He, C. Li, H. Chen, D. Su, B. Zhang, X. Cao, B. Wang, M. Wei, D. G. Evans and X. Duan, *Chem. Mater.*, 2013, **25**, 1040.
211 R. Satthawong, N. Koizumi, C. Song and P. Prasassarakich, *Catal. Today*, 2015, **251**, 34.
212 H. D. Willauer, R. Ananth, M. T. Olsen, D. M. Drab, D. R. Hardy and F. W. Williams, *J. CO2 Util.*, 2013, **3–4**, 56.
213 M. P. Rohde, D. Unruh and G. Schaub, *Ind. Eng. Chem. Res.*, 2005, **44**, 9653.
214 S.-C. Lee, J.-S. Kim, W. C. Shin, M.-J. Choi and S.-J. Choung, *J. Mol. Catal. A: Chem.*, 2009, **301**, 98.
215 D. Sun, F. M. Khan and D. S. A. Simakov, *Chem. Eng. J.*, 2017, **329**, 165.
216 M. E. Dry, *Catal. Today*, 2002, **71**, 227.
217 S. Rönsch, J. Schneider, S. Matthischke, M. Schlüter, M. Götz, J. Lefebvre, P. Prabhakaran and S. Bajohr, *Fuel*, 2016, **166**, 276.
218 S. T. Sie and R. Krishna, *Appl. Catal., A*, 1999, **186**, 55.
219 J.-S. Kim, S. Lee, S.-B. Lee, M.-J. Choi and K.-W. Lee, *Catal. Today*, 2006, **115**, 228.
220 D. B. Levin and R. Chahine, *Int. J. Hydrogen Energy*, 2010, **35**, 4962.
221 M. D. Porosoff, B. Yan and J. G. Chen, *Energy Environ. Sci.*, 2016, **9**, 62.
222 S. Saeidi, F. Fazlollahi, S. Najari, D. Iranshahi, J. J. Klemeš and L. L. Baxter, *J. Ind. Eng. Chem.*, 2017, **49**, 1.
223 J. Ren, S. Ouyang, H. Xu, X. Meng, T. Wang, D. Wang and J. Ye, *Adv. Energy Mater.*, 2017, **7**, 1601657.
224 F. Sastre, A. V. Puga, L. Liu, A. Corma and H. García, *J. Am. Chem. Soc.*, 2014, **136**, 6798.
225 N. M. Haegel, R. Margolis, T. Buonassisi, D. Feldman, A. Froitzheim, R. Garabedian, M. Green, S. Glunz, H.-M. Henning, B. Holder, I. Kaizuka, B. Kroposki, K. Matsubara, S. Niki, K. Sakurai, R. A. Schindler, W. Tumas, E. R. Weber, G. Wilson, M. Woodhouse and S. Kurtz, *Science*, 2017, **356**, 141.
226 D. T. Whipple and P. J. A. Kenis, *J. Phys. Chem. Lett.*, 2010, **1**, 3451.
227 K. W. Frese Jr. and S. Leach, *J. Electrochem. Soc.*, 1985, **132**, 259.
228 Y. Hori, K. Kikuchi and S. Suzuki, *Chem. Lett.*, 1985, 1695.
229 Y. Hori, K. Kikuchi, A. Murata and S. Suzuki, *Chem. Lett.*, 1986, 897.
230 G. O. Larrazábal, A. J. Martín and J. Pérez-Ramírez, *J. Phys. Chem. Lett.*, 2017, **8**, 3933.
231 S. Back, H. Kim and Y. Jung, *ACS Catal.*, 2015, **5**, 965.
232 K. P. Kuhl, E. R. Cave, D. N. Abram and T. F. Jaramillo, *Energy Environ. Sci.*, 2012, **5**, 7050.
233 F. Abild-Pedersen, J. Greeley, F. Studt, J. Rossmeisl, T. R. Munter, P. G. Moses, E. Skúlason, T. Bligaard and J. K. Nørskov, *Phys. Rev. Lett.*, 2007, **99**, 16105.
234 A. A. Peterson and J. K. Nørskov, *J. Phys. Chem. Lett.*, 2012, **3**, 251.
235 Y. Hori, A. Murata, R. Takahashi and S. Suzuki, *J. Am. Chem. Soc.*, 1987, **109**, 5022.
236 Y. Hori, A. Murata, R. Takahashi and S. Suzuki, *Chem. Lett.*, 1987, 1665.
237 Y. Hori, A. Murata, R. Takahashi and S. Suzuki, *J. Chem. Soc., Chem. Commun.*, 1988, 17.
238 Y. Hori, A. Murata and R. Takahashi, *J. Chem. Soc., Faraday Trans. 1*, 1989, **85**, 2309.
239 Y. Hori, A. Murata and Y. Yoshinami, *J. Chem. Soc., Faraday Trans.*, 1991, **87**, 125.
240 D. W. DeWulf, T. Jin and A. J. Bard, *J. Electrochem. Soc.*, 1989, **136**, 1686.
241 M. Gattrell, N. Gupta and A. Co, *J. Electroanal. Chem.*, 2006, **594**, 1.
242 R. L. Cook, R. C. MacDuff and A. F. Sammells, *J. Electrochem. Soc.*, 1989, **136**, 1982.

243 Y. Hori, in *Handbook of Fuel Cells – Fundamentals, Technology and Applications*, ed. W. Vielstich, H. A. Gasteiger and A. Lamm, John Wiley & Sons, Ltd, 2010.
244 Y. Hori, H. Wakebe, T. Tsukamoto and O. Koga, *Electrochim. Acta*, 1994, **39**, 1833.
245 K. P. Kuhl, T. Hatsukade, E. R. Cave, D. N. Abram, J. Kibsgaard and T. F. Jaramillo, *J. Am. Chem. Soc.*, 2014, **136**, 14107.
246 B. A. Rosen, A. Salehi-Khojin, M. R. Thorson, W. Zhu, D. T. Whipple, P. J. A. Kenis and R. I. Masel, *Science*, 2011, **334**, 643.
247 D. D. Zhu, J. L. Liu and S. Z. Qiao, *Adv. Mater.*, 2016, **28**, 3423.
248 E. V. Kondratenko, G. Mul, J. Baltrusaitis, G. O. Larrazábal and J. Pérez-Ramírez, *Energy Environ. Sci.*, 2013, **6**, 3112.
249 B. Kumar, M. Asadi, D. Pisasale, S. Sinha-Ray, B. A. Rosen, R. Haasch, J. Abiade, A. L. Yarin and A. Salehi-Khojin, *Nat. Commun.*, 2013, **4**, 2819.
250 S. Lin, C. S. Diercks, Y.-B. Zhang, N. Kornienko, E. M. Nichols, Y. Zhao, A. R. Paris, D. Kim, P. Yang, O. M. Yaghi and C. J. Chang, *Science*, 2015, **349**, 1208.
251 J. Wu, R. M. Yadav, M. Liu, P. P. Sharma, C. S. Tiwary, L. Ma, X. Zou, X.-D. Zhou, B. I. Yakobson, J. Lou and P. M. Ajayan, *ACS Nano*, 2015, **9**, 5364.
252 J. Wu, M. Liu, P. P. Sharma, R. M. Yadav, L. Ma, Y. Yang, X. Zou, X.-D. Zhou, R. Vajtai, B. I. Yakobson, J. Lou and P. M. Ajayan, *Nano Lett.*, 2016, **16**, 466.
253 M. Watanabe, M. Shibata, A. Katoh, M. Azuma and T. Sakata, *Denki Kagaku*, 1991, **59**, 508.
254 T. E. Teeter and P. Van Rysselberghe, *J. Chem. Phys.*, 1954, **22**, 759.
255 K. Ito, T. Murata and S. Ikeda, *Bull. Nagoya Inst. Technol.*, 1975, **27**, 209.
256 R. Kortlever, J. Shen, K. J. P. Schouten, F. Calle-Vallejo and M. T. M. Koper, *J. Phys. Chem. Lett.*, 2015, **6**, 4073.
257 W. Luo, X. Nie, M. J. Janik and A. Asthagiri, *ACS Catal.*, 2016, **6**, 219.
258 K. J. P. Schouten, Y. Kwon, C. J. M. van der Ham, Z. Qin and M. T. M. Koper, *Chem. Sci.*, 2011, **2**, 1902.
259 J. H. Montoya, C. Shi, K. Chan and J. K. Nørskov, *J. Phys. Chem. Lett.*, 2015, **6**, 2032.
260 A. A. Peterson, F. Abild-Pedersen, F. Studt, J. Rossmeisl and J. K. Nørskov, *Energy Environ. Sci.*, 2010, **3**, 1311.
261 Y. Hori, R. Takahashi, Y. Yoshinami and A. Murata, *J. Phys. Chem. B*, 1997, **101**, 7075.
262 K. J. P. Schouten, E. Pérez Gallent and M. T. M. Koper, *J. Electroanal. Chem.*, 2014, **716**, 53.
263 S. Yu, A. J. Wilson, G. Kumari, X. Zhang and P. K. Jain, *ACS Energy Lett.*, 2017, **2**, 2058.
264 W. J. Durand, A. A. Peterson, F. Studt, F. Abild-Pedersen and J. K. Nørskov, *Surf. Sci.*, 2011, **605**, 1354.
265 X. Nie, W. Luo, M. J. Janik and A. Asthagiri, *J. Catal.*, 2014, **312**, 108.
266 Y. Huang, A. D. Handoko, P. Hirunsit and B. S. Yeo, *ACS Catal.*, 2017, **7**, 1749.
267 R. B. Sandberg, J. H. Montoya, K. Chan and J. K. Nørskov, *Surf. Sci.*, 2016, **654**, 56.
268 R. Reske, M. Duca, M. Oezaslan, K. J. P. Schouten, M. T. M. Koper and P. Strasser, *J. Phys. Chem. Lett.*, 2013, **4**, 2410.
269 A. S. Varela, C. Schlaup, Z. P. Jovanov, P. Malacrida, S. Horch, I. E. L. Stephens and I. Chorkendorff, *J. Phys. Chem. C*, 2013, **117**, 20500.
270 D. Friebel, F. Mbuga, S. Rajasekaran, D. J. Miller, H. Ogasawara, R. Alonso-Mori, D. Sokaras, D. Nordlund, T.-C. Weng and A. Nilsson, *J. Phys. Chem. C*, 2014, **118**, 7954.
271 Y. Hori, I. Takahashi, O. Koga and N. Hoshi, *J. Mol. Catal. A: Chem.*, 2003, **199**, 39.
272 F. Calle-Vallejo and M. T. M. Koper, *Angew. Chem.*, 2013, **125**, 7423.
273 Y. Hori, I. Takahashi, O. Koga and N. Hoshi, *J. Phys. Chem. B*, 2002, **106**, 15.
274 F. S. Roberts, K. P. Kuhl and A. Nilsson, *Angew. Chem., Int. Ed.*, 2015, **54**, 5179.
275 A. Loiudice, P. Lobaccaro, E. A. Kamali, T. Thao, B. H. Huang, J. W. Ager and R. Buonsanti, *Angew. Chem., Int. Ed.*, 2016, **55**, 5789.
276 C. S. Chen, A. D. Handoko, J. H. Wan, L. Ma, D. Ren and B. S. Yeo, *Catal. Sci. Technol.*, 2015, **5**, 161.
277 K. Jiang, R. B. Sandberg, A. J. Akey, X. Liu, D. C. Bell, J. K. Nørskov, K. Chan and H. Wang, *Nat. Catal.*, 2018, **1**, 111.
278 J.-F. Xie, Y.-X. Huang, W.-W. Li, X.-N. Song, L. Xiong and H.-Q. Yu, *Electrochim. Acta*, 2014, **139**, 137.
279 R. Reske, H. Mistry, F. Behafarid, B. R. Cuenya and P. Strasser, *J. Am. Chem. Soc.*, 2014, **136**, 6978.
280 K. Manthiram, B. J. Beberwyck and A. P. Alivisatos, *J. Am. Chem. Soc.*, 2014, **136**, 13319.
281 W. Tang, A. A. Peterson, A. S. Varela, Z. P. Jovanov, L. Bech, W. J. Durand, S. Dahl, J. Nørskov and I. Chorkendorff, *Phys. Chem. Chem. Phys.*, 2012, **14**, 76.
282 M. Le, M. Ren, Z. Zhang, P. T. Sprunger, R. L. Kurtz and J. C. Flake, *J. Electrochem. Soc.*, 2011, **158**, E45.
283 O. A. Baturina, Q. Lu, M. A. Padilla, L. Xin, W. Li, A. Serov, K. Artyushkova, P. Atanassov, F. Xu, A. Epshteyn, T. Brintlinger, M. Schuette and G. E. Collins, *ACS Catal.*, 2014, **4**, 3682.
284 Q. Li, W. Zhu, J. Fu, H. Zhang, G. Wu and S. Sun, *Nano Energy*, 2016, **24**, 1.
285 H. Mistry, F. Behafarid, R. Reske, A. S. Varela, P. Strasser and B. Roldan Cuenya, *ACS Catal.*, 2016, **6**, 1075.
286 D. Ren, N. T. Wong, A. D. Handoko, Y. Huang and B. S. Yeo, *J. Phys. Chem. Lett.*, 2016, **7**, 20.
287 D. Kim, C. S. Kley, Y. Li and P. Yang, *Proc. Natl. Acad. Sci. U. S. A.*, 2017, **114**, 10560.
288 M. Ma, K. Djanashvili and W. A. Smith, *Angew. Chem., Int. Ed.*, 2016, **55**, 6680.
289 Y. Li, F. Cui, M. B. Ross, D. Kim, Y. Sun and P. Yang, *Nano Lett.*, 2017, **17**, 1312.
290 M. N. Hossain, J. Wen and A. Chen, *Sci. Rep.*, 2017, **7**, 3184.

291 H. S. Jeon, S. Kunze, F. Scholten and B. Roldan Cuenya, *ACS Catal.*, 2018, **8**, 531.
292 A. Dutta, M. Rahaman, N. C. Luedi, M. Mohos and P. Broekmann, *ACS Catal.*, 2016, **6**, 3804.
293 S. Sen, D. Liu and G. T. R. Palmore, *ACS Catal.*, 2014, **4**, 3091.
294 K. D. Yang, W. R. Ko, J. H. Lee, S. J. Kim, H. Lee, M. H. Lee and K. T. Nam, *Angew. Chem., Int. Ed.*, 2017, **56**, 796.
295 Y.-G. Kim, J. H. Baricuatro, A. Javier, J. M. Gregoire and M. P. Soriaga, *Langmuir*, 2014, **30**, 15053.
296 C. M. Gunathunge, X. Li, J. Li, R. P. Hicks, V. J. Ovalle and M. M. Waegele, *J. Phys. Chem. C*, 2017, **121**, 12337.
297 Z. Han, R. Kortlever, H.-Y. Chen, J. C. Peters and T. Agapie, *ACS Cent. Sci.*, 2017, **3**, 853.
298 S. Gao, Y. Lin, X. Jiao, Y. Sun, Q. Luo, W. Zhang, D. Li, J. Yang and Y. Xie, *Nature*, 2016, **529**, 68.
299 K. W. Frese Jr., *J. Electrochem. Soc.*, 1991, **138**, 3338.
300 J. Xiao, A. Kuc, T. Frauenheim and T. Heine, *J. Mater. Chem. A*, 2014, **2**, 4885.
301 Y.-J. Zhang and A. A. Peterson, *Phys. Chem. Chem. Phys.*, 2015, **17**, 4505.
302 H. Shibata, J. A. Moulijn and G. Mul, *Catal. Lett.*, 2008, **123**, 186.
303 S. Lee and J. Lee, *ChemSusChem*, 2015, **9**, 333.
304 X. Nie, G. L. Griffin, M. J. Janik and A. Asthagiri, *Catal. Commun.*, 2014, **52**, 88.
305 C. W. Li and M. W. Kanan, *J. Am. Chem. Soc.*, 2012, **134**, 7231.
306 R. Kas, R. Kortlever, A. Milbrat, M. T. M. Koper, G. Mul and J. Baltrusaitis, *Phys. Chem. Chem. Phys.*, 2014, **16**, 12194.
307 D. Kim, S. Lee, J. D. Ocon, B. Jeong, J. K. Lee and J. Lee, *Phys. Chem. Chem. Phys.*, 2015, **17**, 824.
308 D. Ren, Y. Deng, A. D. Handoko, C. S. Chen, S. Malkhandi and B. S. Yeo, *ACS Catal.*, 2015, **5**, 2814.
309 H. Mistry, A. S. Varela, C. S. Bonifacio, I. Zegkinoglou, I. Sinev, Y.-W. Choi, K. Kisslinger, E. A. Stach, J. C. Yang, P. Strasser and B. Roldan Cuenya, *Nat. Commun.*, 2016, **7**, 12123.
310 A. Wuttig, M. Yaguchi, K. Motobayashi, M. Osawa and Y. Surendranath, *Proc. Natl. Acad. Sci. U. S. A.*, 2016, **113**, E4585.
311 A. S. Varela, M. Kroschel, T. Reier and P. Strasser, *Catal. Today*, 2016, **260**, 8.
312 E. L. Clark and A. T. Bell, *J. Am. Chem. Soc.*, 2018, **140**, 7012.
313 C. W. Li, J. Ciston and M. W. Kanan, *Nature*, 2014, **508**, 504.
314 A. Verdaguer-Casadevall, C. W. Li, T. P. Johansson, S. B. Scott, J. T. McKeown, M. Kumar, I. E. L. Stephens, M. W. Kanan and I. Chorkendorff, *J. Am. Chem. Soc.*, 2015, **137**, 9808.
315 X. Feng, K. Jiang, S. Fan and M. W. Kanan, *J. Am. Chem. Soc.*, 2015, **137**, 4606.
316 A. D. Handoko, C. W. Ong, Y. Huang, Z. G. Lee, L. Lin, G. B. Panetti and B. S. Yeo, *J. Phys. Chem. C*, 2016, **120**, 20058.
317 A. Engelbrecht, M. Hämmerle, R. Moos, M. Fleischer and G. Schmid, *Electrochim. Acta*, 2017, **224**, 642.
318 A. Eilert, F. Cavalca, F. S. Roberts, J. Osterwalder, C. Liu, M. Favaro, E. J. Crumlin, H. Ogasawara, D. Friebel, L. G. M. Pettersson and A. Nilsson, *J. Phys. Chem. Lett.*, 2017, **8**, 285.
319 C. Liu, M. P. Lourenço, S. Hedström, F. Cavalca, O. Diaz-Morales, H. A. Duarte, A. Nilsson and L. G. M. Pettersson, *J. Phys. Chem. C*, 2017, **121**, 25010.
320 P. De Luna, R. Quintero-Bermudez, C.-T. Dinh, M. B. Ross, O. S. Bushuyev, P. Todorovic, T. Regier, S. O. Kelley, P. Yang and E. H. Sargent, *Nat. Catal.*, 2018, **1**, 103.
321 Y. Zhou, F. Che, M. Liu, C. Zou, Z. Liang, P. De Luna, H. Yuan, J. Li, Z. Wang, H. Xie, H. Li, P. Chen, E. Bladt, R. Quintero-Bermudez, T.-K. Sham, S. Bals, J. Hofkens, D. Sinton, G. Chen and E. H. Sargent, *Nat. Chem.*, 2018, **10**, 974.
322 C. Reller, R. Krause, E. Volkova, B. Schmid, S. Neubauer, A. Rucki, M. Schuster and G. Schmid, *Adv. Energy Mater.*, 2017, **7**, 1602114.
323 D. Gao, I. Zegkinoglou, N. J. Divins, F. Scholten, I. Sinev, P. Grosse and B. R. Cuenya, *ACS Nano*, 2017, **11**, 4825.
324 A. Murata and Y. Hori, *Bull. Chem. Soc. Jpn.*, 1991, **64**, 123.
325 S. Lee, D. Kim and J. Lee, *Angew. Chem.*, 2015, **127**, 14914.
326 A. S. Varela, W. Ju, T. Reier and P. Strasser, *ACS Catal.*, 2016, **6**, 2136.
327 D. Kim, J. Resasco, Y. Yu, A. M. Asiri and P. Yang, *Nat. Commun.*, 2014, **5**, 4948.
328 M. Watanabe, M. Shibata, A. Katoh, T. Sakata and M. Azuma, *J. Electroanal. Chem. Interfacial Electrochem.*, 1991, **305**, 319.
329 J. He, K. E. Dettelbach, D. A. Salvatore, T. Li and C. P. Berlinguette, *Angew. Chem.*, 2017, **129**, 6164.
330 Z. P. Jovanov, H. A. Hansen, A. S. Varela, P. Malacrida, A. A. Peterson, J. K. Nørskov, I. E. L. Stephens and I. Chorkendorff, *J. Catal.*, 2016, **343**, 215.
331 Z. Yin, D. Gao, S. Yao, B. Zhao, F. Cai, L. Lin, P. Tang, P. Zhai, G. Wang, D. Ma and X. Bao, *Nano Energy*, 2016, **27**, 35.
332 M. Watanabe, M. Shibata, A. Katoh, M. Azuma and T. Sakata, *J. Electrochem. Soc.*, 1991, **138**, 3382.
333 P. Hirunsit, W. Soodsawang and J. Limtrakul, *J. Phys. Chem. C*, 2015, **119**, 8238.
334 X. Guo, Y. Zhang, C. Deng, X. Li, Y. Xue, Y.-M. Yan and K. Sun, *Chem. Commun.*, 2015, **51**, 1345.
335 W. Zhao, L. Yang, Y. Yin and M. Jin, *J. Mater. Chem. A*, 2014, **2**, 902.
336 F. Jia, X. Yu and L. Zhang, *J. Power Sources*, 2014, **252**, 85.
337 S. Ishimaru, R. Shiratsuchi and G. Nogami, *J. Electrochem. Soc.*, 2000, **147**, 1864.
338 J.-P. Grote, A. R. Zeradjanin, S. Cherevko, A. Savan, B. Breitbach, A. Ludwig and K. J. J. Mayrhofer, *J. Catal.*, 2016, **343**, 248.
339 D. A. Torelli, S. A. Francis, J. C. Crompton, A. Javier, J. R. Thompson, B. S. Brunschwig, M. P. Soriaga and N. S. Lewis, *ACS Catal.*, 2016, **6**, 2100.
340 R. Kortlever, I. Peters, C. Balemans, R. Kas, Y. Kwon, G. Mul and M. T. M. Koper, *Chem. Commun.*, 2016, **52**, 10229.

341 H. Zhang, G. Liu, L. Shi and J. Ye, *Adv. Energy Mater.*, 2018, **8**, 1701343.
342 C. S. Chen, J. H. Wan and B. S. Yeo, *J. Phys. Chem. C*, 2015, **119**, 26875.
343 S. Y. Lee, H. Jung, N.-K. Kim, H.-S. Oh, B. K. Min and Y. J. Hwang, *J. Am. Chem. Soc.*, 2018, **140**, 8681.
344 X.-F. Li, Q.-K. Li, J. Cheng, L. Liu, Q. Yan, Y. Wu, X.-H. Zhang, Z.-Y. Wang, Q. Qiu and Y. Luo, *J. Am. Chem. Soc.*, 2016, **138**, 8706.
345 Y. Pan, R. Lin, Y. Chen, S. Liu, W. Zhu, X. Cao, W. Chen, K. Wu, W.-C. Cheong, Y. Wang, L. Zheng, J. Luo, Y. Lin, Y. Liu, C. Liu, J. Li, Q. Lu, X. Chen, D. Wang, Q. Peng, C. Chen and Y. Li, *J. Am. Chem. Soc.*, 2018, **140**, 4218.
346 H. Bin Yang, S.-F. Hung, S. Liu, K. Yuan, S. Miao, L. Zhang, X. Huang, H.-Y. Wang, W. Cai, R. Chen, J. Gao, X. Yang, W. Chen, Y. Huang, H. M. Chen, C. M. Li, T. Zhang and B. Liu, *Nat. Energy*, 2018, **3**, 140.
347 H. Fei, J. Dong, Y. Feng, C. S. Allen, C. Wan, B. Volosskiy, M. Li, Z. Zhao, Y. Wang, H. Sun, P. An, W. Chen, Z. Guo, C. Lee, D. Chen, I. Shakir, M. Liu, T. Hu, Y. Li, A. I. Kirkland, X. Duan and Y. Huang, *Nat. Catal.*, 2018, **1**, 63.
348 K. Jiang, S. Siahrostami, T. Zheng, Y. Hu, S. Hwang, E. Stavitski, Y. Peng, J. Dynes, M. Gangisetty, D. Su, K. Attenkofer and H. Wang, *Energy Environ. Sci.*, 2018, **11**, 893.
349 Y. Wang, Z. Chen, P. Han, Y. Du, Z. Gu, X. Xu and G. Zheng, *ACS Catal.*, 2018, **8**, 7113.
350 X. Wang, A. S. Varela, A. Bergmann, S. Kühl and P. Strasser, *ChemSusChem*, 2017, **10**, 4642.
351 Y. Lum and J. W. Ager, *Energy Environ. Sci.*, 2018, **11**, 2935.
352 V. R. Stamenkovic, B. Fowler, B. S. Mun, G. Wang, P. N. Ross, C. A. Lucas and N. M. Markovic, *Science*, 2007, **315**, 493.
353 F. Marques Mota, D. L. T. Nguyen, J.-E. Lee, H. Piao, J.-H. Choy, Y. J. Hwang and D. H. Kim, *ACS Catal.*, 2018, **8**, 4364.
354 E. E. Benson, C. P. Kubiak, A. J. Sathrum and J. M. Smieja, *Chem. Soc. Rev.*, 2009, **38**, 89.
355 Z. Weng, J. Jiang, Y. Wu, Z. Wu, X. Guo, K. L. Materna, W. Liu, V. S. Batista, G. W. Brudvig and H. Wang, *J. Am. Chem. Soc.*, 2016, **138**, 8076.
356 Z. Weng, Y. Wu, M. Wang, J. Jiang, K. Yang, S. Huo, X.-F. Wang, Q. Ma, G. W. Brudvig, V. S. Batista, Y. Liang, Z. Feng and H. Wang, *Nat. Commun.*, 2018, **9**, 415.
357 J. Wu, S. Ma, J. Sun, J. I. Gold, C. S. Tiwary, B. Kim, L. Zhu, N. Chopra, I. N. Odeh, R. Vajtai, A. Z. Yu, R. Luo, J. Lou, G. Ding, P. J. A. Kenis and P. M. Ajayan, *Nat. Commun.*, 2016, **7**, 13869.
358 X. Zou, M. Liu, J. Wu, P. M. Ajayan, J. Li, B. Liu and B. I. Yakobson, *ACS Catal.*, 2017, **7**, 6245.
359 W. Li, N. Fechler and T. J. Bandosz, *Appl. Catal., B*, 2018, **234**, 1.
360 A. J. Martín, G. O. Larrazábal and J. Pérez-Ramírez, *Green Chem.*, 2015, **17**, 5114.
361 S. Wasmus, E. Cattaneo and W. Vielstich, *Electrochim. Acta*, 1990, **35**, 771.
362 G. Kyriacou and A. Anagnostopoulos, *J. Electroanal. Chem.*, 1992, **328**, 233.
363 Y. Hori, H. Konishi, T. Futamura, A. Murata, O. Koga, H. Sakurai and K. Oguma, *Electrochim. Acta*, 2005, **50**, 5354.
364 A. Wuttig and Y. Surendranath, *ACS Catal.*, 2015, **5**, 4479.
365 R. Kas, R. Kortlever, H. Yilmaz, M. T. M. Koper and G. Mul, *ChemElectroChem*, 2014, **2**, 354.
366 B. Jermann and J. Augustynski, *Electrochim. Acta*, 1994, **39**, 1891.
367 Z. Weng, X. Zhang, Y. Wu, S. Huo, J. Jiang, W. Liu, G. He, Y. Liang and H. Wang, *Angew. Chem., Int. Ed.*, 2017, **56**, 13135.
368 H. Li and C. Oloman, *J. Appl. Electrochem.*, 2006, **36**, 1105.
369 B. Kim, S. Ma, H.-R. M. Jhong and P. J. A. Kenis, *Electrochim. Acta*, 2015, **166**, 271.
370 R. Kortlever, K. H. Tan, Y. Kwon and M. T. M. Koper, *J. Solid State Electrochem.*, 2013, **17**, 1843.
371 S. Kaneco, H. Katsumata, T. Suzuki and K. Ohta, *Energy Fuels*, 2006, **20**, 409.
372 S. Verma, X. Lu, S. Ma, R. I. Maseld and P. J. A. Kenis, *Phys. Chem. Chem. Phys.*, 2016, **18**, 7075.
373 N. Gupta, M. Gattrell and B. MacDougall, *J. Appl. Electrochem.*, 2006, **36**, 161.
374 M. Liu, Y. Pang, B. Zhang, P. De Luna, O. Voznyy, J. Xu, X. Zheng, C.-T. Dinh, F. Fan, C. Cao, F. P. Garcia de Arquer, T. Saberi Safaei, A. Mepham, A. Klinkova, E. Kumacheva, T. Filleter, D. Sinton, S. O. Kelley and E. H. Sargent, *Nature*, 2016, **527**, 382.
375 S. Ma, M. Sadakiyo, R. Luo, M. Heima, M. Yamauchi and P. J. A. Kenis, *J. Power Sources*, 2016, **301**, 219.
376 Y. C. Li, D. Zhou, Z. Yan, R. H. Gonçalves, D. A. Salvatore, C. P. Berlinguette and T. E. Mallouk, *ACS Energy Lett.*, 2016, **1**, 1149.
377 D. T. Whipple, E. C. Finke and P. J. A. Kenis, *Electrochem. Solid-State Lett.*, 2010, **13**, B109.
378 Y. Hori, A. Murata, K. Kikuchi and S. Suzuki, *J. Chem. Soc., Chem. Commun.*, 1987, **10**, 728.
379 W. Zhu, R. Michalsky, Ö. Metin, H. Lv, S. Guo, C. J. Wright, X. Sun, A. A. Peterson and S. Sun, *J. Am. Chem. Soc.*, 2013, **135**, 16833.
380 Q. Lu, J. Rosen, Y. Zhou, G. S. Hutchings, Y. C. Kimmel, J. G. Chen and F. Jiao, *Nat. Commun.*, 2014, **5**, 3242.
381 T. Saberi Safaei, A. Mepham, X. Zheng, Y. Pang, C.-T. Dinh, M. Liu, D. Sinton, S. O. Kelley and E. H. Sargent, *Nano Lett.*, 2016, **16**, 7224.
382 D. Kopljar, A. Inan, P. Vindayer, N. Wagner and E. Klemm, *J. Appl. Electrochem.*, 2014, **44**, 1107.
383 S. Cheng, D. Xing, D. F. Call and B. E. Logan, *Environ. Sci. Technol.*, 2009, **43**, 3953.
384 M. C. A. A. Van Eerten-Jansen, A. Ter Heijne, C. J. N. Buisman and H. V. M. Hamelers, *Int. J. Energy Res.*, 2012, **36**, 809.
385 T. Mogi, T. Ishii, K. Hashimoto and R. Nakamura, *Chem. Commun.*, 2013, **49**, 3967.

386 A. H. Wonders, T. H. M. Housmans, V. Rosca and M. T. M. Koper, *J. Appl. Electrochem.*, 2006, **36**, 1215.
387 E. L. Clark, M. R. Singh, Y. Kwon and A. T. Bell, *Anal. Chem.*, 2015, **87**, 8013.
388 M. G. Walter, E. L. Warren, J. R. McKone, S. W. Boettcher, Q. Mi, E. A. Santori and N. S. Lewis, *Chem. Rev.*, 2010, **110**, 6446.
389 K. S. Joya, Y. F. Joya, K. Ocakoglu and R. van de Krol, *Angew. Chem., Int. Ed.*, 2013, **52**, 10426.
390 A. Kudo and Y. Miseki, *Chem. Soc. Rev.*, 2009, **38**, 253.
391 T. Inoue, A. Fujishima, S. Konishi and K. Honda, *Nature*, 1979, **277**, 637.
392 M. Marszewski, S. Cao, J. Yu and M. Jaroniec, *Mater. Horiz.*, 2015, **2**, 261.
393 J. Zhang and Z. Wang, in *Nanomaterials for Photocatalytic Chemistry*, ed. Y. Sun, World Scientific, 2016, pp. 229–288.
394 Y. Kohno, T. Tanaka, T. Funabiki and S. Yoshida, *Chem. Commun.*, 1997, 841.
395 X. Chang, T. Wang and J. Gong, *Energy Environ. Sci.*, 2016, **9**, 2177.
396 K. Teramura, K. Hori, Y. Terao, Z. Huang, S. Iguchi, Z. Wang, H. Asakura, S. Hosokawa and T. Tanaka, *J. Phys. Chem. C*, 2017, **121**, 8711.
397 W.-N. Wang, W.-J. An, B. Ramalingam, S. Mukherjee, D. M. Niedzwiedzki, S. Gangopadhyay and P. Biswas, *J. Am. Chem. Soc.*, 2012, **134**, 11276.
398 H. Xu, S. Ouyang, L. Liu, D. Wang, T. Kako and J. Ye, *Nanotechnology*, 2014, **25**, 165402.
399 X. An, K. Li and J. Tang, *ChemSusChem*, 2014, **7**, 1086.
400 H.-C. Hsu, I. Shown, H.-Y. Wei, Y.-C. Chang, H.-Y. Du, Y.-G. Lin, C.-A. Tseng, C.-H. Wang, L.-C. Chen, Y.-C. Lin and K.-H. Chen, *Nanoscale*, 2013, **5**, 262.
401 J. Yu, J. Jin, B. Cheng and M. Jaroniec, *J. Mater. Chem. A*, 2014, **2**, 3407.
402 S.-I. In, D. D. Vaughn II and R. E. Schaak, *Angew. Chem., Int. Ed.*, 2012, **51**, 3915.
403 L. Liu, W. Fan, X. Zhao, H. Sun, P. Li and L. Sun, *Langmuir*, 2012, **28**, 10415.
404 S. N. Habisreutinger, L. Schmidt-Mende and J. K. Stolarczyk, *Angew. Chem., Int. Ed.*, 2013, **52**, 7372.
405 N. Sasirekha, S. J. S. Basha and K. Shanthi, *Appl. Catal., B*, 2006, **62**, 169.
406 K. Kočí, L. Obalová and O. Šolcová, *Chem. Process. Eng.*, 2010, **31**, 395.
407 S. Neatu, J. A. Maciá-Agulló, P. Concepción and H. Garcia, *J. Am. Chem. Soc.*, 2014, **136**, 15969.
408 A. Dhakshinamoorthy, S. Navalon, A. Corma and H. Garcia, *Energy Environ. Sci.*, 2012, **5**, 9217.
409 S. S. Tan, L. Zou and E. Hu, *Sci. Technol. Adv. Mater.*, 2007, **8**, 89.
410 T. Mizuno, K. Adachi, K. Ohta and A. Saji, *J. Photochem. Photobiol., A*, 1996, **98**, 87.
411 S. Kaneco, Y. Shimizu, K. Ohta and T. Mizuno, *J. Photochem. Photobiol., A*, 1998, **115**, 223.
412 M. Anpo, H. Yamashita, Y. Ichihashi and S. Ehara, *J. Electroanal. Chem.*, 1995, **396**, 21.
413 L. Liu, H. Zhao, J. M. Andino and Y. Li, *ACS Catal.*, 2012, **2**, 1817.
414 W. Wang, W. Huang, Y. Ni, C. Lu and Z. Xu, *ACS Appl. Mater. Interfaces*, 2014, **6**, 340.
415 H. He, P. Zapol and L. A. Curtiss, *Energy Environ. Sci.*, 2012, **5**, 6196.
416 V. P. Indrakanti, J. D. Kubicki and H. H. Schobert, *Energy Environ. Sci.*, 2009, **2**, 745.
417 F. Saladin, L. Forss and I. Kamber, *J. Chem. Soc., Chem. Commun.*, 1995, 533.
418 K. Xie, N. Umezawa, N. Zhang, P. Reunchan, Y. Zhang and J. Ye, *Energy Environ. Sci.*, 2011, **4**, 4211.
419 J. Lee, D. C. Sorescu and X. Deng, *J. Am. Chem. Soc.*, 2011, **133**, 10066.
420 R. Asahi, T. Morikawa, T. Ohwaki, K. Aoki and Y. Taga, *Science*, 2001, **293**, 269.
421 J. H. Park, S. Kim and A. J. Bard, *Nano Lett.*, 2006, **6**, 24.
422 R. Boppella, S. Thomas Kochuveedu, H. Kim, M. J. Jeong, F. Marques Mota, J. H. Park and D. H. Kim, *ACS Appl. Mater. Interfaces*, 2017, **9**, 7075.
423 Z. Xu, M. Quintanilla, F. Vetrone, A. O. Govorov, M. Chaker and D. Ma, *Adv. Funct. Mater.*, 2015, **25**, 2950.
424 H. Kwon, F. Marques Mota, K. Chung, Y. J. Jang, J. K. Hyun, J. Lee and D. H. Kim, *ACS Sustainable Chem. Eng.*, 2018, **6**, 1310.
425 J. Li, M. Zhang, Z. Guan, Q. Li, C. He and J. Yang, *Appl. Catal., B*, 2017, **206**, 300.
426 F. Zuo, K. Bozhilov, R. J. Dillon, L. Wang, P. Smith, X. Zhao, C. Bardeen and P. Feng, *Angew. Chem.*, 2012, **124**, 6327.
427 R. Boppella, J.-E. Lee, F. Marques Mota, J. Y. Kim, Z. Feng and D. H. Kim, *J. Mater. Chem. A*, 2017, **5**, 7072.
428 G. R. Dey, A. D. Belapurkar and K. Kishore, *J. Photochem. Photobiol., A*, 2004, **163**, 503.
429 X. Meng, S. Ouyang, T. Kako, P. Li, Q. Yu, T. Wang and J. Ye, *Chem. Commun.*, 2014, **50**, 11517.
430 Q. Xiang, J. Yu and M. Jaroniec, *Nanoscale*, 2011, **3**, 3670.
431 W. J. Lee, J. M. Lee, S. T. Kochuveedu, T. H. Han, H. Y. Jeong, M. Park, J. M. Yun, J. Kwon, K. No, D. H. Kim and S. O. Kim, *ACS Nano*, 2012, **6**, 935.
432 L. N. Quan, Y. H. Jang, K. A. Stoerzinger, K. J. May, Y. J. Jang, S. T. Kochuveedu, Y. Shao-Horn and D. H. Kim, *Phys. Chem. Chem. Phys.*, 2014, **16**, 9023.
433 G. Yin, Q. Bi, W. Zhao, J. Xu, T. Lin and F. Huang, *ChemCatChem*, 2017, **9**, 4389.
434 M. Manzanares, C. Fàbrega, J. O. Ossó, L. F. Vega, T. Andreu and J. R. Morante, *Appl. Catal., B*, 2014, **150–151**, 57.
435 S. Xie, Y. Wang, Q. Zhang, W. Fan, W. Deng and Y. Wang, *Chem. Commun.*, 2013, **49**, 2451.
436 K. Kočí, L. Obalová, L. Matějová, D. Plachá, Z. Lacný, J. Jirkovský and O. Šolcová, *Appl. Catal., B*, 2009, **89**, 494.
437 H. Xu, S. Ouyang, P. Li, T. Kako and J. Ye, *ACS Appl. Mater. Interfaces*, 2013, **5**, 1348.
438 K. L. Schulte, P. A. DeSario and K. A. Gray, *Appl. Catal., B*, 2010, **97**, 354.

439 K. Li, T. Peng, Z. Ying, S. Song and J. Zhang, *Appl. Catal., B*, 2016, **180**, 130.
440 W. Jiao, L. Wang, G. Liu, G. Q. (Max) Lu and H.-M. Cheng, *ACS Catal.*, 2012, **2**, 1854.
441 L. Ye, J. Mao, T. Peng, L. Zan and Y. Zhang, *Phys. Chem. Chem. Phys.*, 2014, **16**, 15675.
442 J. Pan, X. Wu, L. Wang, G. Liu, G. Q. (Max) Lu and H.-M. Cheng, *Chem. Commun.*, 2011, **47**, 8361.
443 Z. He, L. Wen, D. Wang, Y. Xue, Q. Lu, C. Wu, J. Chen and S. Song, *Energy Fuels*, 2014, **28**, 3982.
444 J. Yu, J. Low, W. Xiao, P. Zhou and M. Jaroniec, *J. Am. Chem. Soc.*, 2014, **136**, 8839.
445 Q. Xu, J. Yu, J. Zhang, J. Zhang and G. Liu, *Chem. Commun.*, 2015, **51**, 7950.
446 M. Anpo, H. Yamashita, K. Ikeue, Y. Fujii, Y. Ichihashi, S. G. Zhang, D. R. Park, S. Ehara, S.-E. Park, J.-S. Chang and J. W. Yoo, *Stud. Surf. Sci. Catal.*, 1998, **114**, 177.
447 K. Ikeue, H. Yamashita and M. Anpo, *J. Phys. Chem. B*, 2001, **105**, 8350.
448 S. G. Zhang, Y. Fujii, H. Yamashita, K. Koyano, T. Tatsumi and M. Anpo, *Chem. Lett.*, 1997, 659.
449 M. Anpo, H. Yamashita, K. Ikeue, Y. Fujii, S. G. Zhang, Y. Ichihashi, D. R. Park, Y. Suzuki, K. Koyano and T. Tatsumi, *Catal. Today*, 1998, **44**, 327.
450 J.-S. Hwang, J.-S. Chang, S.-E. Park, K. Ikeue and M. Anpo, *Top. Catal.*, 2005, **35**, 311.
451 M. Hussain, P. Akhter, G. Saracco and N. Russo, *Appl. Catal., B*, 2015, **170–171**, 53.
452 M. S. Khan, M. N. Ashiq, M. F. Ehsan, T. He and S. Ijaz, *Appl. Catal., A*, 2014, **487**, 202.
453 A. Paracchino, V. Laporte, K. Sivula, M. Grätzel and E. Thimsen, *Nat. Mater.*, 2011, **10**, 456.
454 P. Dias, M. Schreier, S. D. Tilley, J. Luo, J. Azevedo, L. Andrade, D. Bi, A. Hagfeldt, A. Mendes, M. Grätzel and M. T. Mayer, *Adv. Energy Mater.*, 2015, **5**, 1501537.
455 Z. Xiong, Z. Lei, C.-C. Kuang, X. Chen, B. Gong, Y. Zhao, J. Zhang, C. Zheng and J. C. S. Wu, *Appl. Catal., B*, 2017, **202**, 695.
456 S. Zhu, S. Liang, Y. Wang, X. Zhang, F. Li, H. Lin, Z. Zhang and X. Wang, *Appl. Catal., B*, 2016, **187**, 11.
457 K. Teramura, S. Iguchi, Y. Mizuno, T. Shishido and T. Tanaka, *Angew. Chem., Int. Ed.*, 2012, **51**, 8008.
458 K. Katsumata, K. Sakai, K. Ikeda, G. Carja, N. Matsushita and K. Okada, *Mater. Lett.*, 2013, **107**, 138.
459 Y. Zhao, G. Chen, T. Bian, C. Zhou, G. I. N. Waterhouse, L.-Z. Wu, C.-H. Tung, L. J. Smith, D. O'Hare and T. Zhang, *Adv. Mater.*, 2015, **27**, 7824.
460 S. K. Parayil, A. Razzaq, S.-M. Park, H. R. Kim, C. A. Grimes and S.-I. In, *Appl. Catal., A*, 2015, **498**, 205.
461 G. Xi, S. Ouyang, P. Li, J. Ye, Q. Ma, N. Su, H. Bai and C. Wang, *Angew. Chem.*, 2012, **124**, 2445.
462 Y. Y. Lee, H. S. Jung, J. M. Kim and Y. T. Kang, *Appl. Catal., B*, 2018, **224**, 594.
463 Y.-X. Pan, Y. You, S. Xin, Y. Li, G. Fu, Z. Cui, Y.-L. Men, F.-F. Cao, S.-H. Yu and J. B. Goodenough, *J. Am. Chem. Soc.*, 2017, **139**, 4123.
464 Y. Zhou, Z. Tian, Z. Zhao, Q. Liu, J. Kou, X. Chen, J. Gao, S. Yan and Z. Zou, *ACS Appl. Mater. Interfaces*, 2011, **3**, 3594.
465 H. Cheng, B. Huang, Y. Liu, Z. Wang, X. Qin, X. Zhanga and Y. Daib, *Chem. Commun.*, 2012, **48**, 9729.
466 Y. Y. Lee, H. S. Jung and Y. T. Kang, *J. CO2 Util.*, 2017, **20**, 163.
467 Y. P. Xie, G. Liu, L. Yin and H.-M. Cheng, *J. Mater. Chem.*, 2012, **22**, 6746.
468 S. C. Yan, S. X. Ouyang, J. Gao, M. Yang, J. Y. Feng, X. X. Fan, L. J. Wan, Z. S. Li, J. H. Ye, Y. Zhou and Z. G. Zou, *Angew. Chem., Int. Ed.*, 2010, **49**, 6400.
469 Q. Liu, Y. Zhou, W. Tu, S. Yan and Z. Zou, *Inorg. Chem.*, 2014, **53**, 359.
470 Q. Liu, Y. Zhou, J. Kou, X. Chen, Z. Tian, J. Gao, S. Yan and Z. Zou, *J. Am. Chem. Soc.*, 2010, **132**, 14385.
471 N. Zhang, S. Ouyang, P. Li, Y. Zhang, G. Xi, T. Kako and J. Ye, *Chem. Commun.*, 2011, **47**, 2041.
472 V. B. R. Boppana, N. D. Hould and R. F. Lobo, *J. Solid State Chem.*, 2011, **184**, 1054.
473 H. Park, J. H. Choi, K. M. Choi, D. K. Lee and J. K. Kang, *J. Mater. Chem.*, 2012, **22**, 5304.
474 Q. Liu, D. Wu, Y. Zhou, H. Su, R. Wang, C. Zhang, S. Yan, M. Xiao and Z. Zou, *ACS Appl. Mater. Interfaces*, 2014, **6**, 2356.
475 S. Yan, J. Wang, H. Gao, N. Wang, H. Yu, Z. Li, Y. Zhou and Z. Zou, *Adv. Funct. Mater.*, 2012, **23**, 758.
476 Q. Liu, Y. Zhou, Z. Tian, X. Chen, J. Gao and Z. Zou, *J. Mater. Chem.*, 2012, **22**, 2033.
477 S. Yan, H. Yu, N. Wang, Z. Liab and Z. Zou, *Chem. Commun.*, 2012, **48**, 1048.
478 N. Zhang, S. Ouyang, T. Kako and J. Ye, *Chem. Commun.*, 2012, **48**, 1269.
479 Q. Li, X. Li, S. Wageh, A. A. Al-Ghamdi and J. Yu, *Adv. Energy Mater.*, 2015, **5**, 1500010.
480 P. Praus, O. Kozák, K. Kočí, A. Panáček and R. Dvorský, *J. Colloid Interface Sci.*, 2011, **360**, 574.
481 H. Fujiwara, H. Hosokawa, K. Murakoshi, Y. Wada, S. Yanagida, T. Okada and H. Kobayashi, *J. Phys. Chem. B*, 1997, **101**, 8270.
482 P. Kar, S. Farsinezhad, X. Zhang and K. Shankar, *Nanoscale*, 2014, **6**, 14305.
483 H. Shi and Z. Zou, *J. Phys. Chem. Solids*, 2012, **73**, 788.
484 P. Li, S. Ouyang, G. Xi, T. Kako and J. Ye, *J. Phys. Chem. C*, 2012, **116**, 7621.
485 H. Shi, T. Wang, J. Chen, C. Zhu, J. Ye and Z. Zou, *Catal. Lett.*, 2011, **141**, 525.
486 X. Li, H. Pan, W. Li and Z. Zhuang, *Appl. Catal., A*, 2012, **413–414**, 103.
487 G. Li, S. Ciston, Z. V. Saponjic, L. Chen, N. M. Dimitrijevic, T. Rajh and K. A. Gray, *J. Catal.*, 2008, **253**, 105.
488 H. Zhao, L. Liu, J. M. Andino and Y. Li, *J. Mater. Chem. A*, 2013, **1**, 8209.
489 P.-Q. Wang, Y. Bai, J.-Y. Liu, Z. Fan and Y.-Q. Hu, *Catal. Commun.*, 2012, **29**, 185.
490 K. Wu and T. Lian, *Chem. Soc. Rev.*, 2016, **45**, 3781.

491 C. Wang, R. L. Thompson, J. Baltrus and C. Matranga, *J. Phys. Chem. Lett.*, 2010, **1**, 48.
492 C. Wang, R. L. Thompson, P. Ohodnicki, J. Baltrus and C. Matranga, *J. Mater. Chem.*, 2011, **21**, 13452.
493 S. Chan, M. Liu, K. Latham, M. Haruta, H. Kurata, T. Teranishi and Y. Tachibana, *J. Mater. Chem. C*, 2017, **5**, 2182.
494 Y.-F. Xu, M.-Z. Yang, B.-X. Chen, X.-D. Wang, H.-Y. Chen, D.-B. Kuang and C.-Y. Su, *J. Am. Chem. Soc.*, 2017, **139**, 5660.
495 G. Xi, S. Ouyang and J. Ye, *Chem. – Eur. J.*, 2011, **17**, 9057.
496 H. Shi, G. Chen, C. Zhang and Z. Zou, *ACS Catal.*, 2014, **4**, 3637.
497 J. Jin, J. Yu, D. Guo, C. Cui and W. Ho, *Small*, 2015, **11**, 5262.
498 J. Rascó, *Catal. Lett.*, 1998, **56**, 11.
499 K. Kočí, K. Matějů, L. Obalová, S. Krejčíková, Z. Lacný, D. Plachá, L. Čapek, A. Hospodková and O. Šolcová, *Appl. Catal., B*, 2010, **96**, 239.
500 O. Ishitani, C. Inoue, Y. Suzuki and T. Ibusuki, *J. Photochem. Photobiol., A*, 1993, **72**, 269.
501 W. Hou, W. H. Hung, P. Pavaskar, A. Goeppert, M. Aykol and S. B. Cronin, *ACS Catal.*, 2011, **1**, 929.
502 J. C. Hemminger, R. Carr and G. A. Somorjai, *Chem. Phys. Lett.*, 1978, **57**, 100.
503 G. Guan, T. Kida and A. Yoshida, *Appl. Catal., B*, 2003, **41**, 387.
504 K. Iizuka, T. Wato, Y. Miseki, K. Saito and A. Kudo, *J. Am. Chem. Soc.*, 2011, **133**, 20863.
505 T. Yui, A. Kan, C. Saitoh, K. Koike, T. Ibusuki and O. Ishitani, *ACS Appl. Mater. Interfaces*, 2011, **3**, 2594.
506 J. Yu, K. Wang, W. Xiao and B. Cheng, *Phys. Chem. Chem. Phys.*, 2014, **16**, 11492.
507 S. Xie, Y. Wang, Q. Zhang, W. Deng and Y. Wang, *ACS Catal.*, 2014, **4**, 3644.
508 N. Li, M. Liu, B. Yang, W. Shu, Q. Shen, M. Liu and J. Zhou, *J. Phys. Chem. C*, 2017, **121**, 2923.
509 Y. Li, W.-N. Wang, Z. Zhan, M.-H. Woo, C.-Y. Wu and P. Biswas, *Appl. Catal., B*, 2010, **100**, 386.
510 O. K. Varghese, M. Paulose, T. J. LaTempa and C. A. Grimes, *Nano Lett.*, 2009, **9**, 731.
511 T.-V. Nguyen and J. C. S. Wu, *Appl. Catal., A*, 2008, **335**, 112.
512 X. Zhang, F. Han, B. Shi, S. Farsinezhad, G. P. Dechaine and K. Shankar, *Angew. Chem., Int. Ed.*, 2012, **51**, 12732.
513 R. Long, Y. Li, Y. Liu, S. Chen, X. Zheng, C. Gao, C. He, N. Chen, Z. Qi, L. Song, J. Jiang, J. Zhu and Y. Xiong, *J. Am. Chem. Soc.*, 2017, **139**, 4486.
514 Q. Zhai, S. Xie, W. Fan, Q. Zhang, Y. Wang, W. Deng and Y. Wang, *Angew. Chem., Int. Ed.*, 2013, **52**, 5776.
515 S. Zeng, D. Baillargeat, H.-P. Ho and K.-T. Yong, *Chem. Soc. Rev.*, 2014, **43**, 3426.
516 M. W. Knight, H. Sobhani, P. Nordlander and N. J. Halas, *Science*, 2011, **332**, 702.
517 S. C. Warren and E. Thimsen, *Energy Environ. Sci.*, 2012, **5**, 5133.
518 Y. H. Jang, Y. J. Jang, S. Kim, L. N. Quan, K. Chung and D. H. Kim, *Chem. Rev.*, 2016, **116**, 14982.
519 C. H. Choi, K. Chung, T. T. H. Nguyen and D. H. Kim, *ACS Energy Lett.*, 2018, **3**, 1415.
520 Y. Zhang, S. He, W. Guo, Y. Hu, J. Huang, J. R. Mulcahy and W. D. Wei, *Chem. Rev.*, 2018, **118**, 2927.
521 P. Christopher, H. Xin, A. Marimuthu and S. Linic, *Nat. Mater.*, 2012, **11**, 1044.
522 S. Mubeen, J. Lee, N. Singh, S. Krämer, G. D. Stucky and M. Moskovits, *Nat. Nanotechnol.*, 2013, **8**, 247.
523 S. Linic, P. Christopher, H. Xin and A. Marimuthu, *Acc. Chem. Res.*, 2013, **46**, 1890.
524 M. J. Kale, T. Avanesian and P. Christopher, *ACS Catal.*, 2014, **4**, 116.
525 U. Aslam, V. G. Rao, S. Chavez and S. Linic, *Nat. Catal.*, 2018, **1**, 656.
526 J. Low, S. Qiu, D. Xu, C. Jiang and B. Cheng, *Appl. Surf. Sci.*, 2018, **434**, 423.
527 Z. Zhang, Z. Wang, S.-W. Cao and C. Xue, *J. Phys. Chem. C*, 2013, **117**, 25939.
528 W. Tu, Y. Zhou, H. Li, P. Li and Z. Zou, *Nanoscale*, 2015, **7**, 14232.
529 Y. Zheng, J. Liu, J. Liang, M. Jaroniec and S. Z. Qiao, *Energy Environ. Sci.*, 2012, **5**, 6717.
530 J. Lin, Z. Pan and X. Wang, *ACS Sustainable Chem. Eng.*, 2014, **2**, 353.
531 X. An and J. C. Yu, *RSC Adv.*, 2011, **1**, 1426.
532 Y. T. Liang, B. K. Vijayan, K. A. Gray and M. C. Hersam, *Nano Lett.*, 2011, **11**, 2865.
533 Y. T. Liang, B. K. Vijayan, O. Lyandres, K. A. Gray and M. C. Hersam, *J. Phys. Chem. Lett.*, 2012, **3**, 1760.
534 W. Tu, Y. Zhou, Q. Liu, Z. Tian, J. Gao, X. Chen, H. Zhang, J. Liu and Z. Zou, *Adv. Funct. Mater.*, 2012, **22**, 1215.
535 X.-H. Xia, Z.-J. Jia, Y. Yu, Y. Liang, Z. Wang and L.-L. Ma, *Carbon*, 2007, **45**, 717.
536 W. Wang, D. Xu, B. Cheng, J. Yu and C. Jiang, *J. Mater. Chem. A*, 2017, **5**, 5020.
537 W. Tu, Y. Zhou, Q. Liu, S. Yan, S. Bao, X. Wang, M. Xiao and Z. Zou, *Adv. Funct. Mater.*, 2013, **23**, 1743.
538 Q. Kang, T. Wang, P. Li, L. Liu, K. Chang, M. Li and J. Ye, *Angew. Chem., Int. Ed.*, 2015, **54**, 841.
539 S. Xie, Q. Zhang, G. Liu and Y. Wang, *Chem. Commun.*, 2016, **52**, 35.
540 N. C. D. Nath, S. Y. Choi, H. W. Jeong, J.-J. Lee and H. Park, *Nano Energy*, 2016, **25**, 51.
541 S. Ichikawa and R. Doi, *Catal. Today*, 1996, **27**, 271.
542 X. Chang, T. Wang, P. Zhang, Y. Wei, J. Zhao and J. Gong, *Angew. Chem., Int. Ed.*, 2016, **128**, 8986.
543 T. J. LaTempa, S. Rani, N. Bao and C. A. Grimes, *Nanoscale*, 2012, **4**, 2245.
544 G. Magesh, E. S. Kim, H. J. Kang, M. Banu, J. Y. Kim, J. H. Kim and J. S. Lee, *J. Mater. Chem. A*, 2014, **2**, 2044.
545 J. H. Kim, G. Magesh, H. J. Kang, M. Banu, J. H. Kim, J. Lee and J. S. Lee, *Nano Energy*, 2015, **15**, 153.
546 M. I. Litter and J. A. Navío, *J. Photochem. Photobiol., A*, 1996, **98**, 171.
547 C. Burda, Y. Lou, X. Chen, A. C. S. Samia, J. Stout and J. L. Gole, *Nano Lett.*, 2003, **3**, 1049.
548 W.-H. Lee, C.-H. Liao, M.-F. Tsai, C.-W. Huang and J. C. S. Wu, *Appl. Catal., B*, 2013, **132–133**, 445.

549 F. Galli, M. Compagnoni, D. Vitali, C. Pirola, C. L. Bianchi, A. Villa, L. Prati and I. Rossetti, *Appl. Catal., B*, 2017, **200**, 386.
550 M. Salaices, B. Serrano and H. I. de Lasa, *Chem. Eng. J.*, 2002, **90**, 219.
551 J. Luo, J.-H. Im, M. T. Mayer, M. Schreier, M. K. Nazeeruddin, N.-G. Park, S. D. Tilley, H. J. Fan and M. Grätzel, *Science*, 2014, **345**, 1593.
552 L. Gao, Y. Cui, R. H. J. Vervuurt, D. van Dam, R. P. J. van Veldhoven, J. P. Hofmann, A. A. Bol, J. E. M. Haverkort, P. H. L. Notten, E. P. A. M. Bakkers and E. J. M. Hensen, *Adv. Funct. Mater.*, 2016, **26**, 679.
553 J. L. Young, M. A. Steiner, H. Döscher, R. M. France, J. A. Turner and T. G. Deutsch, *Nat. Energy*, 2017, **2**, 17028.
554 A. Van Miltenburg, W. Zhu, F. Kapteijn and J. A. Moulijn, *Chem. Eng. Res. Des.*, 2006, **84**, 350.